Model Predictive Control of Grid-Connected Voltage Source Converters

A thesis submitted in fulfilment of the requirements for the degree of Doctor of Philosophy

by

Dae Keun Yoo

Supervisor: Prof. Liuping Wang

School of Electrical and Computer Engineering
RMIT University
September 2013

Declaration

I declare that this thesis is my own work and has not been submitted in any form for another degree or diploma at any university or other institute of tertiary education. Information derived from the published and unpublished work of others has been acknowledged in the text and a list of references is given.

Dae Keun Yoo

September/2013

Abstract

Recently, a growth in the renewable energy market, especially in the field of solar and wind energy sector have increased considerably due to uncertain and unstable future supply of crude oil and problems caused by pollution. This continuous growth of renewable energy market will demand new technologies in the area of power electronics, especially in grid connected systems. Furthermore as the regulations and standards put a stringent limitation on individual and total harmonic distortion level allowed to be injected into the grid, the control requirements for grid connected systems consequently become even more complex and challenging. In order to meet these demands, a continuous progress in the field of converters topologies and control techniques is necessary.

In this thesis, the main focus is on the design and implementation of an advanced control scheme, namely model predictive control (MPC) to the grid-connected voltage source converter (VSC) for a three phase system. MPC is a control paradigm that solves a mathematical optimization problem based on a dynamic model of the system. Due to the computationally demanding nature of MPC, the areas of applications have long been restricted to slow dynamical systems. However, with the recent advancement of microprocessor and simulation technologies, application of MPC is now even possible for the control of power electronics. With a very powerful concept such as on-line cost optimisation, input/output constraint handling and model-based design, MPC is able to offer the optimal actuation that allows one to achieve very fast dynamics, while also considering uncertainties such as system parameter variations and unknown disturbances. Furthermore, it is also possible to take advantage of the discrete nature of the power converters and choose from the possible switching states the optimal solution according to the minimization of a predefined cost.

Exploring these advantages of MPC and making them suitable for the control of power converters are the key focus of the thesis.

The first part of the thesis investigates a multi-variable control scheme, namely a predictive voltage controller that controls both DC bus voltage and reactive current (i.e. q-axis current) in the synchronous reference frame. Explicit tuning methods of MPC are introduced to improve the closed-loop transient response as well as improving the robustness against the parameter variations such as the grid inductance.

The second part of the thesis focuses on the predictive current control design. A predictive current controller for VSC with LCL (inductor-capacitor-inductor) input filter is first proposed with a robust control scheme that employs nominal and disturbance rejection control parts. The nominal control part is designed using the reduced-order model (i.e. L filter model) to control dominant dynamics of the LCL filter where as the disturbance rejection control part actively suppresses the disturbance due to unmodeled dynamics of LCL filter (i.e. resonance of the LCL filter). Following from this, a predictive resonant controller is presented to control the converter in the stationary frame axis. A resonant module with a grid frequency is embedded in the model to handle the periodicity in the measured states and the reference inputs. The proposed design considers the periodic input constraints in the stationary frame as well as disturbances due to grid voltage distortion. The last part of the thesis investigates the stability aspect of a finite control set predictive control (FCS-MPC) method and presents a design framework to handle the imposed the output current constraints in the cost function.

All of the presented control methods in this thesis are experimentally validated on a 1kW prototype converter that has been built by the author.

Acknowledgments

Foremost, I would like to express my sincere gratitude to my advisor Prof. Liuping Wang for providing excellent guidance and assistance during my Ph.D study and research. I also would like to acknowledge and thank the industry partners, ANCA Motion Pty Ltd and AMCRC for providing the financial assistance and equipment for this research to be carried out.

My sincere thanks also goes to my colleagues Ki Ng, Dr. Nguyen-Vu Truong, Dr. Shan Chai, Lu Gan and Dr. Sven Dominica who have helped me in many ways during my candidature.

On a personal note, I would like to thank my family, Sujin, Nathan and Olivia for their love, kindness and support they have shown during the past four years it has taken me to finalize this thesis.

Contents

List of Figures

List of Tables

List of Symbols

LMI	Linear Matrix Inequalities
AC	Alternating Current
ARE	Algebraic Riccati Equation
DC	Direct Current
IGBT	Insulated Gate Bipolar Transistor
LMI	Linear Matrix Inequalities
LTI	Linear Time Invariant
MPC	Model Predictive Control
PLL	Phase Locked Loop
PV	Photovoltaic
PWM	Pulse Width Modulation
VSC	Voltage Source Converter
WT	Wind Turbine

CHAPTER 1

Introduction

1.1 Background

Recently, a growth in the renewable energy market, especially in the field of solar and wind energy sector have increased considerably due to uncertain and unstable future supply of crude oil and problems caused by pollution. This continuous growth of renewable energy market will demand new technologies in the area of power electronics, especially in grid connected systems.

The most conventional configuration of a grid connected renewable energy system is shown in Figure 1.1, where a renewable energy source can either be supplied by a photovoltaic array or a wind turbine. As also indicated in the figure, the output stage, which is connected to the main grid, essentially remains the same regardless of the type of renewable energy source. For this output stage, a PWM controlled converter is typically used to convert and adapt the energy accumulated in an intermediate storage element (dc-link capacitor). The converter must be controlled to ensure that the correct flow of energy from the generator to the grid or vice-versa is guaranteed. Furthermore as the regulations and standards such as IEC 1000-3-2, IEC 1000-3-4 and IEEE Standard 519 [1],[2],[3] put a stringent limitation on individual and total harmonic distortion level allowed to be injected into the grid, the control requirements for grid connected systems consequently becomes even more complex and challenging. In order to meet these demands, a continuous progress in the field of converters topologies, semiconductor devices and control techniques is neces-

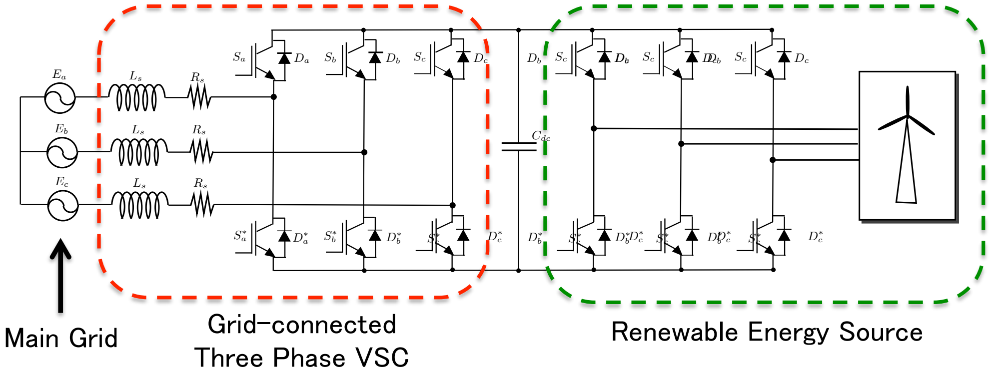

Figure 1.1: A renewable energy source with a grid-connected three phase voltage source converter

sary.

In this thesis, the main focus is on the design and implementation of an advanced control scheme, namely model predictive control (MPC) to the grid-connected voltage source converter (VSC) for a three phase system. MPC is a control paradigm that solves a mathematical optimization problem based on a dynamic model of the system. Due to the computationally demanding nature of MPC, the areas of applications have long been restricted to slow dynamical systems. However, with the recent advancement of microprocessor and simulation technologies, application of MPC is now even possible for the control of power electronics. With a very powerful concept such as on-line cost optimisation, input/output constraint handling and model-based design, MPC is able to offer the optimal actuation that allows one to achieve very fast dynamics, while also considering uncertainties such as system parameter variations and unknown disturbances. Furthermore, it is also possible to take advantage of the discrete nature of the power converters and choose from the possible switching states the optimal solution according to the minimization of a predefined cost. Exploring these advantages of MPC and making them suitable for the control of power converters are the key focus of the thesis.

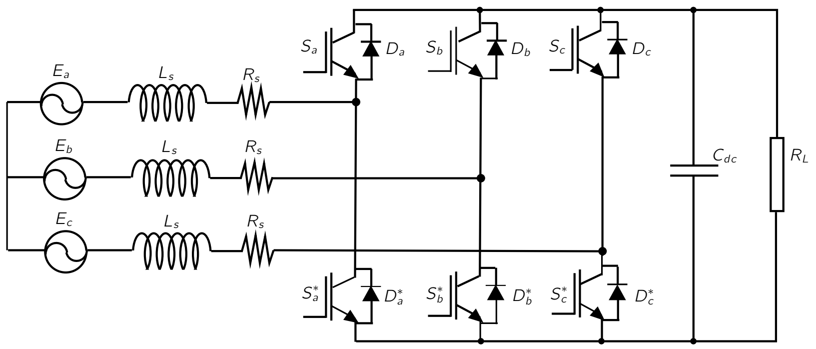

Figure 1.2: A typical three phase voltage source converter with bi-directional power transfer capability.

1.2 Literature Review

This section presents a literature review on the major topics relating to grid-connected voltage source converters (VSC) and model predictive control (MPC).

The first two sections (section 1.2.1 and 1.2.2) focus on the area of grid-connected VSC, where we review some of the major converter topologies and closed-loop control techniques which have been used to achieve bi-directional power transfer in grid-connected systems. In the last part of the section (section 1.2.3), a literature review of MPC is presented, where the main focus of the review is to give an overview of the wide and constantly expanding field of MPC, and to discuss the topics relating to the stability and robust stability problems of MPC.

1.2.1 Voltage Source Converter Topologies

Two-level converter

The most commonly used topology of a three phase voltage source with bidirectional energy flow capability and high quality input current waveforms is shown

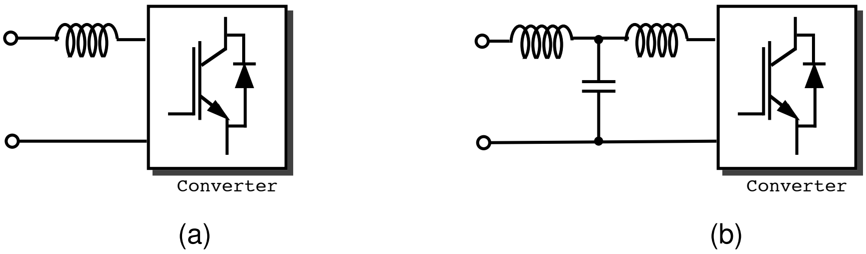

Figure 1.3: Input filter topologies: (a) L-filter (b) LCL filter

in Figure 1.2. In this topology, there are six semi-conductor switches which are coupled with free-wheeling diodes. The switches are typically controlled through PWM signals to allow the current to conduct in bi-directional way (from AC grid to DC load and vice versa). When the switches are controlled through PWM it is generally referred to as a 'hard-switching' scheme which generates a sequence of short pulse current during the switching cycle. These short bursts of current is rich in harmonics which can induce excessive harmonics on the main grid. To reduce the switching harmonics in the current, a line inductor must be placed between the grid and the converter, so the current generated from the converter is filtered to produce a near sinusoidal current. The line inductors also play a role in boosting DC-bus voltage level, where the boosted inductor current is transferred to DC link capacitor of the VSC which acts as an energy storage and filter for the DC link voltage.

Based on this configuration of topology, a size of passive component such as line inductors (and ESR) and DC-link capacitor, as well as the voltage/current rating of IGBT switches must be carefully selected to achieve the desired power ratings. In particular, for high power applications such as modern wind-turbines ranging from kW-MW, the switching frequency of the converter is generally chosen to be low in order to minimise the switching losses in the converter. A L-filter topology, shown in Figure 1.3 (a), is essentially the first order filter with attenuation of 20 dB/dec for the ranges of PWM harmonic frequency, which means that a relatively large inductance is required for a low PWM switching frequency. Generally, a large inductance in the input filter also means a slow current dynamics which in turn affect the dynamics of the whole converter system. As such, the trade-off between the size, cost and filtering capacity of L-filter becomes a serious limitation in high power applications. For this reason, the LCL circuit shown in Figure 1.3 (b), is often preferred as an input filter in high power applications which has a better filtering characteristics than the L-filter with comparatively smaller size of passive components [77].

There is one major disadvantage in LCL filter which is the inherent resonance present in the LCL filter. The resonance in LCL filter can cause static and transient distortion of the grid currents. The common countermeasures in the literature is to connect resistors to the filter in order to damp the resonance, known as passive damping. However a main disadvantage of such technique is that the damping resistance value required to provide satisfactory performance generally results in very high power losses. Alternatively the active damping method which emulates the damping resistor within the controller algorithm is also often used to avoid any extra losses.

In overall, the choice of the input filter must be chosen carefully considering various factors such as level of harmonics allowed to inject into the grid, power rating of VSC and cost of hardware etc. A comprehensive guidelines of choosing LCL filter component is illustrated in [64].

Multi-level converter

For low power systems, the two-level inverter is typically employed as the interface between dc-link and grid. However, as the power rating of the converter increases to around hundreds of kilowatts up to a few megawatts, the two-level converter with hard-switching scheme is no longer a viable option due

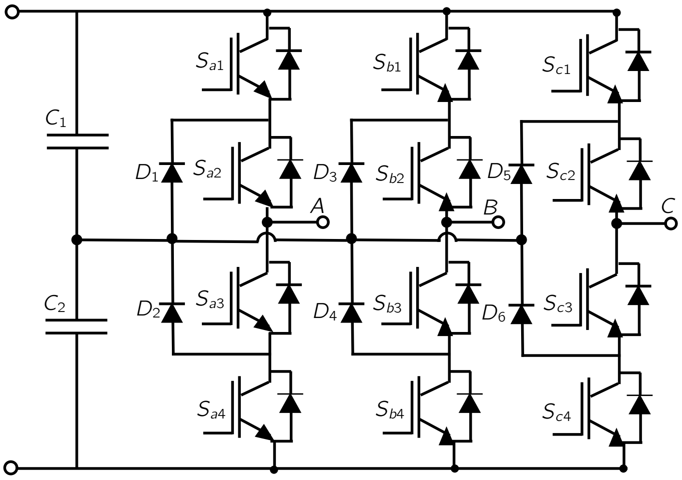

Figure 1.4: Topology of three-level Neutral-Point Clamped (NPC) converter

to a large voltage stress (dv/dt) that exceeds the power semi-conductor device rating. For these reasons, several alternative structure of the converter have been suggested in the literature. One alternative which is emerging as the standard solution for high power medium voltage applications, is the Multilevel Converter [54] [87],[52], where Figure 1.4 shows a topology of three-level Neutral-Point Clamped (NPC) converter. Compared to the two-level converter in the previous section, output waveform from the multi-level converter consists of several levels of voltages which improves the harmonic quality. As the number of levels increases, the synthesized output waveform approaches the sinusoidal wave with minimum harmonic distortion [52]. Furthermore, it permits the use of power devices with lower voltage rates due to a smaller voltage stress (dv/dt). Moreover, multilevel converters produce smaller common-mode (CM) voltage which reduces the stress in the bearings of a motor connected to a multilevel motor drive. Recently, with the development in modulation techniques and control techniques for multilevel converters, the area of multilevel converter application has expanded to include industrial medium-voltage motor drives [113] and utility interface for renewable energy systems [48],[99]

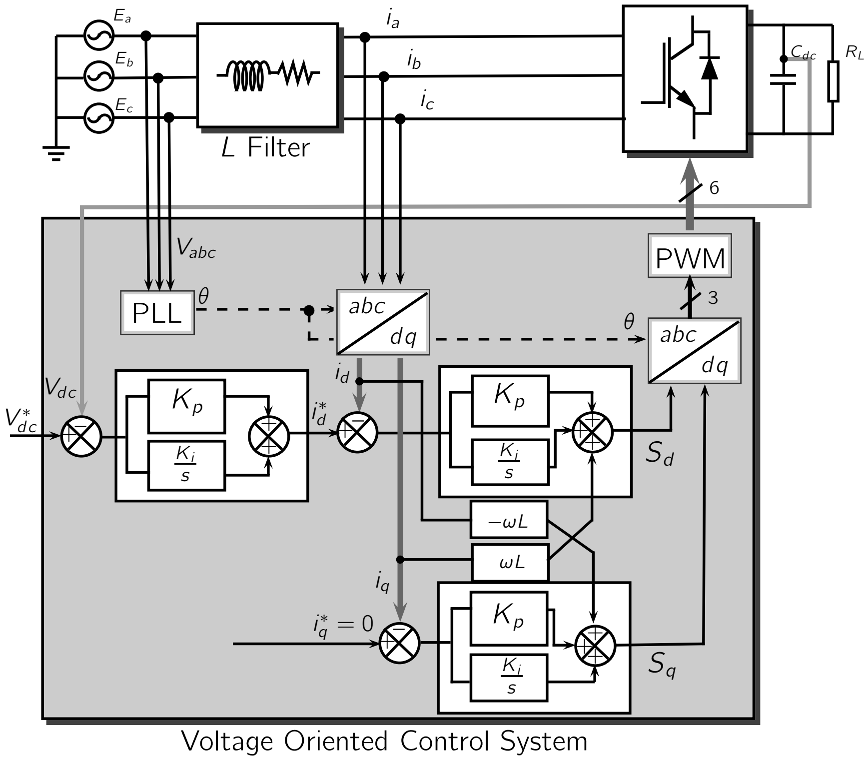

Figure 1.5: Voltage-oriented control system for grid-connected VSC: The outer control loop controls the DC-bus voltage and generates the reference input current i_d^*. The reference input of i_q^* is generally set to zero for unity power factor operation. Two inner control loop consist of PI control with feed-forward term.

Unfortunately, one of the main disadvantages of multilevel converters is the greater number of power semiconductor switches needed as shown in Figure 1.4. Although lower voltage rated switches can be utilized in a multilevel converter, each switch requires a related gate drive circuit, thus it causes the overall system to be more expensive and complex.

1.2.2 Voltage Source Converter Control

Voltage oriented control

The most widely used control method for grid-connected VSC is the voltage-oriented control (VOC) method [69],[34], which regulates the active and reactive power indirectly by their respective currents in the synchronous reference frame axis. In general, the VOC employs a cascaded control structure consists of outer voltage control loop and inner current loop as shown in Figure 1.5. The voltage control loop regulates a DC-bus voltage to a desired value by manipulating the d-axis reference current i_d^*, while the q-axis current i_q^* is controlled to zero to obtain a unity power factor. Since the dynamics of the inner current is faster than the DC-bus voltage dynamics, the inner loop are tuned to achieve a fast setting time, where as the outer voltage loop is designed to achieve an optimum regulation and stability. Symmetrical and modulus optimum tuning method is generally used to tune the voltage and current control loops respectively [61],[75]. Apart from the cascaded control loops, a grid-synchronisation module (shown as PLL in Figure 1.5) and synchronous-reference transformation are required as a part of the overall control system. The grid-synchronisation module mainly consists of a Phase-Locked-Loop (PLL) which tracks the phase angle of the grid voltage [102],[28]. The phase angle output from PLL is then used to generate the synchronous-reference transformed grid voltages and current.

Proportional Resonant Control

For the inner current loop control, a Proportional-Resonant control technique in a stationary frame is also often considered to overcome the computational burden while achieving virtually similar frequency response characteristics as a synchronous frame PI controller [56],[88],[115]. As evidently shown in Figure

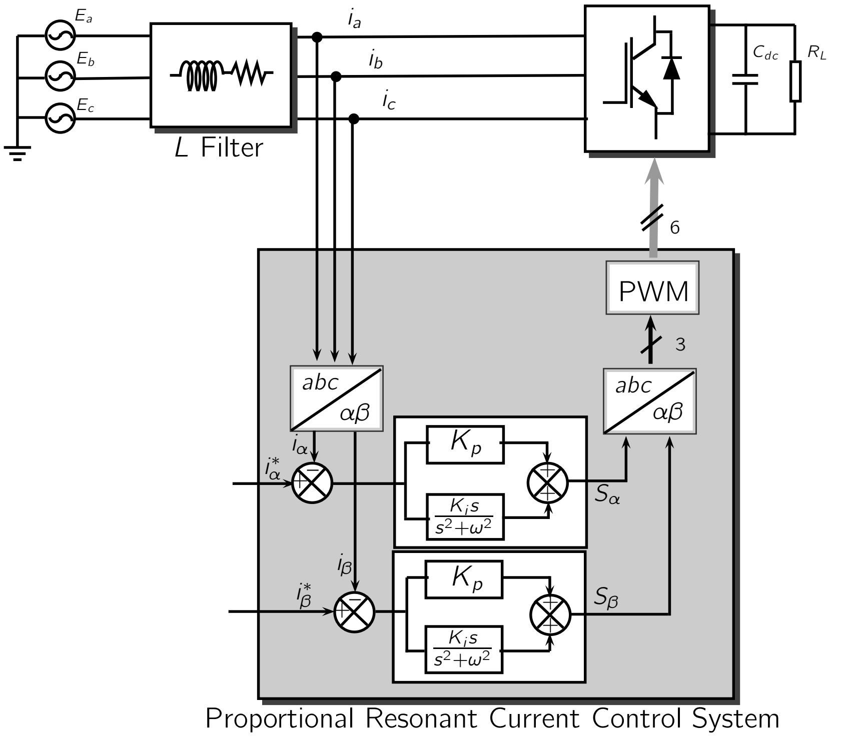

Figure 1.6: Proportional resonant current control system for grid-connected VSC: reference input currents for i^*_α and i^*_β are typically generated based on instantaneous power requirement. Two current control loop consists of a proportional term (K_p) and a generalised integrator ($\frac{K_i s}{s^2+\omega^2}$). Typically ω is set to the grid frequency.

1.6, a PLL is not required and the transformation is much simpler in the PR control implementation. In essence, the main idea of the PR controller is to introduce an infinite gain at a selected resonant frequency for eliminating steady-state error at that frequency, which is conceptually similar to a PI control whose infinite DC gain forces the DC steady-state error to zero. The resonant portion of the PR controller can therefore be viewed as a generalised AC integrator (GI), as proven in [88],[33]. The PR control system in Figure 1.6 assumes non-distorted grid voltage conditions, however, since the grid frequency often varies, the resonant module of the following is often employed.

$$G(s) = K_p + K_r \frac{\omega_c s}{s^2 + 2\omega_c s + \omega^2} \tag{1.1}$$

which has a damping term (ω_c) that can be tuned to give a robust performance subject to frequency variation.

Direct Power Control

Another control strategy, called direct power control (DPC), is based on the instantaneous active and reactive power control loops. In DPC, there are no internal current control loops and no PWM modulator block, and the converter switching states are appropriately selected by a switching table based on the instantaneous errors between the commanded and estimated values of active and reactive power. Figure 1.7 shows the block diagram of a typical DPC system. The instantaneous active and reactive power can be obtained from the estimated virtual flux or measured currents. The outputs of the power controller go through a switching table to decide the converter switching states appropriately.

As shown in Figure 1.7, the main part of DPC system is the estimation of the active and reactive line power which must be fast and accurate to guarantee the satisfactory control performance.

Many authors proposed an estimation algorithm which can largely be divided into voltage-based and virtual flux based estimation. For the voltage based estimation [104], the instantaneous active (P) and reactive power (Q)

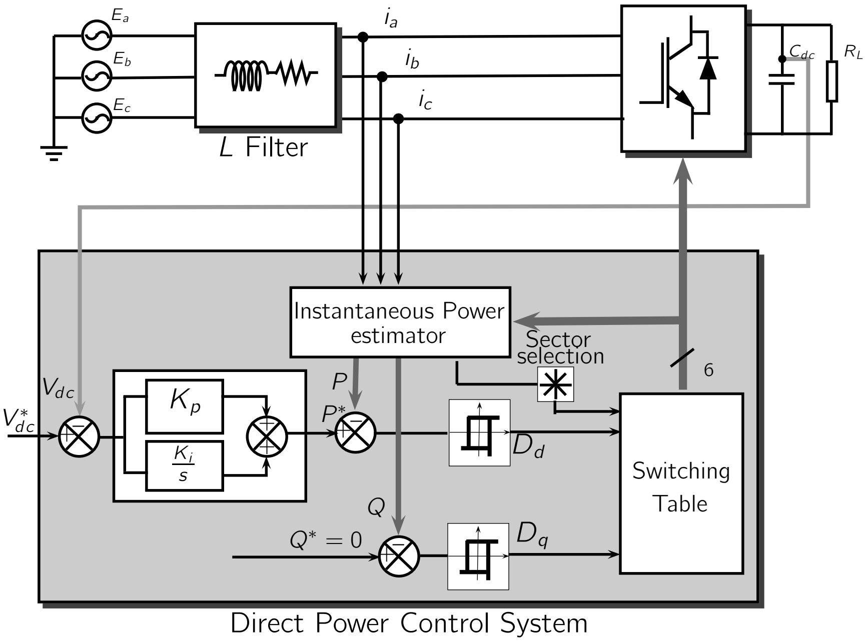

Figure 1.7: Direct Power control system for grid-connected VSC: P^* and Q^* are the reference active and reactive instantaneous power. D_d and D_q are the hysteresis control output which are used in the pre-defined switching table to generate switching output.

in ac voltage sensorless system are estimated using (1.2) and (1.3).

$$P = L\left(\frac{di_a}{dt}i_a + \frac{di_b}{dt}i_b + \frac{di_c}{dt}i_c\right) + V_{dc}(S_a i_a + S_b i_b + S_c i_c) \tag{1.2}$$

$$Q = \frac{1}{\sqrt{3}}\left\{3L\left(\frac{di_a}{dt}i_c + \frac{di_c}{dt}i_a\right) + V_{dc}(S_a(i_b - i_c) + S_b(i_c - i_a) + S_c(i_a - i_b))\right\} \tag{1.3}$$

Unfortunately, the above algorithm involves the computation of the derivative of the measured currents, so the computation may become noisy, especially at low currents.

To improve the voltage-based estimation, another method based on the virtual flux concept has been proposed by Malinowski et al. [75]. The concept of virtual flux is to relate the main grid to a virtual AC motor by making an analogy of grid inductance L and ESR R to the stator resistance and stator leakage inductance of the virtual motor. Based on the flux equation and the voltage loop equations in (1.4) and (1.5) respectively,

$$\Psi_g = \int u_g dt \tag{1.4}$$

$$u_g = u_s - Ri_g - L_g \frac{di_g}{dt} \tag{1.5}$$

Neglecting the ESR, the line virtual flux is calculated based on the measured line current and the inverter voltage

$$\Psi_g = \int u_s dt - L_g \cdot i_g \tag{1.6}$$

Using the virtual flux estimation in (1.6), the active and reactive power can be estimated as

$$P = \frac{3}{2}\omega(\Psi_\alpha i_\beta - \Psi_\beta i_\alpha) \tag{1.7}$$

$$Q = \frac{3}{2}\omega(\Psi_\alpha i_\alpha - \Psi_\beta i_\beta) \tag{1.8}$$

The DPC offers an interesting alternative to the VOC where there is no need for a complex transformation and the estimations can easily be implemented. The work by Noguchi et al. [104] showed that DPC can improve the total power factor and efficiency over VOC. One of the main drawback of DPC is the high sampling frequency required in response to obtain the estimated instantaneous active and reactive power accurately. Hence it is only feasible for a system with the fast microprocessor and A/D converters.

Deadbeat Control

With the development of digital control technology, especially with high-speed microprocessors, a control technique known as a deadbeat control has been well adopted in the control of power converters [56],[55],[103]. An application of deadbeat control in VSC requires a sampling of input current of the converter at each sampling instant, then prediction of input current given value is made based on the discrete model of the converter for the next sampling period. In order to make the phase current reach its reference by the end of the following modulation period the corresponding phase voltage is calculated and applied to the switching converter. For instance, the command voltage of U_d and U_q can be computed by the following equations in deadbeat control.

$$U_d(k) = -(\frac{L}{T} + \frac{R}{2})[i_d^*(k) - i_d(k)] - Ri_d(k) + \omega L\frac{i_q^*(k) + i_q(k)}{2} + e_d(k) \tag{1.9}$$

$$U_q(k) = -(\frac{L}{T} + \frac{R}{2})[i_q^*(k) - i_q(k)] - Ri_q(k) - \omega L\frac{i_d^*(k) + i_d(k)}{2} + e_q(k) \tag{1.10}$$

where $i_d^*(k)$ and $i_q^*(k)$ are the reference current inputs at sampling instant k. Since the future prediction is made based on the model, it is also often referred to as a direct predictive control in the literature [92]. The calculations are often performed in the synchronous-reference frame, and the space vector modulation strategy is often employed, which very well suits the digital implementation. A control block diagram of a deadbeat control for VSC is depicted in Figure 1.8.

It is known that deadbeat current control technology has faster dynamic response than other digital feedback control, thus it can greatly improve the dynamic performance of VSC. On the other hand, due to the model uncertainties and the inherent delay due to the calculations cause a serious drawback for this technique [24], which may imply an unsatisfactory performance level. In more

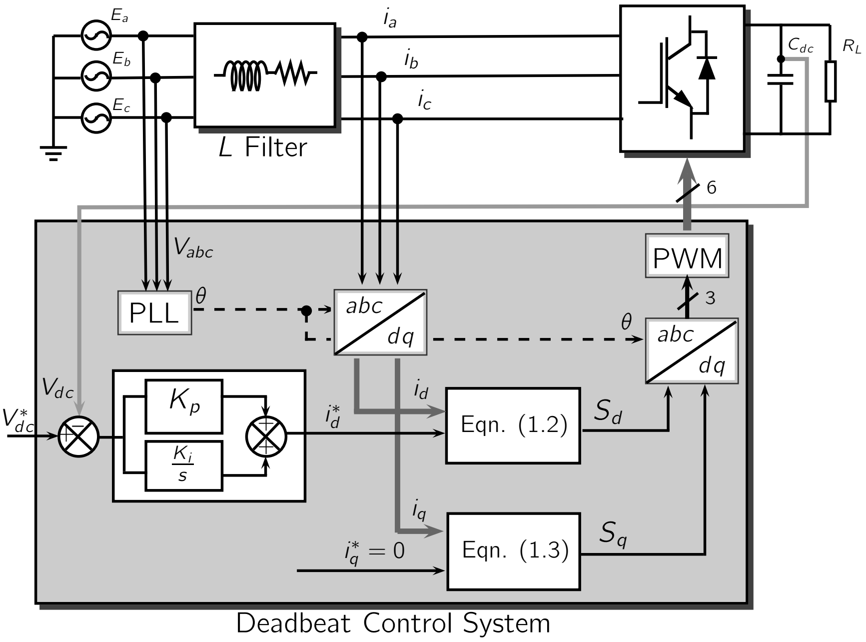

Figure 1.8: Deadbeat control system for grid-connected VSC: i_d^* and i_q^* are the reference input current. Two inner control loop is based on (1.9) and (1.10), where $S_d = U_d/V_{dc}$ and $S_q = U_q/V_{dc}$

recent work of the deadbeat controller, robust issues of deadbeat controller has been addressed using the additional observers or estimators to improve the disturbance rejection and to reduce the sensitivities to the computational delay and the plant uncertainties [58],[37],[46].

Hysteresis Control

The most well known control method without PWM is the hysteresis current control. The basic idea of hysteresis control is to directly control the switches to keep the output current (i_a) trajectories to follow reference current (i_a^*) waveforms within a fixed hysteresis band as shown in Fig. 1.9. In the actual implementation, shown in Fig. 1.10 the feedback error is used with the pre-defined error band for which the switching input is applied to force the error to zero

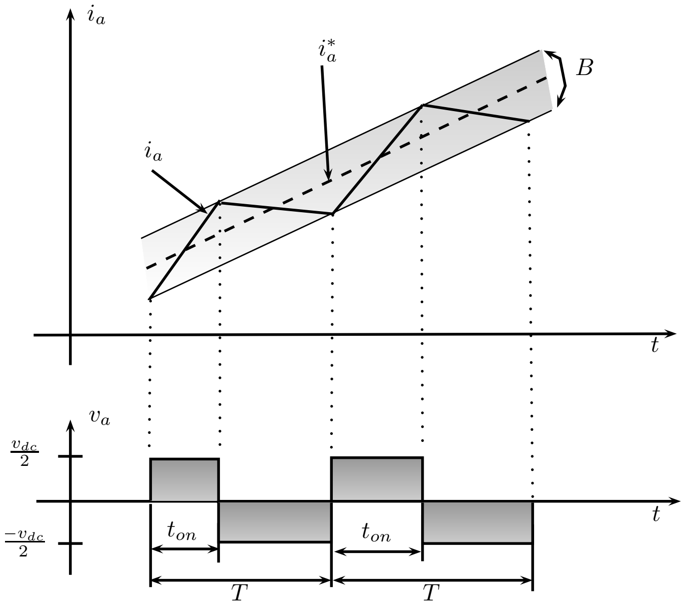

Figure 1.9: Concept of Hysteresis Current Control: B is the hysteresis current band, i_a is the actual phase A current, i_a^* is the reference current for phase. The switching action is applied whenever the actual current touches the hysteresis band to keep the current within the fixed limit

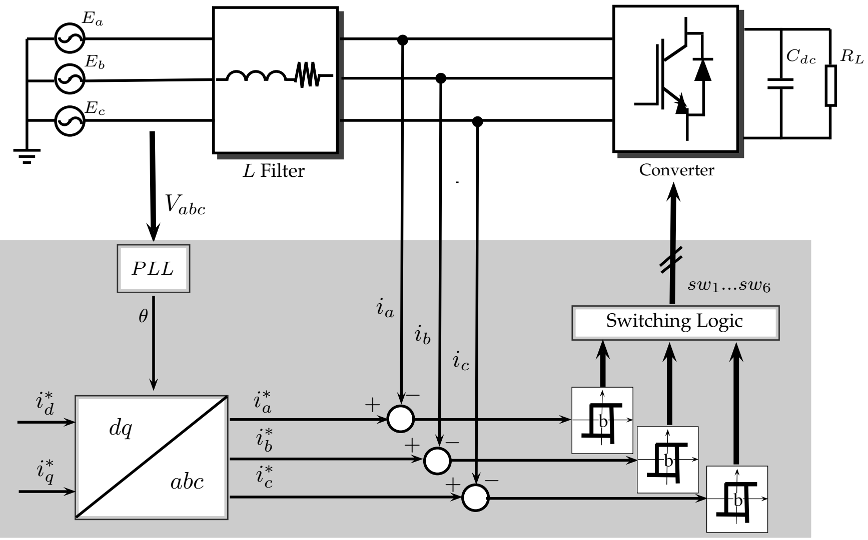

Figure 1.10: Typical hysteresis current control based on error-band comparators to generate the gate signals to the converter: The reference inputs (i_d^* and i_q^*) are generated from the outer control loop.

or origin whenever the error touches the band. As can be seen, an error signal is used to control the switches (i.e.IGBT) in the converter, where the error ($e(t) = i(t) - i^{*}(t)$) is the difference between the desired current, ($i^{*}(t)$), and the current being injected by the converter, ($i(t)$). When the error reaches an upper limit, the switches are opened to force the current down, and if the error reaches a lower limit the switches are closed to force the current to increase. Hence, the range between the lower hysteresis limit and the upper hysteresis limit directly controls the amount of ripple in the output current from the converter.

The main advantage of hysteresis control is the simpler implementation compared to the PWM based control which only requires comparator blocks to determine the correct switching of bipolar switches. Moreover, it is reported that it also leads to a higher dynamic response as well as being robust to parameter variations. However a noticeable disadvantage of this approach is the wide spectrum of the switching frequency, which leads to a stochastic switching losses and it is no longer a linear control. Moreover when applied to a three phase system, the phase errors between the actual and the reference can reach twice the hysteresis band. This is mainly due to the interference between the commutations of the three phases, since each phase current not only depends on the corresponding phase voltage but is also affected by the voltage of the other two phases [74],[23].

Many improvements to the original control structure have been suggested by industrial applications. For example, a three-level comparators with a lookup table is proposed in [68],[13] to reduce the switching frequency by selecting zero voltage vectors, fixed modulation frequency with a variable width of the hysteresis band as function of the instantaneous output voltage [21],[83]. All of these provisions have allowed a substantial improvement in the performance of the hysteresis current controller, as is discussed in [56].

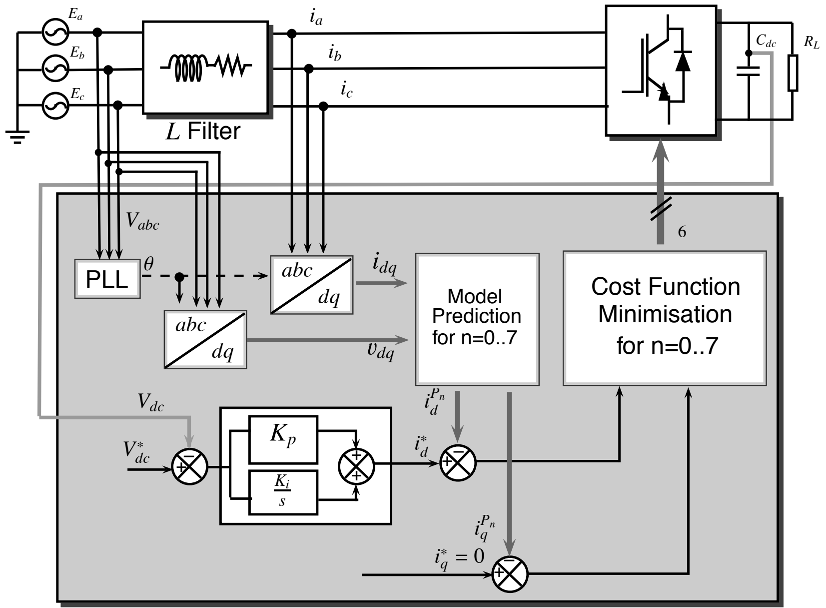

Finite Control Set Predictive Control System

Figure 1.11: Finite control set predictive control system for grid-connected VSC: Model Prediction and Cost Minimisation part is executed iteratively for all possible switching inputs ($n = 1..7$) at each sampling instant. The switching inputs to the converter are directly controlled based on the cost minimisation

Finite-Control-Set Predictive Control

As we described earlier in 'deadbeat control' review section, the concept of predicting the future current behaviour based on the electrical dynamic equation (usually R-L equations for the current control) has long been applied in the control of power converters. However, the most of these earlier predictive or deadbeat controllers use either PWM or SVM techniques to produce switching inputs to the power converter. In recent years, a new control concept called Finite-Control-Set (FCS) predictive control is fast becoming as one of the main control techniques to control the power converters [86],[100],[81],[49],[39].

As explained in the work by Kouro et.al in [100], the main concept that differs from the earlier predictive current control is the use of the cost function to find the optimal switching vector based on the finite number of switching vectors.

Without any fixed modulation, the optimal switching vector is directly applied to switch the converter. More specifically, at each sample time, the output current is predicted for each one of the valid switching states using a model of the converter. Based on the following cost function,

$$J_i = |i^*_{xx} - i^P_{xx}(S_i)| + |i^*_{xx} - i^P_{xx}(S_i)| \;\; fori = 1..7 \tag{1.11}$$

where xx indicates the reference frame which can either be $\alpha\beta$ for the stationary frame and dq for the synchronous reference frame. All the predicted values are evaluated in the cost function and the switching state that minimizes this function is selected to be applied at the next sample time.

The main benefit of the FCS-MPC is the ability to use the different combination of cost terms to consider various performance aspect of the converter, such as switching losses, common-mode voltage reduction etc [100]. For example, to consider increasing the efficiency of the VSC in FCS-MPC, one can choose a cost function of the following form (1.12) that not only penalises the deviation of trajectories from the reference, but also minimises the switching loss [86],[89].

$$J^* = J^p + \lambda \cdot C_p \tag{1.12}$$

where C_p is the number of the switched commutations involved when changing from the present to the future switching state. λ is the associated weighting factor. Hence, the computed optimal control input from the above cost function gives the best possible dynamic response with minimum switching losses by avoiding those switching states that would produce more commutations.

Compared to VOC and other traditional control methods, FCS-MPC is still a relatively new concept, hence there are vast amount of open research problems to be addressed, one of them is to find the guaranteed stability condition for

FCS-MPC [8],[9]. So far in the available literature, only the recent work by Aguilera et.al [8] addressed this issue by applying the terminal cost approach similar to the concept used in the robust MPC problem. Their main idea is to consider the practical stability of FCS-MPC and to design the cost function as a practical Lyapunov function by finding a suitable local controller and the terminal weighting matrix based on the LQR problem.

Other area of concern includes the variable switching frequency and the lack of analytical or numerical solution to obtain an optimal solution to the problem for FSC-MPC. Especially the variable switching frequency problem consequently leads to a spread harmonic spectrum which directly affects the efficiency of the converter.

In many aspects, FCS-MPC approach resembles a classical MPC design. However, as pointed out in number of publications, a discrete minimisation of cost function for possible finite switching states allows an implementation of FCS-MPC to be much simpler and intuitive, even compared to a standard VOC method. Due to this reason and many other advantages of FSC-MPC, a continuous extension of the FCS-MPC to different converter topologies have also been reported for the grid-connected converters [34],[53] for multi-level inverters [90] and for motor drive applications [59],[50]. Recent work by Rodriguez et al.[51], summarises the current state of art of FCS-MPC in power electronics applications.

1.2.3 Model Predictive Control

Model predictive control (MPC), also referred to as receding horizon control, is essentially a class of standard optimal control algorithm that solves the constrained optimal control problem on-line for the current state of the plant by defining a finite horizon. Over the last few decades, MPC has been an active research area from both academic and industries and has become one of the most commonly encountered control methodologies for multivariable control problems. A number of major publications have appeared in the literature, which includes the tutorial papers by Rawlings [94] and Wang [108], an extensive theoretical review paper by Garcia et al. [25], Morari [78], as well as books by Maciejowski [72], Rossiter [97] and Wang [109]. In industry applications, MPC control systems have first appeared in the process industry [25]. Since then the widespread applications of MPC have been reported in the area of chemical process industries, automotive, and power electronics.

The main principle of MPC is to compute the predicted evolution of the system based on the current state at each sampling instant and the state prediction is optimized with respect to some cost function subject to linear inequality constraints. By the receding horizon concept, the first element of the computed sequence of predicted optimal control actions is applied to the plant, and the whole process is repeated for all subsequent sampling. The use of finite horizon and the receding horizon principle is what differentiates from the other optimal control methods and it is the key factor that allows the optimization problem to be solved on-line with a finite number of decision variables and a finite number of constraints.

The most of MPC literatures consider a linear discrete-time system of the following state space form

$$x(k+1) = Ax(k) + Bu(k) \tag{1.13}$$

$$y(k) = Cx(k) \tag{1.14}$$

where $x(k) \in R^n$, $u(k) \in R^m$, $y(k) \in R^p$ denote the state, control input and controlled output respectively. Subsequently the prediction of the model based on the current state for a finite horizon is solved iteratively as shown below,

$$\begin{aligned}
x(k+1) &= Ax(k) + Bu(k) \\
x(k+2) &= Ax(k+1) + Bu(k+1) \\
&= A^2x(k) + ABu(k) + Bu(k+1) \\
&\vdots \\
x(k+N_p) &= A^{N_p}x(k) + A^{N_p-1}Bu(k) + A^{N_p-2}Bu(k+1) \\
&+ A^{N_p-N_c}Bu(k+N_c-1) \qquad (1.15)
\end{aligned}$$

where N_p and N_c denote prediction horizon and control horizon respectively. Generally for a stability purpose, a large N_p is often preferred.

Based on the predicted behaviour of the system, usually a quadratic cost is used to compute the optimal control solution.

$$J = \sum_{i=1}^{N_p}(r(k_i) - y(k_i + N_p)^T Q(r(k_i) - x(k_i + N_p)) + \sum_{i=1}^{N_c} u(k_i + N_c)^T Ru(k_i + N_c) \qquad (1.16)$$

where $r(k_i)$ is the set-point signal for the output y at time k_i, and the weighting matrices Q and R are symmetric positive semi-definite and symmetric positive definite matrices, which are used to tune the optimal performance of MPC.

Without constraints, the objective of model predictive control is to minimise the cost function (1.16) and to find the control law that will drive the predicted plant output $y(k_i+N_p)$ as close as possible to the future trajectory of the set-point $r(k_i)$.

For a continuous-time implementation of MPC, a state-space model of the following form is used

$$\dot{x}_m(t) = A_m x_m(t) + B_m u(t) \tag{1.17}$$

$$y(t) = C_m x_m(t) \tag{1.18}$$

The corresponding state prediction based on the continuous time model is solved based on the following convolution.

$$x(t_i + \tau \mid t_i) = e^{A_m \tau} x(t_i) + \int_0^{\tau} e^{A_m(\tau-\gamma)} B u(\gamma) d\gamma \tag{1.19}$$

Unlike the discrete time case in (1.15), solving the above convolution is computationally more demanding. Due to this reason, the continuous time MPC received a comparatively less attention than the discrete-time counterpart. Major works on continuous time MPC includes Gawthrop et al. [82], Kouvaritakis et al.[16] and Wang [107].

In particular, the work by Wang [107] addresses the apparent difficulties with a continuous time implementation and proposes a method of describing the control trajectory and formulation of constraints using a set of orthonormal basis functions.

By using an augmented system model with embedded integrators, also known as 'velocity'-form model, and assuming that first derivative of control inputs converges exponentially to zero for a chosen control horizon, the control input trajectory is approximated using a set of pre-chosen orthonormal basis functions, which allows the future prediction to be calculated in an analytical form. Based on the model prediction and by defining positive definite matrices (the performance weights), the underlying goal is same as the discrete-time implementation which is to find the optimal control input that minimizes a quadratic cost function with prediction horizon N.

$$J = \int_0^{T_p} x(t_i + \tau \mid t_i)^T Q x(t_i + \tau \mid t_i) d\tau + u^T R_L u \tag{1.20}$$

The detailed summary of the method is described in [109].

One of the key advantages of MPC is the handling of system constraints in the on-line optimisation problem. Since the cost function of MPC is generally chosen to be as a quadratic cost function, a quadratic programming (QP) is used to solve the constrained optimisation problem on-line. Generally, the QP methods can not be solved explicitly and requires an iterative computational approach. From a practical point of view, especially for a fast sampling system, this can also be the one of the main drawbacks of MPC due to the substantial computational load required by the on-line minimisation.

To minimise the computational load, various approaches have been suggested [5],[10]. In particular, the work by Bempoad et al.[5], a method referred to as 'Explicit MPC' has been proposed. The resulting control law of this method is a piecewise-affine (PWA) function of the system state, which uses parametric programming to pre-compute the solution of the optimal control problem for all initial states off-line, and the resulting piecewise-affine control law is stored in a lookup table. Therefore there is no need to solve an optimization problem on-line, and is effective to control fast-sampling systems. However this approach is found to be only feasible for a system with low dimension and a number of constraints.

In contrast to the off-line approach, recent work by Wang [109] uses a computationally efficient QP solver known as Hildreth's programming to solve on-line the quadratic cost function.

Nominal Stability and Feasibility of MPC

Unlike the infinite horizon optimal control problem, the stability and recursive feasibility are not automatically inherited by the finite horizon MPC problem without the pre-setting of parameters, such as weighting matrices Q and R, the length of prediction horizon as well as the terminal cost in the cost function [31],[95]. Typically to ensure the stability of MPC, the cost function of the following form is used which is an extension of (1.16) to include the terminal cost and terminal set constraints.

$$J = \sum_{i=1}^{N_p} \ell(x_i, u_i) + V_f(x_N) \tag{1.21}$$

where $\ell(x_i, u_i) = x^T Q x + u^T R u$, $V_f(x) = x^T P x$. Based on the above cost function, the main idea of guaranteeing the stability is to choose the terminal cost and terminal set, such that the MPC is approximately equal to or an upper bound on the infinite horizon cost and as an invariant subset around the origin respectively.

The exact conditions for which terminal cost and terminal set must satisfy to guarantee the stability and the recursive feasibility are discussed in the seminal paper by Mayne et al. [31].

Robust MPC

Since the control quality of MPC relies heavily on the fidelity of the mathematical model of the underlying plant and because of the fact that there will always be some exogenous disturbances acting on the plant, as well as the presence of uncertainty in the model parameter, the robust aspect of MPC under uncertainty for practical applications is an important topic and have been extensively covered in the literature [18],[73],[31].

Generally for a system with persistent but bounded disturbances, asymptotic stability of the origin can not be achieved but instead under certain conditions the stability of the uncertain system can be achieved by converging the state trajectories to a robust positive invariant set (see Definition 1.2.1), which can be seen as the 'enlarged' origin of the uncertain system [29]. The main goal of robust MPC is therefore to achieve this condition while satisfying the state and control input constraints.

Definition 1.2.1 *(Robust Positive Invariant Set) For the system* $x_{k+1} = Ax_k + \omega_k$, $x_k \in X$, *a set* $\Omega \subseteq \mathbb{R}^n$ *is said to be a robust positive invariant set, if* $Ax_k + \omega_k \in \Omega \subseteq X$, $\forall x \in \Omega$ *and* $\forall \omega_k \subseteq W$.

The seminal work by [26] proposed a method referred to as 'Min-Max Model Predictive Control' which is designed to minimize the worst-case performance achievable under any admissible uncertainty. Under the framework of Min-Max MPC, it is further divided into open-loop and closed-loop min-max MPC.

In open-loop min-max MPC, the worst-case realisation of the uncertainty is minimised over the sequence of open-loop control actions, which often leads to a very conservative solution. In closed-loop min-max MPC, instead of optimising over a nominal control sequence, it optimises a sequence of control policies and thereby introduces a feedback to the disturbances to contain the spread of predicted trajectories resulting from the influence of uncertainty [93].

Another important contribution was made by Kothare et al.[70],[71] which the author used LMI framework to formulate a Min-Max MPC. The main principle of their method is to introduce the control policy for the prediction model which is computed at each time step based on the minimisation of a worst-case upper bound on the infinite horizon cost. Despite the strong theoretical development, many of the Min-Max Robust MPC methods that have been presented in the literature have high computational complexity, which is a major drawback in terms of practicality.

In a more recent work, a method called 'Tube-Based Robust Model Predictive Control' was proposed in Langson et al.[106],[32], to reduce the on-line computational load. The basic concept of Tube-Based Robust MPC is to solve a nominal Model Predictive Control problem for suitably tightened constraints, while bounding the error between nominal1 and uncertain system state by a robust positively invariant set. The method is based on the use of the following form of control input

$$u = \bar{u} + K(x - \bar{x}) \tag{1.22}$$

where $\bar{u}$ and $\bar{x}$ are state and control input of the nominal system. The linear time-invariant feedback controller K, also referred to as the disturbance rejection controller, is computed off-line and ensures that the deviation of the actual system state from the nominal system state is bounded. Tube-Based Robust MPC can be seen as a way of separating the problem of constrained optimal control from the problem of ensuring robustness in the presence of uncertainty.

As was shown in [32], this controller only involves the solution of a standard Quadratic Program which is similar to the conventional MPC which can be solved fast and efficiently using standard mathematical optimization algorithms. Hence Tube-Based Robust MPC can also be applied for fast dynamical systems.

1.3 Objectives

The research objectives of this thesis are:

- To develop voltage and current feedback control systems for grid-connected VSC based on a model predictive control approach: The proposed control system must be applicable to major topologies of grid-connected VSC, and must ensure a fast response to transient events as well as provide good steady-state regulation. Furthermore, the achieved closed-loop performance must be within the physical bounds of the grid-connected VSC.

- To implement the proposed control system on a laboratory scaled grid connected system, to verify the practicality and the control performances.

1.4 Thesis Contribution

Thesis presents several key contributions to the application of MPC in the field of power electronic converters.

The first contribution of this thesis is the development of a model predictive voltage controller (MPVC) which offers a centralised control structure to regulate both DC-bus voltage and input currents in the synchronous reference frame. In order to reduce the complexity of tuning, explicit tuning techniques based on a regional pole placement method are presented to confine the closed-loop poles of MPVC in the desired region of the complex plane. So the extensive tuning of cost-weighting factors are avoided and offers a systematic way of tuning the MPVC to satisfy desired closed-loop responses. Furthermore, the parameter uncertainties, especially the grid impedance variation is considered and also presents a systematic way of designing a MPVC to ensures the robust stability. Lastly, a constrained optimisation problem with switching control input constraints is formulated and implemented in the synchronous reference frame to regulate the closed-loop response of the proposed controller to be within a linear modulation region.

The second major contribution of this thesis is the development of a model predictive current controller for grid-connected VSC with an LCL filter. A novel current control system which consists of nominal and disturbance rejection controller is proposed to ensure a good tracking performance of the input current in the synchronous reference frame while sufficiently suppressing the resonance harmonics caused by the LCL filter. For the disturbance rejection controller, the concept of finite frequency H_∞ control is employed to reject the LCL resonant harmonics in a finite frequency interval which improves the damping of LCL filter harmonics compared to other traditional methods. In order to ensure the system constraints are satisfied, an approach similar to the constraint tightening approach is used to ensure the feasibility of switching input constraints while rejecting LCL filter harmonics.

The third contribution is the development of a model predictive resonant current controller (MPRC) for a grid-connected VSC. The presented MPRC embeds a sinusoidal module in the original model to track the sinusoidally varying reference inputs and the measured system states in the stationary reference frame. A grid-frequency variation problem is considered and a robustly stabilising controller has been proposed to improve the robust tracking of reference input current for different grid frequencies. The selective harmonic compensation controller is also proposed to minimise the odd-order harmonics in the grid-side current caused by the grid-voltage harmonics. Model based harmonic compensator along with MPRC is designed to ensure a sufficient reduction of the harmonics while ensuring the stability and the tracking performance of reference inputs.

The last contribution of this thesis is the development of a finite-control-set MPC (FCS-MPC) with state constraints. The main idea of this contribution is to augment a general cost-function of FCS-MPC with linear inequalities such that both initial and final states (input currents) are confined within the maximal admissible set that satisfies input and state constraints. The optimal switching input from the finite control set is computed based on the concept of dual-model control to ensure that the initial state in a relaxed final state constraint is steered towards an invariant set around the equilibrium/reference point for ensuring the stability. The presented concept is applied to a grid-connected VSC and verified in the experimental tests.

1.4.1 List of Publications

1. D. K. Yoo and L. Wang. "Predictive Control of a Three-Phase Regenerative PWM converter using a Prescribed Degree of Stability". 18th IFAC World Congress, Milan, Aug, 2011.

2. D. K. Yoo and L. Wang. "A model predictive resonant controller for grid-connected voltage source converters". 37th Annual Conference of IEEE Industrial Electronics Society, IECON, Melbourne, 2011.

3. D. K. Yoo, L. Wang and P. Gawthrop. "Predictive Control of a Three-Phase Regenerative PWM converter using a Prescribed Degree of Stability". System Identification, Environmental Modelling, and Control System Design, Springer, 2012

4. D. K. Yoo and L. Wang. " Constrained predictive control of three-phase voltage source converters with explicit performance specifications". 38th Annual Conference of IEEE Industrial Electronics Society, IECON, Montreal, 2012.

5. L. Wang, S. Chai, D, K. Yoo, L. Gan and K. Ng. "PID and Predictive Control of Electric Drives and Power Converters using MATLAB/Simulink", To appear in 2014, Wiley.

1.5 Thesis Organisation

The thesis consists of 6 chapters and 2 appendices which are organised as follows.

Chapter 2 presents a control-oriented linear model of a three phase voltage source converter which is derived from a nonlinear model using a well-known technique called state averaging method. Based on the state averaged model, separate linear models of the converter are derived in both the synchronous reference frame and stationary frame which will be used for the control design.

Chapter 3 presents a multi-variable control scheme based on a general framework of model predictive control. The presented control scheme departs from the conventional cascaded control, and constructs an unified controller that regulates both DC-bus voltage and input currents based on the state-averaged model of the VSC in the synchronous reference frame. In order to reduce the complexity of tuning, pre-stabilisation techniques are presented to satisfy desired closed-loop response and to improve the numerical conditioning of the predictive controller with a long prediction horizon. In order to keep the modulation index of switching control input to within a linear region, a constrained optimisation with switching control input constraints are formulated and implemented in the synchronous reference frame.

Chapter 4 presents MPC based control of three phase VSC with an LCL filter. An identification of frequency characteristics of the LCL filter is presented first to analyse the resonance frequency of LCL filter. Following from the identification, a novel MPC based current control method is presented based on the reduced-order model of LCL filter. The proposed scheme comprises of nominal and disturbance rejection control parts where each part of control is designed separately. For the disturbance rejection control, a finite-frequency H_∞ control method is adopted to reduce the effect of resonance of LCL filter.

Chapter 5 presents a model predictive control scheme that tracks periodic reference current inputs of i_α and i_β in the stationary frame. The main idea of the proposed scheme is based on the internal model principle which embeds the resonant module of $\frac{1}{s^2+\omega^2}$ in the model of VSC in the stationary frame. From this model, the future prediction of states and optimum switching inputs are computed by minimizing the error function between the predicted and measured input currents (i_α and i_β). An extension of MPRC is presented to selectively compensate for multiple harmonics caused by the grid voltage harmonics. The proposed scheme controls the nominal current dynamics as well as the harmonic at a specific frequency by resonant harmonic compensator which ensures the overall system stability in the presence of harmonic distortions.

Chapter 6 presents a FCS-MPC scheme with state constraints, where the proposed scheme handles the system constraints on-line while minimising the cost function based on a one-step ahead prediction. An application of the proposed FCS-MPC scheme to VSC is explained and simulation and experimental results are presented for the analysis.

Chapter 2

Mathematical Model

This chapter presents a mathematical model of grid-connected VSC, which will form a basis of the model predictive control design proposed in this thesis.

In section 2.1, a control-oriented model is first derived based on the operation principle of a three phase VSC by using a well-known method called state averaging method. In sections 2.2 and 2.3, a linearised model of VSC is derived using the concept of synchronous-reference frame and the stationary-frame transformations, which allows dynamics of the linearised model to transform from time-varying to time-invariant. In the last section, a brief discussion on the design constraint for VSC in grid-connected applications is presented.

2.1 Nonlinear Model

Before proceeding to the model derivation, several assumptions are made about the operation of the converter. First, it is assumed that all switches are ideal and operate in a continuous conduction mode (CCM), and the grid voltage is symmetric and balanced as follows.

$$E_a = E_m \sin(\omega t) \tag{2.1}$$

$$E_b = E_m \sin(\omega t + \frac{2\pi}{3}) \tag{2.2}$$

$$E_c = E_m \sin(\omega t + \frac{4\pi}{3}) \tag{2.3}$$

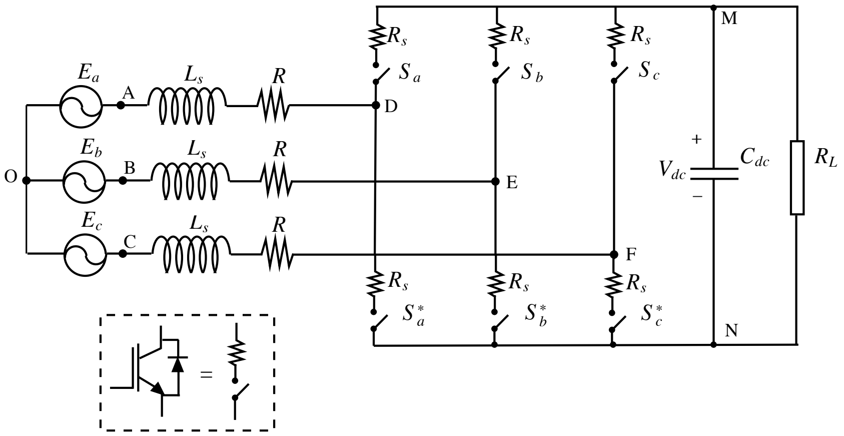

Figure 2.1: Grid-connected three phase voltage source converter

where $\omega = 2\pi f$, f is the grid frequency. Furthermore, the system is assumed to be a three wire system, thus the sum of three phase currents and voltage are equal to zero.

$$I_a + I_b + I_c = 0 \tag{2.4}$$

$$V_{an} + V_{bn} + V_{cn} = 0 \tag{2.5}$$

Based on these assumptions, voltage equations for each phase are written as follows.

$$E_a = L_s \frac{di_a}{dt} + Ri_a + V_{dn} + V_{no} \tag{2.6}$$

$$E_b = L_s \frac{di_b}{dt} + Ri_b + V_{en} + V_{no} \tag{2.7}$$

$$E_c = L_s \frac{di_c}{dt} + Ri_c + V_{fn} + V_{no} \tag{2.8}$$

The symbol $[S_i, S_i^*]$ in Figure 2.1 denotes a bipolar switching input $[0, 1]$ for an upper and lower leg of each phase respectively. Since these switching inputs are conducted in a complementary manner, $S_a + S_a^* = 1$ (i.e. only one of the switch is allowed to conduct in any one time), two linear equations are obtained for V_{dn}, V_{en}, V_{fn}. For example,

$$V_{dn} = \begin{cases} I_a R_s + V_{dc}, & S_a = 1 \\ I_a R_s, & S_a^* = 1 \end{cases} \tag{2.9}$$

where R_s is the equivalent resistance of switching device. Now, substituting (2.9) into (2.6) yields

$$E_a = L\frac{di_a}{dt} + Ri_a + (I_a R_s + V_{dc})S_a + (I_a R_s)S_a^* + V_{no} \tag{2.10}$$

Since $S_a + S_a^* = 1$, it is further simplified to

$$E_a = L\frac{di_a}{dt} + Ri_a + (V_{dc}S_a + V_{no}) \tag{2.11}$$

The same procedure can be applied for phase B and C, to yield the similar expressions,

$$E_b = L\frac{di_b}{dt} + Ri_b + (V_{dc}S_b + V_{no}) \tag{2.12}$$

$$E_c = L\frac{di_c}{dt} + Ri_c + (V_{dc}S_c + V_{no}) \tag{2.13}$$

Based on the assumptions made in (2.4) and (2.1), the equation for V_{no} is given by adding (2.11)–(2.12) together,

$$V_{no} = \frac{-V_{dc}}{3}\sum_{k=1}^{3} S_k \tag{2.14}$$

For the DC-side of the converter, it can be written as

$$C\frac{dV_{dc}}{dt} = I_{dc} - I_L \tag{2.15}$$

$$= \frac{S_a I_a}{2} + \frac{S_b I_b}{2} + \frac{S_c I_c}{2} - I_L \tag{2.16}$$

In a more compact form, the converter model is written in a state-space form as follows,

$$\begin{bmatrix} \frac{d}{dt}i_a \\ \frac{d}{dt}i_b \\ \frac{d}{dt}i_c \\ \frac{d}{dt}V_{dc} \end{bmatrix} = \begin{bmatrix} -\frac{R}{L_s} & 0 & 0 & \frac{S'_a}{L_s} \\ 0 & -\frac{R}{L_s} & 0 & \frac{S'_b}{L_s} \\ 0 & 0 & -\frac{R}{L_s} & \frac{S'_c}{L_s} \\ \frac{S_a}{C_{dc}} & \frac{S_b}{C_{dc}} & \frac{S_c}{C_{dc}} & 0 \end{bmatrix} \begin{bmatrix} i_a \\ i_b \\ i_c \\ V_{dc} \end{bmatrix} + \begin{bmatrix} \frac{E_a}{L_s} \\ \frac{E_b}{L_s} \\ \frac{E_c}{L_s} \\ 0 \end{bmatrix} \tag{2.17}$$

where S'_{abc} are given as

$$S'_a = S_a - \frac{1}{3}(S_a + S_b + S_c) \tag{2.18}$$

$$S'_b = S_b - \frac{1}{3}(S_a + S_b + S_c) \tag{2.19}$$

$$S'_c = S_c - \frac{1}{3}(S_a + S_b + S_c) \tag{2.20}$$

A further simplification of the model in (2.17) is possible given that a PWM switching frequency is assumed to be much higher (i.e typically $\gg 1\ KHz$) than a grid frequency (i.e $50Hz$ in this work). Based on such assumptions the switching functions (S_a, S_b, S_c) can be approximated by their averaged function (i.e duty-ratio) as follows:

$$d_a = \frac{m\cos(\omega t) + 1}{2} \tag{2.21}$$

$$d_b = \frac{m\cos(\omega t - \frac{2\pi}{3}) + 1}{2} \tag{2.22}$$

$$d_c = \frac{m\cos(\omega t + \frac{2\pi}{3}) + 1}{2} \tag{2.23}$$

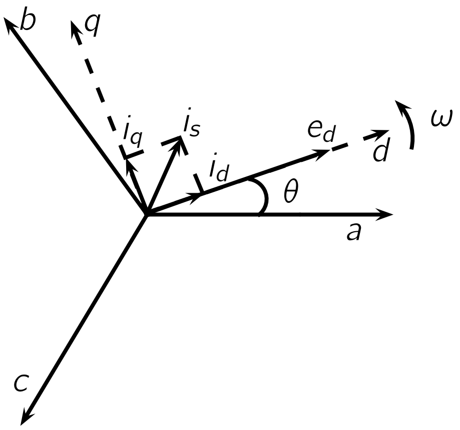

Figure 2.2: Phasor diagram of synchronous reference frame: d-axis is aligned with the grid voltage and the d-axis lags the q-axis by $90°$.

This type of approximation in the model is known as a state-averaging method. For a detailed derivation and proof of the method can be found in [91].

Now, by substituting the (2.21)–(2.23) into (2.17), a continuous-time model of the VSC is obtained as

$$\begin{bmatrix} \frac{d}{dt}i_a \\ \frac{d}{dt}i_b \\ \frac{d}{dt}i_c \\ \frac{d}{dt}V_{dc} \end{bmatrix} = \begin{bmatrix} -\frac{R}{L_s} & 0 & 0 & \frac{m\cos(\omega t)}{L_s} \\ 0 & -\frac{R}{L_s} & 0 & \frac{m\cos(\omega t-\frac{2\pi}{3})}{L_s} \\ 0 & 0 & -\frac{R}{L_s} & \frac{m\cos(\omega t+\frac{2\pi}{3})}{L_s} \\ \frac{m\cos(\omega t)+1}{C_{dc}} & \frac{m\cos(\omega t-\frac{2\pi}{3})+1}{C_{dc}} & \frac{m\cos(\omega t+\frac{2\pi}{3})+1}{C_{dc}} & 0 \end{bmatrix} \begin{bmatrix} i_a \\ i_b \\ i_c \\ V_{dc} \end{bmatrix} + \begin{bmatrix} \frac{E_a}{L_s} \\ \frac{E_b}{L_s} \\ \frac{E_c}{L_s} \\ 0 \end{bmatrix} \tag{2.24}$$

2.2 Synchronous-Reference-Frame Axis

The dynamic equations of the converter given in (2.17) are time-varying and nonlinear. For the purpose of controller design, it is preferable to transform the

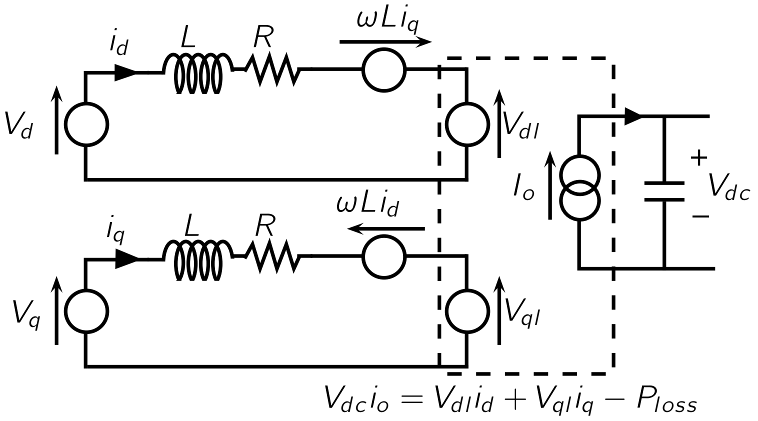

Figure 2.3: Equivalent circuit of three-phase VSC in the synchronous reference frame: P_{loss} is the total power loss which mainly consist of switching and conduction losses.

non-linear model into a linear time-invariant (LTI) model. First, a synchronous-reference frame transformation, also known as d-q axis transformation is applied to (2.17) to obtain a time-invariant equivalent model. An in-depth treatment of the synchronous-reference frame transformation is not presented in this work, however a transformed model can simply be obtained by applying the matrix given below.

$$T = \begin{bmatrix} cos(\omega t) & cos(\omega t - \frac{2\pi}{3}) & cos(\omega t - \frac{4\pi}{3}) \\ -sin(\omega t) & -sin(\omega t - \frac{2\pi}{3}) & -sin(\omega t - \frac{4\pi}{3}) \end{bmatrix} \tag{2.25}$$

The phasor diagram and the equivalent circuit of a three-phase VSC in synchronous reference frame aligned with grid voltage at ω frequency is shown in Figure 2.2 and Figure 2.3 respectively. After applying the transformation to (2.17), dynamic equations of the VSC in synchronous-reference axis are expressed as,

$$L_s \frac{di_d}{dt} = -Ri_d + \omega L_s i_q + e_d - v_d \tag{2.26}$$

$$L_s \frac{di_q}{dt} = -v_q - Ri_q - \omega L_s i_d \tag{2.27}$$

$$C_{dc} \frac{dv_d}{dt} = \frac{3}{4}\left(S_d i_d + S_q i_q\right) - i_L \tag{2.28}$$

where e_d is a grid source voltage, i_d, i_q are the input currents and v_d , v_q denotes control inputs, which are defined as below,

$$v_d = S_d * (v_{dc}/2) \tag{2.29}$$

$$v_q = S_q * (v_{dc}/2) \tag{2.30}$$

S_d and S_q are switching functions. Note that with the switching functions S_d and S_q as control variables, (2.26)-(2.28) become a set of bilinear equations.

Supposing that at steady state operating condition, the converter maintains a target DC bus voltage with unity power factor, in other words both the magnitude of i_{qo} and v_q are assumed to be zero, then the steady state values of the parameters in the linear model are selected as $i_{qo} = 0, v_q = 0, V_{dco} = V_{ref}$. For steady-state switching functions S_{do}, S_{qo} are computed as ([57]),

$$S_{do} = \frac{2(V_d - Ri_d)}{V_{dco}} \tag{2.31}$$

$$S_{qo} = \frac{-2\omega L_s i_d}{V_{dco}} \tag{2.32}$$

Therefore by linearising the bilinear model of VSC using the above operating point calculation, the linear time-invariant model can be obtained as follows

$$\dot{X}_m(t) = A_m X_m(t) + B_m u(t) \tag{2.33}$$

$$y(t) = C_m X_m(t) \tag{2.34}$$

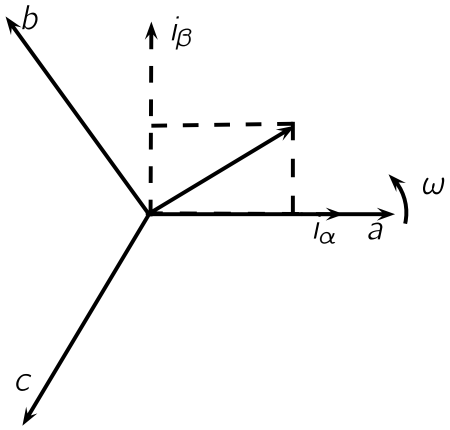

Figure 2.4: Phasor diagram of stationary frame: α-axis is aligned with a-phase and the orthogonal α–β axis does not rotate with respect to the three phase axis at ω frequency.

where A_m, B_m and X_m are defined as,

$$A_m = \begin{bmatrix} -\frac{R}{L_s} & \omega & -\frac{S_{do}}{2L_s} \\ -\omega & -\frac{R}{L_s} & -\frac{S_{qo}}{2L_s} \\ \frac{3S_{do}}{4C_{dc}} & \frac{3S_{qo}}{4C_{dc}} & 0 \end{bmatrix}, B_m = \begin{bmatrix} \frac{-v_{dco}}{2L_s} & 0 \\ 0 & \frac{-v_{dco}}{2L_s} \\ \frac{3i_{do}}{4C_{dc}} & \frac{3i_{qo}}{4C_{dc}} \end{bmatrix}, \tag{2.35}$$

$$C_m = \begin{bmatrix} 0 & 1 & 0 \\ 0 & 0 & 1 \end{bmatrix}, X_m = \begin{bmatrix} i_d \\ i_q \\ v_{dc} \end{bmatrix}, u = \begin{bmatrix} S_d \\ S_q \end{bmatrix} \tag{2.36}$$

where $S_{do}, S_{qo}, V_{dco}, i_{do}$ and i_{qo} represents steady state equivalent solutions.

2.3 Stationary-Frame Axis

Another transformation commonly used is called a stationary frame transformation, also known as α-β frame transformation. As shown in Figure 2.4, in

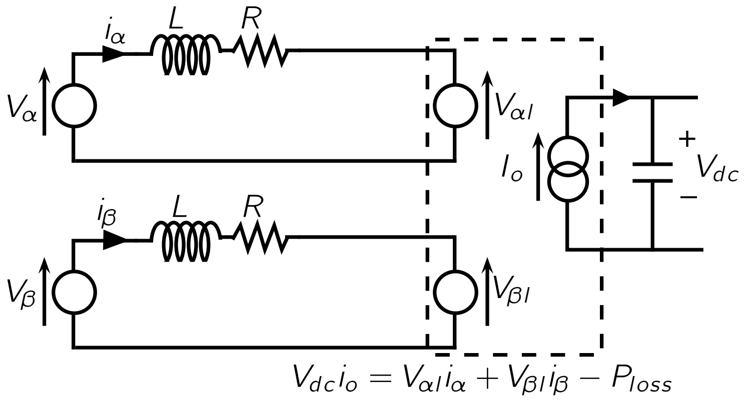

Figure 2.5: Equivalent circuit of three-phase VSC in the stationary frame: P_{loss} is the total power loss which mainly consist of switching and conduction losses.

this frame the three-phase vectors are projected into a stationary orthogonal vectors, where the projected two-axis vectors remain stationary with respect to three-phase vector rotating at ω. Mathematically, the SF transformation can be obtained by applying the matrix below.

$$T_{\alpha\beta} = \begin{bmatrix} 1 & -\frac{1}{2} & -\frac{1}{2} \\ 0 & \frac{\sqrt{3}}{2} & -\frac{\sqrt{3}}{2} \end{bmatrix} \tag{2.37}$$

Due to the omission of phase angle in (2.37), the computation is simpler compared to the synchronous-reference transformation, where the grid synchronisation is also no longer needed. However it is important to note that the stationary frame transformed variables such as current and voltage vary sinusoidally at the grid frequency.

By applying the stationary frame transformation to (2.17), a three phase

VSC model in terms of i_α and i_β in the stationary frame can be expressed as,

$$L_s \frac{di_\alpha}{dt} = -Ri_\alpha + e_\alpha - v_\alpha \tag{2.38}$$

$$L_s \frac{di_\beta}{dt} = -Ri_\beta + e_\beta - v_\beta \tag{2.39}$$

where e_α,e_β and i_α, i_β are the stationary frame grid voltages and input currents respectively. v_α and v_β denote control inputs with

$$v_\alpha = \frac{S_\alpha v_{dc}}{2} \tag{2.40}$$

$$v_\beta = \frac{S_\beta v_{dc}}{2} \tag{2.41}$$

where S_α and S_β are switching functions. The DC-link bus voltage equation can be expressed as,

$$C\frac{dv_{dc}}{dt} = \frac{3(S_\alpha \cdot i_\alpha + S_\beta \cdot i_\beta)}{4} - \frac{v_{dc}}{R_L} \tag{2.42}$$

The equivalent circuit of three-phase VSC in synchronous reference frame is shown in Figure 2.5, compared to the synchronous reference frame in Figure 2.3, a cross-coupling terms do exist.

Considering only the dynamics of i_α and i_β, the above model is linearized and casted into the state-space form below,

$$\dot{x}_m(t) = A_m x_m(t) + B_m u(t) \tag{2.43}$$

$$y(t) = C_m x_m(t) \tag{2.44}$$

where A_m, B_m and C_m are defined as

$$A_m = \begin{bmatrix} -\frac{R}{L_s} & 0 \\ 0 & -\frac{R}{L_s} \end{bmatrix}, B_m = \begin{bmatrix} \frac{-v_{dco}}{2L_s} & 0 \\ 0 & \frac{-v_{dco}}{2L_s} \end{bmatrix}$$

$$C_m = \begin{bmatrix} 1 & 0 \\ 0 & 1 \end{bmatrix}, x_m = \begin{bmatrix} i_\alpha \\ i_\beta \end{bmatrix}, u = \begin{bmatrix} S_\alpha \\ S_\beta \end{bmatrix}$$

v_{dco} is the chosen operating voltage of the DC-link bus.

Chapter 3

Model Predictive Voltage Control

3.1 Introduction

The objective of the control system for the VSC is to regulate DC-bus voltage to follow the reference value, while the line current should be sinusoidal shape and in phase with the grid voltage. A control system of the VSC to achieve this objective often employs a cascaded control structure in which DC-bus voltage and current controllers are designed and tuned separately. Predominantly in the literature, PI controllers are used for each control loops where an outer-loop voltage controller generates reference value of current for the inner controller.

In this chapter, departing from the conventional cascaded PI control, a multivariable structure of the MPC is utilised to construct a centralized controller that regulates both DC-bus voltage and input currents based on the state-averaged model of the VSC in the synchronous reference frame (herein referred to as Model Predictive Voltage Controller (MPVC)). An overview of the complete control structure of MPVC with a grid connected VSC is shown in Figure 3.1.

In section 3.3, a concept known as *Prescribed Degree of Stability* is introduced to simplify the tuning of MPVC. The presented method allows a simple weighting matrix in the quadratic cost function and introduces a scalar parameter as an exponential weighting factor on the cost function to tune the minimum decay rate of the closed-loop response.

In section 3.4, an extension of *Prescribed Degree of Stability and Damping* is proposed to consider a more complex performance requirement such as min-

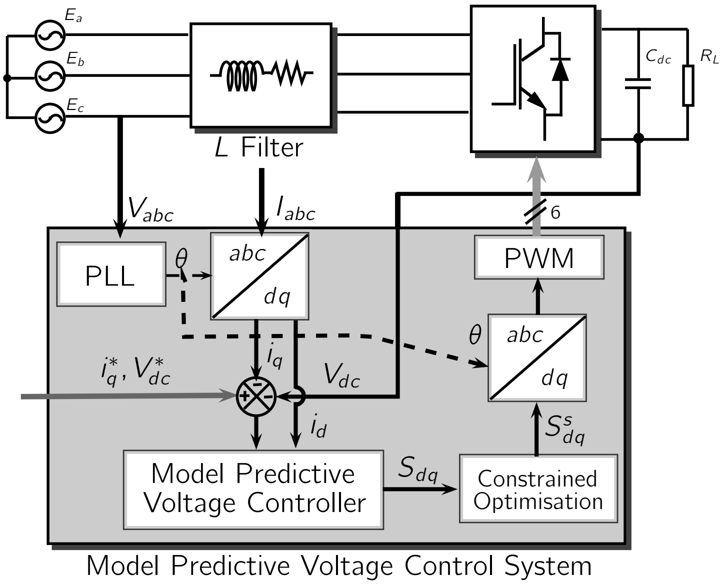

Figure 3.1: The control block diagram of the proposed model predictive voltage control (MPVC)

imum damping and decay rate. A desired region in the complex plane based on the minimum damping and decay rate requirements is defined and formulated in terms of LMI expressions and solved using a LMI solver. The resulting state-feedback law which satisfies the performance requirements of the closed-loop system is then employed into the finite horizon optimisation problem using the technique known as the *Closed-Loop Paradigm* [97].

Section 3.5 explains Laguerre function based MPC design technique which parametrises the control trajectories and solves a quadratic cost function with the parametrised control inputs. Furthermore, the switching constraints used for VSC application is explained and formulated as a linear constraints. To close the chapter, experimental validations of all proposed methods are presented.

3.2 Mathematical Model

The model of the VSC used in this section is based on the synchronous-reference frame model in (2.33)) which is reproduced in the following

$$\dot{x}_m(t) = A_m x_m(t) + B_m u(t) \tag{3.1}$$

$$y(t) = C_m x_m(t) \tag{3.2}$$

where A_m, B_m, C_m and X_m are defined as

$$A_m = \begin{bmatrix} -\frac{R}{L_s} & \omega & -\frac{S_{do}}{2L_s} \\ -\omega & -\frac{R}{L_s} & -\frac{S_{qo}}{2L_s} \\ \frac{3S_{do}}{4C_{dc}} & \frac{3S_{qo}}{4C_{dc}} & 0 \end{bmatrix}, B_m = \begin{bmatrix} \frac{-v_{dco}}{2L_s} & 0 \\ 0 & \frac{-v_{dco}}{2L_s} \\ \frac{3i_{do}}{4C_{dc}} & \frac{3i_{qo}}{4C_{dc}} \end{bmatrix}, \tag{3.3}$$

$$C_m = \begin{bmatrix} 0 & 1 & 0 \\ 0 & 0 & 1 \end{bmatrix}, x_m = \begin{bmatrix} i_d \\ i_q \\ v_{dc} \end{bmatrix}, u = \begin{bmatrix} S_d \\ S_q \end{bmatrix} \tag{3.4}$$

In the synchronous-reference frame, the reference inputs for i_d^* and i_q^* currents, DC-bus voltage (V_{dc}^*) as well as the physical measurements of i_d, i_q and V_{dc} are converted into DC vector quantities. So for a controller in the synchronous-reference frame an integral action is required to achieve a zero steady-state error. One way of integral action in the MPC framework is to embed integrators for output variables in the above model, where the output variables of the interest in this case are DC-bus voltage (V_{dc}) and reactive current (i_q). To embed the integrator, two auxiliary variables are first chosen as

$$z(t) = \dot{x}_m(t) \tag{3.5}$$

$$y(t) = C_m x_m(t) \tag{3.6}$$

and based on them, a new state variable vector is defined as $x(t) = [z(t)^T \;\; y(t)^T]^T$, where $y(t) = [i_q \;\; V_{dc}]$. With these auxiliary variables, in conjunction with the original plant model, the augmented state space model is defined as:

$$\begin{bmatrix} \dot{z}(t) \\ \dot{y}(t) \end{bmatrix} = \overbrace{\begin{bmatrix} A_m & 0_{3\times2}^T \\ C_m & 0_{2\times2} \end{bmatrix}}^{A} \overbrace{\begin{bmatrix} z(t) \\ y(t) \end{bmatrix}}^{x} + \overbrace{\begin{bmatrix} B_m \\ 0_{2\times2} \end{bmatrix}}^{B} \overbrace{\begin{bmatrix} \dot{S}_d(t) \\ \dot{S}_q(t) \end{bmatrix}}^{\dot{u}} \tag{3.7}$$

$$y(t) = \underbrace{\begin{bmatrix} 0_{2\times3} & I_{2\times2} \end{bmatrix}}_{C} \begin{bmatrix} z(t) \\ y(t) \end{bmatrix} \tag{3.8}$$

where $I_{2\times2}$ is the identity matrix with dimensions 2×2, $0_{3\times2}$ is a 3×2 zero matrix, $0_{2\times2}$ is a 2×2 zero matrix and $0_{2\times3}$ is a 2×3 zero matrix. Note that the control input to the above model is the derivative of the actual control signal. From hereafter the model in (3.7) and (3.8) are used for the control design.

3.3 Prescribed Degree of Stability

In the continuous-time setting of MPC, the model prediction is given by

$$x(t_i + \tau \mid t_i) = e^{A\tau}x(t_i) + \int_0^{\tau} e^{A(\tau-\gamma)}Bu(\gamma)d\gamma \tag{3.9}$$

where in general the plant model A is assumed to be stable and a long prediction horizon is chosen to give a stable closed loop response. But for the case of marginally stable/unstable system, such as the augmented system matrix in (3.7 and 3.8) which has three poles on the origin of the complex plane, the prediction computation becomes numerically ill-conditioned with a long prediction horizon [109],[97]. Therefore, there is a need to improve the numerical conditioning of the model prediction in (3.9). One approach to predictive control with *Prescribed Degree of Stability* has been developed in [109] and applied to the VSC in [112] where the resulting design overcomes the numerical ill-conditioning problem by applying exponential weighting factor on the system states. The following section describes the *Prescribed Degree of Stability* method developed in [109] which involves two steps of pre-conditioning the system matrix in the cost function. Following from this, Robust Prescribed Degree of Stability method is presented to consider the model parameter uncertainties.

3.3.1 Pre-stabilisation

As a first step of pre-conditioning, a constant α is chosen as an exponential weighting factor on states $x(t)$ as follows.

$$x_\alpha(t) = e^{-\alpha t}x(t) \tag{3.10}$$

Differentiating the above with respect to time gives

$$\begin{aligned}
\dot{x}_\alpha(t) &= -\alpha e^{-\alpha t}x(t) + e^{-\alpha t}\dot{x}(t) && (3.11)\\
&= A_\alpha x_\alpha(t) + B\dot{u}_\alpha(t) && (3.12)
\end{aligned}$$

where $A_\alpha = A - \alpha I$ and $\dot{u}_\alpha = e^{\alpha t}\dot{u}(t)$. For an appropriate choice of α, the prediction of the state variables based on $(A-\alpha I)$ is numerically well conditioned (i.e. stable eigenvalues) and prediction horizon T_p can be selected sufficiently large to capture the transformed state variable response. In the case where the plant is unstable with all its eigenvalues lying to the left of the line $s = -\varepsilon$ line in the complex plane, where $\varepsilon > 0$, $\alpha > \varepsilon$ is required.

Now, by using the transformed state x_α and assuming that at the current time, say t_i, the state variable vector $x(t_i)$ is measured. The predicted state vector, denoted by $x_\alpha(t_i + \tau \mid t_i)$ at the future time τ, $\tau > 0$, is described by the following equation

$$x_\alpha(t_i + \tau \mid t_i) = e^{A_\alpha \tau} x(t_i) + \int_0^\tau e^{A_\alpha(\tau - \gamma)} B\dot{u}_\alpha(\gamma) d\gamma \tag{3.13}$$

Based on the above prediction, a cost function with a finite horizon of the form below is used in MPC

$$J = \int_0^{T_p} x_\alpha(t_i + \tau \mid t_i)^T Q x_\alpha(t_i + \tau \mid t_i) d\tau + \dot{u}_\alpha^T R_L \dot{u}_\alpha \tag{3.14}$$

where Q and R_L are symmetric positive definite and positive semi-definite matrices, written as $Q > 0$ and $R_L \geq 0$ respectively. The use of exponential data weighting ($e^{-\alpha t}$) alters the original closed-loop performance as specified by the cost function weighting matrices Q and R and in order to compensate for this variation, the Q matrix is replaced by

$$Q_\alpha = Q + 2\alpha P \tag{3.15}$$

where P is based on the solution of the Riccati equation for the cost function of (3.68) with infinite horizon.

$$PA + A^T P - PBR^{-1}B^T P + Q = 0 \tag{3.16}$$

It is easy to see from the following that

$$J = \int_0^{T_p} x_\alpha(t_i + \tau \mid t_i)^T Q_\alpha x_\alpha(t_i + \tau \mid t_i) d\tau + \dot{u}_\alpha^T R_L \dot{u}_\alpha \tag{3.17}$$

To this end, a positive constant α is used to improve the numerical conditioning of predictive formulation by applying the exponential weighting factor on the original matrix A. As such, we can assume that a predictive controller with the augmented model of the converter with a sufficient value of α gives a stable response for a relatively large prediction horizon (T_p). In fact, in the absence of constraints, it is known that if exponential data weighting is employed then the predictive controller converges to the corresponding linear quadratic regulator with sufficiently large prediction horizon T_p [109].

3.3.2 Prescribed Degree of Stability

Now, if Q in (3.68) is simply chosen as $Q = C^T C$, the closed-loop poles of the predictive control system follows the stable branches of the symmetric root-locus, dictated by the choice of the weight coefficient r_w ($R = r_w I$).

$$det(I + \frac{1}{r_w}\frac{G(s)G(-s)}{s(-s)}) = 0 \tag{3.18}$$

where $G(s) = C_m(sI_{n_1} - A_m)^{-1}B_m$ is the Laplace transfer function of VSC. The stable branches of the symmetric root-locus provide limited options for the desired closed-loop eigenvalues in the design [110]. In order to overcome such performance limitations with a simple Q matrix, we introduce Prescribed Degree of Stability method, which was first proposed by B.O Anderson and Moore [12] in the context of LQR design. The main idea of this method is to improve the stability margin of the original system by shifting the closed-loop eigenvalue placement through a positive scalar factor β while minimizing the quadratic cost function.

$$J = \int_0^{\infty} e^{2\beta t}\left[x(t)^T Qx(t) + \dot{u}(t)^T R\dot{u}(t)\right] dt \tag{3.19}$$

subject to

$$\dot{x}(t) = Ax(t) + B\dot{u}(t) \tag{3.20}$$

For a positive scalar factor $\beta > 0$, we can denote

$$\dot{x}_\beta(t) = e^{\beta t}x(t), \;\; u_\beta(t) = e^{\beta t}u(t) \tag{3.21}$$

Then, the minimisation of the cost function (3.19) is equivalent to

$$J = \int_0^\infty \left[x_\beta(t)^T Q x_\beta(t) + \dot{u}_\beta(t)^T R \dot{u}_\beta(t)\right] dt \tag{3.22}$$

subject to

$$\dot{x}_\beta(t) = Ax_\beta(t) + B\dot{u}_\beta(t) \tag{3.23}$$

The solution to the cost function (3.22) is found from the following Riccati equation.

$$P(A + \beta I) + (A + \beta I)^T P - PBR^{-1}B^T P + Q = 0 \tag{3.24}$$

Assuming that the system matrix A is pre-stabilised as described in Section 3.3.1, A_α in (3.11) is substituted in the above to give

$$P(A - \alpha I) + (A - \alpha I)^T P - PBR^{-1}B^T P + Q + 2\alpha P + 2\beta P = 0 \tag{3.25}$$

with $Q_\beta = Q + 2\alpha P + 2\beta P$, it can be rewritten as

$$P(A - \alpha I) + (A - \alpha I)^T P - PBR^{-1}B^T P + Q_\beta = 0 \tag{3.26}$$

Using the above result, the cost function of (3.68) is altered in the following form to introduce the prescribed degree of stability β.

$$J = \int_0^{T_p} x_\alpha(t_i + \tau \mid t_i)^T Q_\beta x_\alpha(t_i + \tau \mid t_i) d\tau + \dot{u}^T R_L \dot{u} \tag{3.27}$$

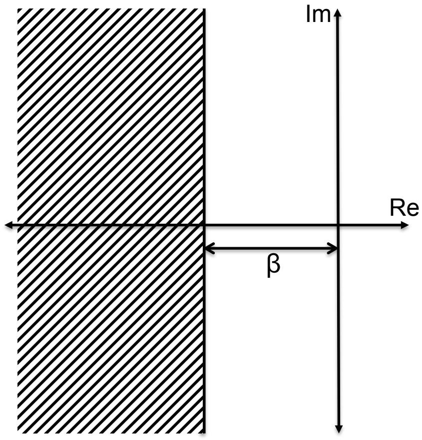

Figure 3.2: A region in the complex plane (shaded area) which meets the minimum decay rate of β.

where $Q_\beta = Q + 2\alpha P + 2\beta P$. The effect of β on the location of closed-loop eigenvalues is illustrated in Figure 3.2.

3.3.3 Robust prescribed degree of stability

A linearised model of VSC in (3.7 and 3.8) are sensitive to system uncertainties such as the steady-state duty-cycle, the load, or the parametric uncertainty of passive elements, which may change the model response considerably. For instance, we have so far assumed the input inductance to be constant and equal to the total inductance of the system (L_T) as

$$L_T = L + L_g \tag{3.28}$$

where L_g is the grid inductance and assumed to be negligible ($L_g \approx 0$). However it is expected that the grid impedance may change ($L_g \gg 0$), if the VSC is installed in under developed remote areas (e.g., rural areas) characterized by weak grid conditions due to low power transformers and long distribution wires [66]. The presented method extends the *Prescribed Degree of Stability* method to systematically find the Q matrix in (3.27) subject to parametric uncertainties of the model for a given a prescribed degree of stability of β

To facilitate the proposed approach, we will first establish the LMI formulation of the LQR optimal problem, as described in [35].

Consider the following linear system,

$$\dot{x}(t) = Ax(t) + Bu(t) \tag{3.29}$$

The optimal LQR controller for this system is obtained by using the state-feedback gain K ($u(t) = -Kx(t)$) that minimises the following cost function

$$J = \int_0^\infty (x(t)^T Qx(t) + u(t)^T Ru(t))dt \tag{3.30}$$

where Q is symmetric and semi-definite positive matrix and R is a symmetric and definite positive matrix. The closed-loop form of (3.30) is rewritten as

$$J = \int_0^\infty x(t)^T (Q - K^T RK)x(t)dt \tag{3.31}$$

In order to transform the above LQR problem into LMI formulation, we first apply the trace operator $\mathbf{Tr}(*)$ which satisfies $a^T Xb = \mathbf{Tr}(Xba^T)$ to (3.31), which yields

$$\begin{aligned} J &= \int_0^\infty \mathbf{Tr}((Q - K^T RK)xx^T)dt \\ &= \mathbf{Tr}((Q - K^T RK)P) \end{aligned} \tag{3.32}$$

where $P = \int_0^\infty x_0 x_0^T dt$ is a positive symmetric matrix that satisfies the stability condition with a prescribed degree of stability and x_0 is the initial condition. For the constraint on the matrix P, we can formulate as follows:

Let us first consider that the prescribed degree of stability, β (or the decay rate) is given such that

$$\lim_{t\to\infty} e^{\beta t}\|x(t)\| = 0 \tag{3.33}$$

Considering the quadratic Lyapunov's function

$$V(x(t)) = x(t)^T P x(t) \tag{3.34}$$

a quadratic stability with a prescribed degree of stability can be defined as (see [22])

$$\dot{V}(x(t)) \leq -2\beta V(x(t)) \tag{3.35}$$

From (3.34) and (3.29), considering the closed-loop system we can derive

$$\begin{aligned}\dot{V}(x(t)) &= \dot{x}(t)^T P x(t) + x(t)^T P \dot{x}(t) \\ &= x(t)^T (A - BK)^T P x(t) + x(t)^T P (A - BK) x(t)\end{aligned} \tag{3.36}$$

Applying the prescribed degree of stability condition in (3.35) to (3.36) and after some simplifications we can derive

$$(A - BK)P + P(A - BK)^T + 2\beta P < 0 \tag{3.37}$$

$$P > 0 \tag{3.38}$$

The LQR problem with a prescribed degree of stability can now be found by the following optimisation

$$\begin{aligned} &\underset{X}{\text{minimize}} \quad && \mathbf{Tr}(QP) + \mathbf{Tr}(R^{\frac{1}{2}} K P K^T R^{\frac{1}{2}}) \\ &\text{subject to} \quad && (A - BK)P + P(A - BK)^T + 2\beta P < 0 \end{aligned} \tag{3.39}$$

However, (3.39) is not linear due to the multiplication of P and K, so introducing a new variable $Y = KP$, (3.39) is rewritten as

$$\begin{aligned} \underset{X}{\text{minimize}} \quad & \mathbf{Tr}(QP) + \mathbf{Tr}(R^{\frac{1}{2}} Y P^{-1} Y^T R^{\frac{1}{2}}) \\ \text{subject to} \quad & AP + PA^T + BY + Y^T B^T + 2\beta P < 0 \end{aligned} \tag{3.40}$$

Furthermore, it was shown in [35] that the nonlinear term $\mathbf{Tr}(R^{\frac{1}{2}} Y P^{-1} Y^T R^{\frac{1}{2}})$ can be replaced by a second auxiliary X as

$$\begin{aligned} \underset{X}{\text{minimize}} \quad & \mathbf{Tr}(X) \\ \text{subject to} \quad & X > R^{\frac{1}{2}} Y P^{-1} Y^T R^{\frac{1}{2}} \end{aligned} \tag{3.41}$$

which can further be decomposed by Schur's complement as follows

$$X > R^{\frac{1}{2}} Y P^{-1} Y^T R^{\frac{1}{2}} \leftrightarrow \begin{bmatrix} X & R^{\frac{1}{2}} Y \\ Y^T R^{\frac{1}{2}} & P \end{bmatrix} > 0 \tag{3.42}$$

Combining (3.40) and (3.41), the complete LMI formualtion of the LQR problem is given as follows

$$\begin{aligned} \underset{X}{\text{minimize}} \quad & \mathbf{Tr}(QP) + \mathbf{Tr}(X) \\ \text{subject to} \quad & AP + PA^T + BY + Y^T B^T + 2\beta P < 0 \\ & \begin{bmatrix} X & R^{\frac{1}{2}} Y \\ Y^T R^{\frac{1}{2}} & P \end{bmatrix} > 0, P > 0 \end{aligned} \tag{3.43}$$

If there exist symmetric matrices $X \in \mathbb{R}^{n \times n}$ and $Y \in \mathbb{R}^{m \times n}$ such that the above condition is satisfied, then the state feedback gain is given by $K = YP^{-1}$ which is the optimal LQR controller. For the interest of *Prescribed Degree of Stability*, the Q matrix in (3.27) is set to $Q = P$.

The main advantage of this formulation is that the solution may include uncertainty in the model whereas the classical LQR control is only valid for systems without uncertainty. In order to handle parameter uncertainties, the uncertain model is re-expressed as a function of uncertain parameters, which in general can be expressed as follows

$$\dot{x}(t) = A(p)x(t) + B(p)u(t) \tag{3.44}$$

where the uncertain terms are grouped in a vector p. The vector p consists of N_p uncertain parameters $p = (p_1, ..., p_{N_p})$, where each uncertain parameter p_i is bounded between a minimum $(\underline{p})$ and a maximum value $(\bar{p})$ as follows

$$p_i \in [\underline{p_i} \quad \bar{p}_i] \tag{3.45}$$

Assuming that the matrix $[A(p), B(p)]$ depends linearly on p for all admissible values of p, the LMI-LQR formulation including decay rate constraints for uncertain system is formulated as follows

$$\begin{aligned} \underset{P,Y,X}{\text{minimize}} \quad & \mathbf{Tr}(QP) + \mathbf{Tr}(X) \\ \text{subject to} \quad & A_iP + PA_i^T + B_iY + Y^TB_i^T + 2\beta P \leq 0 \\ & \begin{bmatrix} X & R^{\frac{1}{2}}Y \\ Y^TR^{\frac{1}{2}} & P \end{bmatrix} > 0, P > 0 \\ & i = 1, \ldots, N_p \end{aligned} \tag{3.46}$$

If there exist symmetric matrices $X \in \mathbb{R}^{n \times n}$ and $Y \in \mathbb{R}^{m \times n}$ such that the above condition is satisfied, then the weighting matrix of Q in (3.27) is set to $Q = P$ which guarantees the prescribed degree of stability β under model parameter variations.

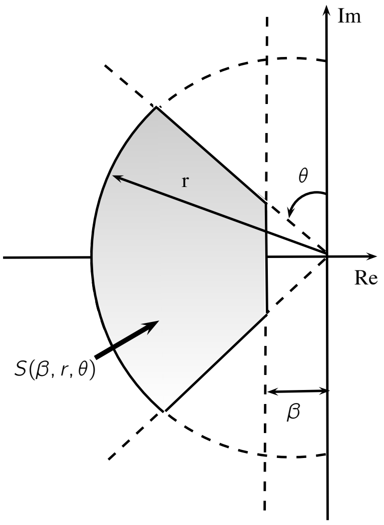

Figure 3.3: Region $S(\beta, r, \theta)$

3.4 Prescribed degree of stability and damping ratio

In this section, we extend the result in the preceding section to achieve both degree of stability and damping ratio by confining the eigenvalues in a prescribed region shown in Figure. 3.3. If we let complex poles be defined as $x + iy$, then it is easy to see that the complex poles of the system inside the $S(\beta, r, \theta)$ region in Figure. 3.3 satisfies

$$x < -\beta, \quad |x + iy| < r, \quad y < \cot(\theta)x \tag{3.47}$$

Furthermore, if we let $x + iy = \zeta\omega_n + i\omega_d$, the boundaries of $S(\beta, r, \theta)$ specifies a minimum decay rate β, a minimum damping ratio $\zeta > \sin\theta$, and a maximum damped natural frequency $\omega_d < r\cos\theta$, where $\omega_d = \omega_n\sqrt{1 - \zeta^2}$.

The $S(\beta, r, \theta)$ region in the complex plane can be defined using an LMI region which is defined as

$$D = \{z \in C : f_D(z) < 0\} \tag{3.48}$$

for fixed real matrices $L = L^T$ and a complex number z, where $f_D(z) = L + Mz + M^T\bar{z}$ is the characteristic function of D. So for any subset of the stable region in the complex plane (i.e. the left of the imaginary axis), it can be described using the LMI region. For instance, it can be shown that convex regions in the complex plane which are symmetric with respect to the real axis including half planes, horizontal strips, circles and sectors can be expressed as LMI regions. Furthermore, the intersection of a number of LMI regions is also a LMI region which allows to construct a more complicated regions as the intersection of a number of individual LMI regions. For example,

- half-plane $Re(z) < -\beta$: $f_D(z) = z + \bar{z} + 2\beta < 0$

- disk centered at $(-q, 0)$ with radius r:

$$f_D(z) = \begin{bmatrix} -r & q + z \\ q + \bar{z} & -r \end{bmatrix} < 0 \tag{3.49}$$

- conic sector with apex at the origin and inner angle 2θ:

$$f_D(z) = \begin{bmatrix} \sin\theta(z + \bar{z}) & \cos\theta(z - \bar{z}) \\ \cos\theta(\bar{z} - z) & \sin\theta(z + \bar{z}) \end{bmatrix} < 0 \tag{3.50}$$

Now, it is easy to see that if the closed-loop poles $(A - BK)$ are placed in the $S(\beta, r, \theta)$ region in the complex plane, the response of the closed-loop system will guarantee to have minimum damping ratio and decay rate. The seminal work by [27] showed that if there exist symmetric matrices $X \in \mathbb{R}^{n\times n}$ and $Y \in \mathbb{R}^{m\times n}$ such that

$$AX + XA^T + BY + Y^T B^T + 2\beta X < 0 \tag{3.51}$$

$$\begin{bmatrix} -rX & XA^T + Y^T B^T \\ AX + BY & -rX \end{bmatrix} < 0 \tag{3.52}$$

$$\begin{bmatrix} \cos\theta(AX + XA^T + BY + Y^T B^T) & \cos\theta(AX + XA^T + BY + Y^T B^T) \\ \sin\theta(-AX + XA^T + BY + Y^T B^T) & \sin\theta(AX + XA^T + BY + Y^T B^T) \end{bmatrix} < 0 \tag{3.53}$$

then, a state feedback gain (K) which guarantees the closed-loop poles lying in $S(\beta, r, \theta)$ is given by $K = YX^{-1}$. A detailed proof can be found in [27].

In order to retain the degree of stability and damping ratio as specified in the above LMI problem, using the closed-loop model $(A - BK)$ instead of the open-loop model of A in (3.7) is more desirable for the design of MPVC. To do that, the control signal leads to the following form

$$\dot{u}(t) = -Kx(t) \tag{3.54}$$

However, a serious drawback of the above control input is the lack of degree of freedom to handle the system constraints. Therefore, it is more appropriate to consider the control signal of the following form

$$\dot{u}(t) = -Kx(t) + \dot{v}(t) \tag{3.55}$$

where the auxiliary control signal v represents a degree of freedom which are no longer the predicted control moves, but perturbations on an unconstrained control law. The approach taken here is known as the closed-loop paradigm (CLP), where we give a brief overview and the application for MPVC in the following section.

3.4.1 Closed-Loop Paradigm

The basic idea of closed-loop paradigm (CLP), which was originally proposed as part of a stable generalised predictive control [14] is to choose a stabilising control law and to apply it throughout the predictions. As described in [97], one could take the view of CLP that the control law is hard-wired into the prediction computation which implies one has pseudo closed-loop predictions. Alternatively one could consider this as analogous to the control law used in mode 2 of dual mode MPC [76] with the only difference being that the terminal law is now also deployed during mode 1. Based on the stabilising control law, the CLP gives better numerical conditioning [98] of the optimisation and the stability and robustness analysis are more straightforward even for the constrained case [15]. Especially, the CLP can also be used to improve the robustness of MPC by choosing a control law that incorporates some design for robustness and using it as the terminal control law in the prediction. As such the perturbations used for constraint handling ($\dot{v}(t)$ in (3.55)) are acting on a robustified loop so one can achieve a constrained control law with better robustness than a conventional MPC.

Now, to apply the CLP to the design MPVC, we first consider substituting the closed-loop control signal (4.21) into the state dynamic equation, which leads to the closed-loop model prediction of the following form,

$$x_k(t_i + \tau \mid t_i) = e^{A_k \tau} x(t_i) + \int_0^{\tau} e^{A_k(\tau - \gamma)} B \dot{v}_k(\gamma) d\gamma \tag{3.56}$$

where $A_k = (A - BK)$. So the key idea of (3.55) and (3.56) is to embed the predictions of the unconstrained optimal behaviour and to find the global optimum with respect to the cost function in (3.57).

$$J = \int_0^{T_p} \left[x_k(t_i + \tau \mid t_i)^T Q x_k(t_i + \tau \mid t_i) + \dot{v}(\tau)^T R \dot{v}(\tau) \right] d\tau \tag{3.57}$$

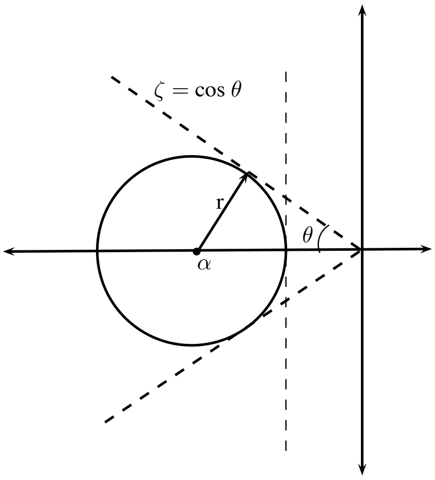

Figure 3.4: A circular region in the complex plane proposed by [36] to satisfy the prescribed degree of stability and damping ratio.

It is important to note that when the constraints are not violated the closed-loop response is dictated by the design of unconstrained optimal control law K, whereas for the case when the unconstrained optimal solutions are infeasible (i.e. violation of state and control input constraints) auxiliary control input $v(\tau)$ are allowed to perturb over a finite horizon T_p; which constitute the degrees of freedom (d.o.f.) within the optimisation. The design of K in (3.55) is therefore immensely important to ensure the stability and desired closed-loop response of MPC. Furthermore, since $(A-BK)$ is stable, (3.56) and (3.57) are numerically stable for a long prediction horizon.

3.4.2 Alternative regional pole placement

As an alternative to the LMI-based method in the previous section, another regional pole placement method proposed by [36] can also be used to place the closed-loop poles in a circular region defined by α and r as shown in Figure. 3.4. As shown, the placement of eigenvalues inside a prescribed region is defined by (α, r) where the specification is given in terms of damping ratio and alpha only. For different values of damping ratio, it is clear to see that poles are placed inside a region bounded by the minimum damping ratio. In their proposed method, a state feedback control $(u = -Kx)$ is found under the following condition in which eigenvalues of $(A - BK)$ lie within a disk of specified radius r at the center α if only if there is a $P > 0$ satisfying the equation.

$$\begin{aligned}-\alpha(A - BK)^* P - \alpha P(A - BK) + \\ (A - BK)^* P(A - BK) + (\alpha^2 - r^2)P = -Q\end{aligned}$$

where Q is positive definite, and the state feedback gain K is given by

$$K = -(r^2 R + B^T PB)^{-1} B^T P(A - \alpha I)x \tag{3.58}$$

P is the symmetric positive definite solution of the following discrete Riccati equation

$$\begin{aligned}P = \frac{(A - \alpha I)^T}{r} P \frac{(A - \alpha I)}{r} + H^T H - \frac{(A - \alpha I)^T}{r} \\ \cdot PB(r^2 R + B^T PB)^{-1} B^T P \frac{(A - \alpha I)}{r}\end{aligned} \tag{3.59}$$

Essentially the circular region defined above is the equivalent to the affine map of the unit disk at the origin.

3.5 Model Predictive Voltage Control

Assuming that the system matrix has been pre-stabilised as described in the previous section, the main part of MPVC design is presented in the following sections, where we focus on the continuous-time implementation of MPVC, using Laguerre function based technique described in [109]. A brief background to Laguerre functions and the application to the MPC design is presented in the Appendix B.

3.5.1 MPVC with Prescribed Degree of Stability

Following from (3.27), using the transformed state x_α and assuming that at the current time, say t_i, the state variable vector $x(t_i)$ is measured, the predicted state vector, denoted by $x_\alpha(t_i + \tau \mid t_i)$ at the future time τ, $\tau > 0$, is described by the following equation

$$x_\alpha(t_i + \tau \mid t_i) = e^{A_\alpha \tau} x(t_i) + \int_0^\tau e^{A_\alpha(\tau-\gamma)} B \dot{u}_\alpha(\gamma) d\gamma \tag{3.60}$$

where $\dot{u}_\alpha$ is the transformed derivative of the control signal. In VSC, the derivative of switching input signal $\dot{u}_\alpha(\tau)$ with two inputs is expressed as

$$\dot{u}_\alpha(\tau) = \begin{bmatrix} \dot{S}_d(\tau) & \dot{S}_q(\tau) \end{bmatrix}^T \tag{3.61}$$

and the input matrix B is partitioned as

$$B = \begin{bmatrix} B_1 & B_2 \end{bmatrix} \tag{3.62}$$

where B_1 and B_2 are the first and second columns of the B matrix. With this formulation, each input signal is described with a Laguerre function expansion (see Appendix B for detailed explanations). Namely, by choosing two continuous-time Laguerre function vectors $L_1(\tau)$ and $L_2(\tau)$ with dimensions N_1

and N_2, the derivative of the control signal $\dot{u}_\alpha(\tau)$ is represented by

$$\dot{u}_\alpha(\tau) = \begin{bmatrix} L_1^T(\tau) & 0_{L2}^T \\ 0_{L1}^T & L_2^T(\tau) \end{bmatrix} \begin{bmatrix} \eta_1 \\ \eta_2 \end{bmatrix} \tag{3.63}$$

where 0_{L1} and 0_{L2} are the zero column vectors with the same dimensions as $L_1(\tau)$ and $L_2(\tau)$. In addition, both $L_1(\tau)$ and $L_2(\tau)$ satisfy the differential equation as below, with their own scaling factors and number of terms (p and N parameters)

$$\dot{L}(\tau) = A_p L(\tau) \tag{3.64}$$

where

$$A_p = \begin{bmatrix} -p & 0 & \dots & 0 \\ -2p & -p & \dots & 0 \\ \vdots & \vdots & \ddots & 0 \\ -2p & \dots & -2p & -p \end{bmatrix}$$

and $L(0)$ is the $N \times 1$ vector with each element equal to $\sqrt{2p}$.

By substituting (3.63) into the state prediction equation, the predicted state vector, $x_\alpha(t_i + \tau \mid t_i)$ is rewritten as

$$x_\alpha(t_i + \tau \mid t_i) = e^{A_\alpha \tau} x(t_i) + \int_0^\tau e^{A_\alpha(\tau-\gamma)} \begin{bmatrix} B_1 L_1^T(\gamma) & B_2 L_2^T(\gamma) \end{bmatrix} d\gamma \begin{bmatrix} \eta_1 \\ \eta_2 \end{bmatrix} \tag{3.65}$$

To simplify the notation, let the convolution integral be denoted as

$$\phi(\tau)^T = \int_0^\tau e^{A_\alpha(\tau-\gamma)} \begin{bmatrix} B_1 L_1^T(\gamma) & B_2 L_2^T(\gamma) \end{bmatrix} d\gamma \tag{3.66}$$

where $\phi(\tau)^T$ can be easily computed by solving a set of linear algebraic equations (see Appendix B for the derivation). By defining the coefficient vector of Laguerre polynomials as $\eta^T = [\eta_1^T \ \eta_2^T]$, the prediction of future states is expressed as

$$x_\alpha(t_i+\tau \mid t_i) = e^{A_\alpha \tau} x(t_i) + \phi(\tau)^T \eta \tag{3.67}$$

Considering the cost function of below with a prescribed degree of stability.

$$J = \int_0^{T_p} x_\alpha(t_i+\tau \mid t_i)^T Q_\alpha x_\alpha(t_i+\tau \mid t_i) d\tau + \eta^T R_L \eta \tag{3.68}$$

where Q and R_L are symmetric positive definite and positive semi-definite matrices, written as $Q > 0$ and $R_L \geq 0$ respectively, by substituting the predicted state equation of (3.60) into the above cost function yields

$$J = \eta^T \Omega \eta + 2\eta^T \Psi x(t_i) + constant \tag{3.69}$$

where the quantities of Ω and Ψ are

$$\Omega = \{\int_0^{T_p} \phi(\tau) Q_\beta \phi(\tau)^T d\tau + R_L\}; \Psi = \int_0^{T_p} \phi(\tau) Q_\beta e^{A_\alpha \tau} d\tau$$

Considering the unconstrained minimization with respect to the parameter vector η of the cost function (3.69), the minimizing η is found from the following least squares solution

$$\eta = -\Omega^{-1} \Psi x(t_i) \tag{3.70}$$

By the principle of receding horizon control, the optimal control $\dot{u}(t)$ for the unconstrained problem at time t_i is

$$\dot{u}_\alpha(t_i) = \begin{bmatrix} L_1^T(0) & o_{L2}^T \\ o_{L1}^T & L_2^T(0) \end{bmatrix} \begin{bmatrix} \eta_1 \\ \eta_2 \end{bmatrix} \tag{3.71}$$

With the derivative of the control signal computed, the actual control signal is written as

$$u(t_i) = u(t_i - \Delta t) + \dot{u}_\alpha(t_i) \Delta t \tag{3.72}$$

where Δt is the sampling interval.

3.5.2 MPVC with Prescribed Degree of Stability and Damping Ratio

Since we are optimising the auxiliary control signal $\dot{v}(\tau)$ in a finite horizon, a state prediction based on the auxiliary control signal is given as

$$x_k(t_i + \tau \mid t_i) = e^{A_k \tau} x(t_i) + \int_0^{\tau} e^{A_k(\tau - \gamma)} \begin{bmatrix} B_1 L_1^T(\gamma) & B_2 L_2^T(\gamma) \end{bmatrix} d\gamma \begin{bmatrix} \eta_1 \\ \eta_2 \end{bmatrix} \tag{3.73}$$

where each auxiliary control signal $\dot{v}(\tau)$ is described with a Laguerre function expansion by choosing two continuous-time Laguerre function vectors $L_1(\tau)$ and $L_2(\tau)$ (see the previous section for the definition of $L_1(\tau)$ and $L_2(\tau)$). Similarly the cost function with auxiliary control signal $\dot{v}(\tau)$ is given below

$$J = \int_0^{T_p} \left[x_k(t_i + \tau \mid t_i)^T Q x_k(t_i + \tau \mid t_i) + \dot{v}(\tau)^T R \dot{v}(\tau) \right] d\tau \tag{3.74}$$

Substituting the predicted state variables and rearranging the terms in (3.74) yields the following equation which is quadratic in η

$$J = \eta^T \Omega \eta + 2\eta^T \Psi x(t_i) + constant \tag{3.75}$$

where the quantities of Ω and Ψ are

$$\Omega = \{ \int_0^{T_p} \phi(\tau) Q \phi(\tau)^T d\tau + R_L \}; \Psi = \int_0^{T_p} \phi(\tau) Q e^{A_k \tau} d\tau$$

The unconstrained minimization of the above cost function yields

$$\eta = -\Omega^{-1} \Psi x(t_i) \tag{3.76}$$

By the principle of receding horizon control, the optimal auxiliary control input $\dot{v}(t)$ for the unconstrained problem at time t_i is

$$\dot{v}_k(t_i) = \begin{bmatrix} L_1^T(0) & o_{L2}^T \\ o_{L1}^T & L_2^T(0) \end{bmatrix} \begin{bmatrix} \eta_1 \\ \eta_2 \end{bmatrix} \tag{3.77}$$

From (3.55), the derivative of the control signal $\dot{u}(t)$ is given by

$$\dot{u}(t) = (-K + K_{mpc})x(t) \tag{3.78}$$

where $K_{mpc} = -\Omega^{-1}\Psi$. Finally, the actual control signal $u(t)$ defined in () is given by

$$u(t_i) = u(t_i - \Delta t) + \dot{u}(t_i)\Delta t \tag{3.79}$$

where Δt is the sampling interval.

3.6 Constrained MPVC

In the grid-connected VSC, the amplitude of switching functions (i.e modulation index) must be restricted within a linear modulation region to avoid inducing any unwanted harmonics on the input currents, which leads to the following relationship in the synchronous reference frame [114].

$$S_d^2 + S_q^2 \leq \frac{4}{3} \tag{3.80}$$

The figure 3.5 shows this relationship graphically and a region of linear modulation is defined by the area inside a circle with a radius of $\frac{2}{\sqrt{3}}$.

Within a linear modulation region defined in (3.80), a stricter constraint region such as shown in Figure 3.6 can be defined by considering the maximum deviation of I_d currents from the nominal values (i.e a maximum load distur-

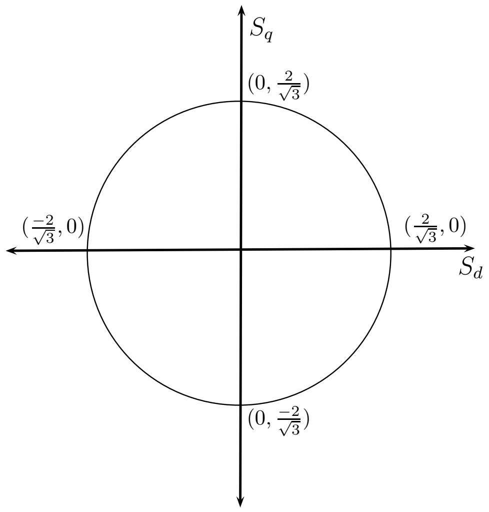

Figure 3.5: Switching function space of S_d and S_q: a linear modulation region is defined by the area inside the circle with a radius $\frac{2}{\sqrt{3}}$

bance). Recall that the steady-state d-q axis switching function is defined by the equation below,

$$S_{do} = \frac{2(e_d - RI_d)}{V_{dco}} \tag{3.81}$$

$$S_{qo} = -\frac{2\omega L I_d}{V_{dco}} \tag{3.82}$$

where I_d is the nominal active current for the chosen operating condition. If the saturation limit for I_d current is defined as

$$I_{d_{max}} = I_d + \Delta I_d \tag{3.83}$$

$$I_{d_{min}} = I_d - \Delta I_d \tag{3.84}$$

where ΔI_d is the amplitude of the maximum deviation from the nominal I_d current, and thus by substituting the above into (3.81) and (3.82). S_d^{max}, S_q^{max}, S_d^{min}

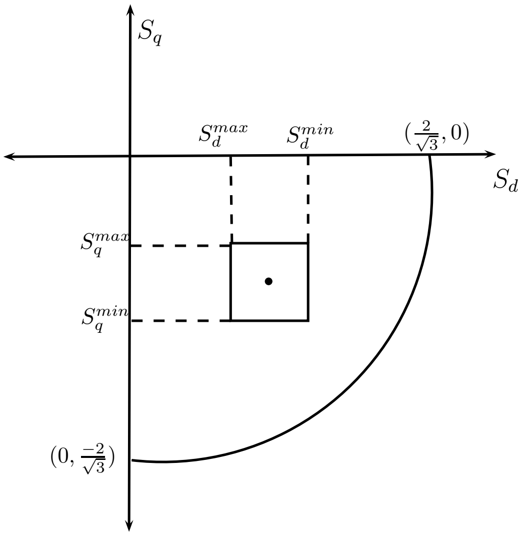

Figure 3.6: Redefined constraint region of S_d and S_q by considering the maximum deviation of I_d current from the nominal value in both rectification and regeneration mode: (•) indicates a steady-state switching inputs

and S_q^{min} are defined as.

$$S_d^{max} = \frac{2(E - R(I_d + \Delta I_d))}{V_{dco}} \tag{3.85}$$

$$S_q^{max} = -\frac{2\omega L(I_d + \Delta I_d)}{V_{dco}} \tag{3.86}$$

$$S_d^{min} = \frac{2(E - R(I_d - \Delta I_d))}{V_{dco}} \tag{3.87}$$

$$S_q^{min} = -\frac{2\omega L(I_d - \Delta I_d)}{V_{dco}} \tag{3.88}$$

Having formulated the constraints for switching inputs S_d and S_q, the next step is to translate them into linear inequalities, and relate them to the original model predictive control problem.

The key here is to parametrize the constrained variables using the same orthonormal basis functions as the ones used in the design of predictive control. Subsequently, we represent the constraints in terms of the parameter vector η. For the 'Prescribed Degree of Stability' approach, assuming that Δt is the sampling interval for implementation, the first sample of the control signal at the optimization window, is calculated as

$$u(t_i) = u(t_i - \Delta t) + \begin{bmatrix} L_1^T(0) & o_{L2}^T \\ o_{L1}^T & L_2^T(0) \end{bmatrix} \begin{bmatrix} \eta_1 \\ \eta_2 \end{bmatrix} \Delta t \tag{3.89}$$

This leads to the constraints for the control signal at the first sample time of the window for the lower limit as

$$u^{min} - u(t_i - \Delta t) \leq \begin{bmatrix} L_1^T(0) & o_{L2}^T \\ o_{L1}^T & L_2^T(0) \end{bmatrix} \begin{bmatrix} \eta_1 \\ \eta_2 \end{bmatrix} \Delta t \tag{3.90}$$

for the upper limit as

$$\begin{bmatrix} L_1^T(0) & o_{L2}^T \\ o_{L1}^T & L_2^T(0) \end{bmatrix} \begin{bmatrix} \eta_1 \\ \eta_2 \end{bmatrix} \Delta t \leq u^{max} - u(t_i - \Delta t) \tag{3.91}$$

Similarly, for the approach in section 3.4, the first sample of the control signal at the optimization window, is calculated as

$$u(t_i) = u(t_i - \Delta t) - Kx(t_i)\Delta t + \begin{bmatrix} L_1^T(0) & o_{L2}^T \\ o_{L1}^T & L_2^T(0) \end{bmatrix} \begin{bmatrix} \eta_1 \\ \eta_2 \end{bmatrix} \Delta t \tag{3.92}$$

This leads to the constraints for the control signal at the first sample time of the window for the lower limit as

$$u^{min} - u(t_i - \Delta t) + Kx(t_i)\Delta t \leq \begin{bmatrix} L_1^T(0) & o_{L2}^T \\ o_{L1}^T & L_2^T(0) \end{bmatrix} \begin{bmatrix} \eta_1 \\ \eta_2 \end{bmatrix} \Delta t \tag{3.93}$$

for the upper limit as

$$\begin{bmatrix} L_1^T(0) & o_{L2}^T \\ o_{L1}^T & L_2^T(0) \end{bmatrix} \begin{bmatrix} \eta_1 \\ \eta_2 \end{bmatrix} \Delta t \leq u^{max} - u(t_i - \Delta t) + Kx(t_i)\Delta t \tag{3.94}$$

More specifically, with the control vector defined by $u = [S_d \; S_q]^T$, the limits corresponding to the operation of the converter are $u^{min} = [S_d^{min} \; S_q^{min}]^T$ and $u^{max} = [S_d^{max} \; S_q^{max}]^T$.

With the operational constraints specified, the predictive control problem with hard constraints imposed in the design becomes the problem of finding the optimal solution of the quadratic cost function

$$J = \eta^T \Omega \eta + 2\eta^T \Psi x(t_i) \tag{3.95}$$

subject to constraints

$$\begin{bmatrix} S_d^{min} - S_d(t_i - \Delta t) \\ S_q^{min} - S_q(t_i - \Delta t) \end{bmatrix} \leq C\eta \leq \begin{bmatrix} S_d^{max} - S_d(t_i - \Delta t) \\ S_q^{max} - S_q(t_i - \Delta t) \end{bmatrix} \tag{3.96}$$

and for the constraints in (3.93) and (3.94)

$$\begin{bmatrix} S_d^{min} - S_d(t_i - \Delta t) + Kx(t_i)\Delta t \\ S_q^{min} - S_q(t_i - \Delta t) + Kx(t_i\Delta t) \end{bmatrix} \leq C\eta \leq \begin{bmatrix} S_d^{max} - S_d(t_i - \Delta t) + Kx(t_i)\Delta t \\ S_q^{max} - S_q(t_i - \Delta t) + Kx(t_i)\Delta t \end{bmatrix} \tag{3.97}$$

where

$$C = \begin{bmatrix} L_1^T(0) & o_{L2}^T \\ o_{L1}^T & L_2^T(0) \end{bmatrix} \begin{bmatrix} \eta_1 \\ \eta_2 \end{bmatrix} \Delta t \tag{3.98}$$

There are three categories of methods in solving the above equation which are primal methods, dual methods and the primal-dual methods. In this work, primal-dual method of Hildrethis Quadratic Programming algorithm is chosen to provide the numerical solution to the constrained optimal problem [109]

3.7 Experimental Results

The experimental validation of the proposed method in this section is carried out using the test bench that was developed by the author, where the detailed description of the test bench set up is given in Appendix A.

Table 3.1: System parameters of grid-connected VSC

Symbol	Parameter Name	Value	Unit
L_s	Input filter inductance	3.0	mH
R_s	Input filter ESR	0.2	Ω
C_{dc}	DC-link Capacitance	700	μF
R_{dc}	DC-link load resistance	20–40	Ω
V_g	Grid Voltage	30	V
F_g	Grid Frequency	50	Hz

3.7.1 Comparison study with and without prescribed degree of stability

To illustrate the efficacy of the prescribed degree of stability used in the design of MPVC, a comparison study is done between the case where the prescribed degree of stability $\beta = 0$ and the case where $\beta = 100$. With the value of $\beta = 100$, all closed-loop poles of the MPVC lie on the left of -100 line on the complex plane as shown in Figure 3.8. In the experimental results shown in Figure.3.7, a step load change of DC link resistance from $20\ \Omega$ to $40\ \Omega$ occurs at around 1 second, and the transient responses of the DC bus voltage are compared. It is seen from this figure that it took about 0.02 second for the DC bus voltage to return to the reference signal when $\beta = 100$, whilst when $\beta = 0$ it took at least

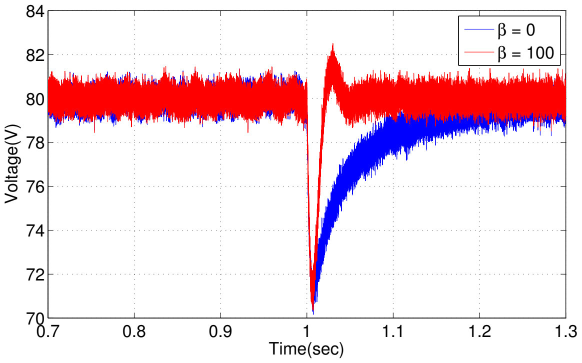

Figure 3.7: Comparison of DC bus voltage response to a step load change with $\beta = 0$ and $\beta = 100$.

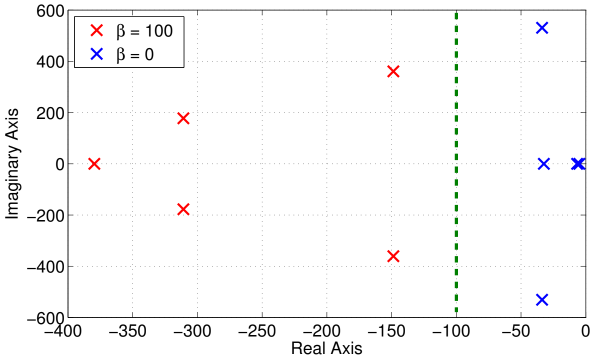

Figure 3.8: Comparison of closed-loop eigenvalue placement with $\beta = 0$ and $\beta = 100$.

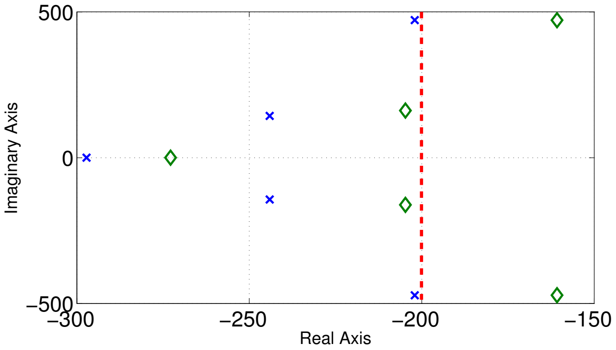

Figure 3.9: Plot of closed-loop pole placement with $\beta = 200$ for a system with the nominal input inductance $3mH$ (x) and the system with the input inductance variation $3.5mH$ ($\diamond$)

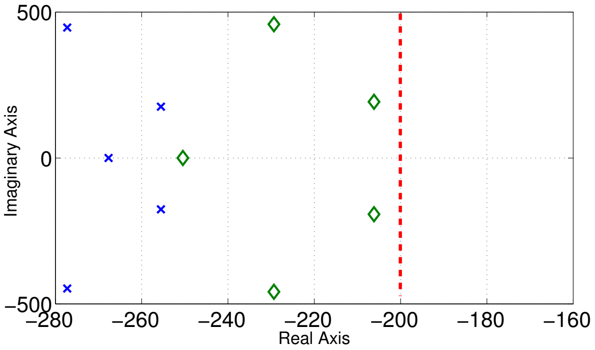

Figure 3.10: Plot of closed-loop pole placement with $\beta = 200$ for a system with the nominal input inductance $3mH$ (x) and the system with the input inductance variation $3.5mH$ ($\diamond$) based on Robust Prescribed Degree of Stability in section 3.3.

more than 0.2 seconds for DC bus voltage to get in the vicinity of the reference signal. The results clearly show that the transient response of DC bus voltage to a step load change is greatly improved for the case of $\beta = 100$. This result demonstrates that by tuning a scalar value of β, the desired transient closed-loop response of MPVC can now be achieved without extensively tuning the weighting matrices.

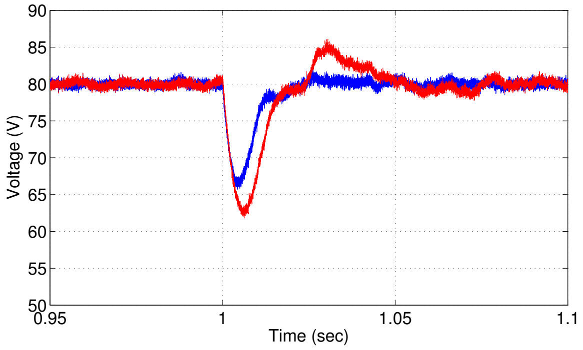

Figure 3.11: Comparison of DC bus voltage response to a step load change with $\beta = 200$ for PDS (red) and robust PDS (blue)

3.7.2 Robust prescribed degree of stability

In this section of the experimental validation, a variation of input inductance (e.g. change in the grid condition) is considered to analyse the effect on the closed-loop poles of MPVC with a prescribed degree of stability method.

To see how the inductance variation affects the prescribed degree of stability method, the matrix P in (3.26) is first obtained based on the nominal inductance value of 3 mH for $\beta = 200$.

$$P = \begin{bmatrix} 1.058e^{-5} & 1.230e^{-6} & 7.376e^{-5} & 3.505e^{-4} & 2.621e^{-3} \\ 1.230e^{-6} & 2.571e^{-5} & 1.266e^{-6} & 1.086e^{-3} & 2.237e^{-4} \\ 7.376e^{-5} & 1.266e^{-6} & 6.235e^{-6} & 6.634e^{-4} & 2.308e^{-5} \\ 3.505e^{-4} & 1.086e^{-3} & 6.634e^{-4} & 0.008 & 0.0015 \\ 2.621e^{-3} & 2.237e^{-4} & 2.308e^{-5} & 0.0015 & 0.0106 \end{bmatrix} \tag{3.99}$$

Based on (3.99) and the weighting matrix of Q_β in (3.27), the resulting closed-loop poles of MPVC are shown (indicated as x) in Figure 3.9, which indicates that the closed-loop poles of MPVC satisfy the stability requirement ($\beta = 200$).

Now if the same P matrix in (3.99) is applied to the system with a variation of 0.5 mH, the resulting closed-loop poles of MPVC (indicated as ($\diamond$)) in Figure 3.9

do not satisfy the stability requirement, which indicates that when there is a mismatch in the input inductance between the actual system and the model used to obtain the P matrix, the prescribed degree of stability requirement ($\beta = 200$) can not be guaranteed, and it will also lead to a slower closed-loop response speed than the desired minimum decay rate.

To overcome this issue, a robust prescribed degree of stability method in section 3.3 is applied considering the variation of inductance.

$$L_s = \{L_s - 0.5mH, \ \ L_s + 0.5mH\} \tag{3.100}$$

Based on above interval of input inductance, the LMI-LQR in (3.46) is solved and obtained the following P matrix

$$P = \begin{bmatrix} 0.0018 & -7.978e^{-6} & 0.0029 & 0.0771 & 0.8522 \\ -7.978e^{-6} & 5.315e^{-6} & 1.266e^{-6} & 0.0021 & -4.237e^{-4} \\ 0.0029 & 1.266e^{-6} & 0.0046 & 0.1240 & 1.3734 \\ 0.0771 & 0.0021 & 0.1240 & 406.1952 & 29.2509 \\ 0.8522 & -4.237e^{-4} & 1.3734 & 29.2509 & 837.5592 \end{bmatrix} \tag{3.101}$$

The resulting closed-loop poles of the system based on (3.101) is shown in Figure.3.10. Clearly, the closed-loop poles of both nominal and uncertain system now satisfies the minimum decay rate by lying left to the minimum prescribed degree of stability requirement ($\beta = 200$).

To further validate the robust prescribed degree of stability strategy, an experimental test is carried out to compare two strategies on the DC-bus voltage disturbance rejection. For the test, the input inductance is set to $3.5mH$ and the P matrix in (3.99) and (3.101) are used to obtain the unconstrained MPVC control laws for PDS and robust PDS strategies respectively. Figure 3.11 is the response of DC-bus voltage when the DC load was step changed from 40Ω to

20Ω. Comparing the two responses, it is clear that the response of PDS method is slower and has a larger overshoot than the robust PDS which aligns with the response expected from the closed-loop poles in Figure 3.9.

3.7.3 Experimental results for prescribed degree of stability and damping ratio

Table 3.2: System parameters of VSC and the main grid

Symbol	Parameter Name	Value	Unit
L_s	Input filter inductance	3	mH
R_s	Input filter ESR	0.2	Ω
C_{dc}	DC-link Capacitance	326	μF
R_L	DC-link load resistance	20–40	Ω
V_g	Grid Voltage	30	V
F_g	Grid Frequency	50	Hz

An experimental validation of the method proposed in section 3.4 is carried out based on the system parameters listed in Table 3.2. A noticeable difference compared to the Table 3.1 is the DC-link capacitance which has been reduced from $740\mu F$ to $326\mu F$. In practical applications, a reduction in DC-link capacitance is often desired since the required number of physical capacitors can significantly be reduced to decrease the hardware cost and the size of overall system.

However, a reduced DC-link capacitance makes the response of DC-link voltage and i_d and i_q current to become more oscillatory as can be seen from the plot of open-loop poles (indicated as ($\diamond$)) in Figure 3.12. If we apply the PDS method to pre-stabilise the system, the trace of closed-loop pole placement with increasing β value is also shown in the same figure (indicated as (X)), in which the under-damped poles are simply shifted horizontally. Hence it can be expected that the closed-loop response of the system will also exhibit under-damped response which may lead to an undesirable overshoot response in the voltage and current.

The above observation clearly shows the limitation of the design framework of MPVC with PDS that a desired damping ratio of closed-loop response can not be attained easily by just tuning the scalar parameter of β. For the same system, the method in section 3.4 is applied with a minimum damping ratio of 0.4 ($\theta = 25$) and decay-rate ($\beta = 200$) are chosen respectively. Solving the LMI in (3.51) using SeDuMi in YALMIP tool, yields a unconstrained control law K as,

$$K = \begin{bmatrix} 0.0475 & 0.0209 & 0.0692 & 0.0001 & 14.7629 \\ -0.0209 & 0.0133 & 0.0017 & 10.4158 & -0.0001 \end{bmatrix} \tag{3.102}$$

Figure 3.13 shows the resulting closed-loop poles of MPVC and comparing to the closed-loop poles in Figure 3.12, it is clear that CLP method provides an extra degree of freedom in the design such that, in the case of lightly damped system considered here, both the desired overshoot and the response speed can be satisfied simultaneously in the closed-loop response of MPVC.

Remark 3.7.1 *The weighting matrix R in the cost function in (3.57) can still be used to fine tune the system either on-line or off-line to obtain the desired closed-loop response.*

To experimentally validate the above observations, a step change in the voltage command is applied from 60V to 90V, and the response of V_{dc}, i_d and i_q currents are compared between MPVC with PDS and MPVC with CLP as shown in Figure 3.14,3.15 and 3.16 respectively. Generally, the response of CLP compared to PDS has a more damped response as we expected from the closed-loop pole placement in Figure 3.13. However, a difference in the response of i_q current in Figure 3.16 can be noted where a large oscillation

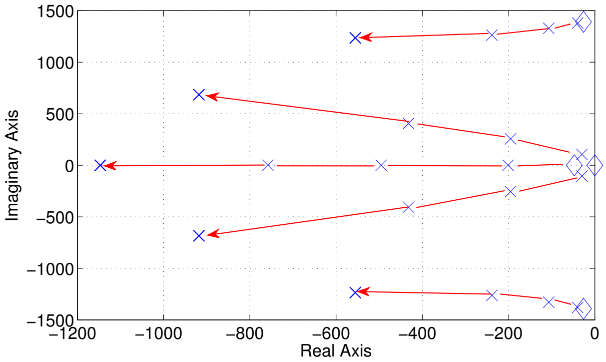

Figure 3.12: Plot of open-loop poles (◇) based on the VSC parameter in Table 3.2 and the trace of closed-loop poles (x) of MPVC with Prescribed Degree of Stability (PDS) method for increasing value of β.

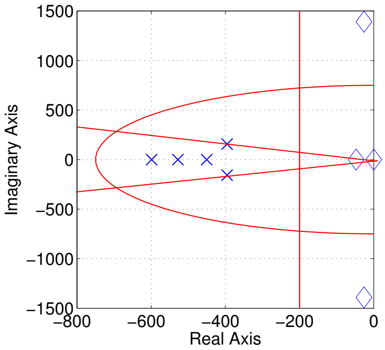

Figure 3.13: Plot of open-loop poles (◇) based on the VSC parameter in Table 3.2 and the closed-loop poles (x) of MPVC with Prescribed Degree of Stability and Damping (CLP) method for .

in i_q current with the maximum overshoot around -19A is shown for the PDS. A significance of this difference is highlighted in Figure 3.17 and 3.18, where the response of a phase current and voltage are shown. It can be seen that when the step change occurs at 1 sec, for 0.03 sec the phase current is not synchronised with the phase voltage (i.e. loss of unity-power factor) due to the oscillation observed in i_q current in Figure 3.16, where as shown in Figure 3.18 for CLP method, the unity power factor between the phase voltage and current

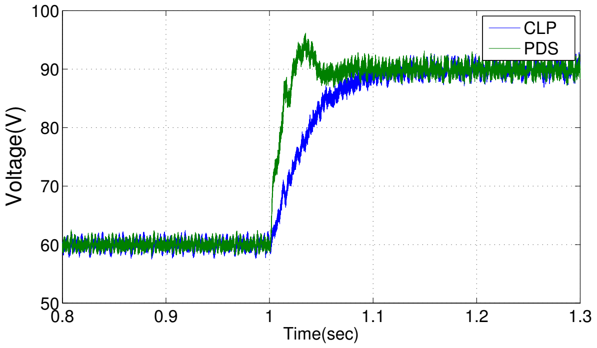

Figure 3.14: Comparison of DC-link voltage response to a step change in the reference input: MPVC with PDSD (gree) and MPVC with PDS (blue)

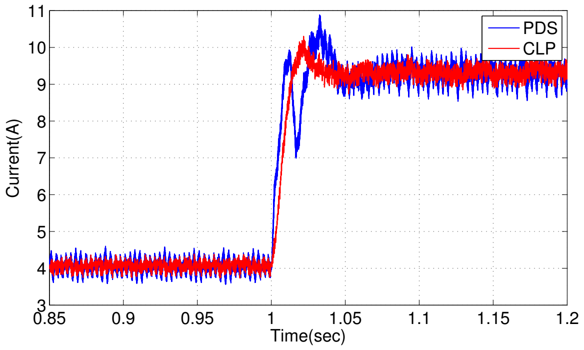

Figure 3.15: Comparison of i_d current response to a step change in the reference input: MPVC with PDSD (gree) and MPVC with PDS (blue)

is maintained.

3.7.4 Experimental results for rectification mode

Having validated the proposed pre-stabilisation techniques in MPVC, the following two sections presents experimental results for the rectification and the regeneration mode.

Starting with the rectification mode, the control objective of this mode is to keep the DC bus voltage at 80V, and i_q current at zero for unity power factor. In the experimental testing, prior to the rectification mode, the converter is operat-

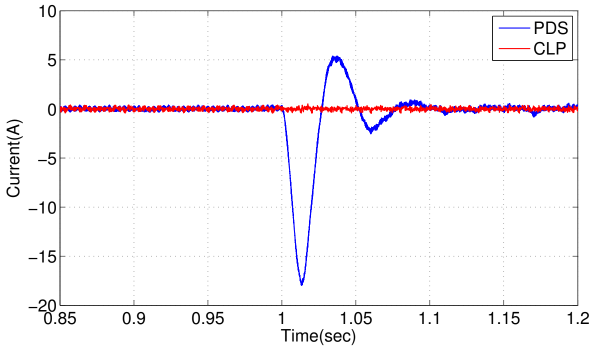

Figure 3.16: Comparison of i_q current response to a step change in the reference input: MPVC with PDSD (gree) and MPVC with PDS (blue)

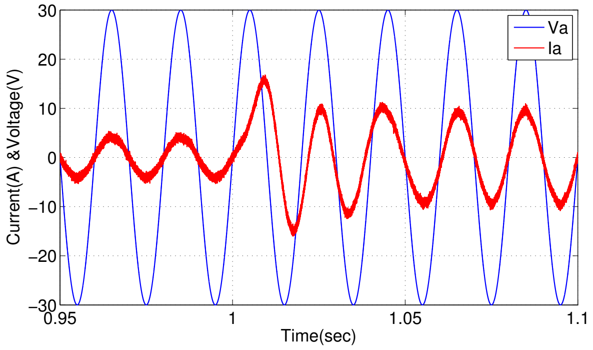

Figure 3.17: Response of a phase current (I_a) and the grid voltage based on MPVC with PDS (blue)

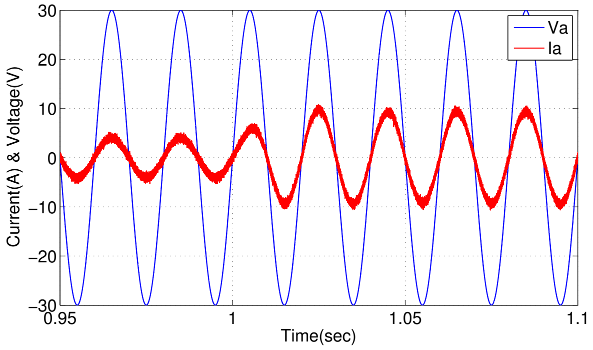

Figure 3.18: Response of a phase current (I_a) and the grid voltage based on MPVC with PDSD (blue)

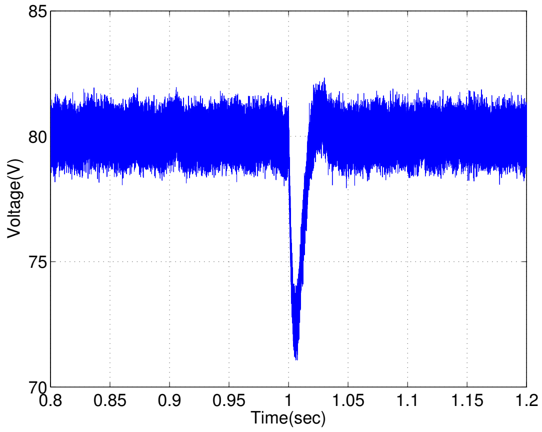

Figure 3.19: DC bus voltage response to a step input in rectification mode.

ing as a diode rectifier where the switching functions of IGBT are disabled and the current is only conducting through the freewheeling diode of IGBT. This is a necessary step for any VSC to naturally charge the DC-bus voltage.

When the rectification mode is switched on, the predictive controller is activated to boost the DC bus voltage from 35 V to 80 V. After the DC-bus voltage has been stabilised a step disturbance is injected by changing the load resistance from 40Ω to 20Ω. Figure 3.19–3.21 shows the closed-loop responses of the outputs $V_{dc}(t)$ and $i_q(t)$, as well as the state variable $i_d(t)$. Figure 3.21 shows that while drawing an extra current from the grid, i_q is well maintained around zero which results in zero phase shift between phase voltage and phase current (i.e unity power factor) and i_d is increased to a new steady-state value according to the required DC bus voltage level. Figure 3.23 shows the corresponding switching control inputs of S_d and S_q which are inside a linear modulation region.

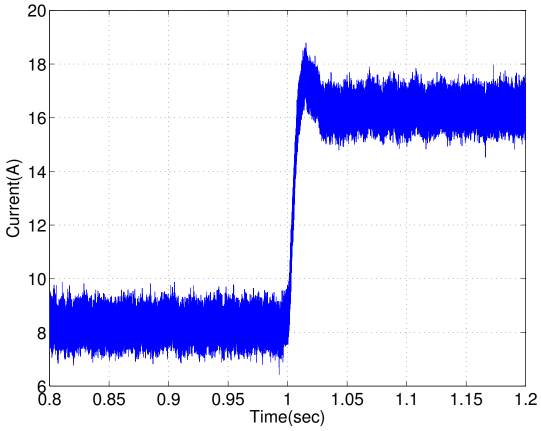

Figure 3.20: A step I_d current response in the rectification mode: a step load disturbance is injected at 1 sec by changing the load resistance from 40Ω to 20Ω

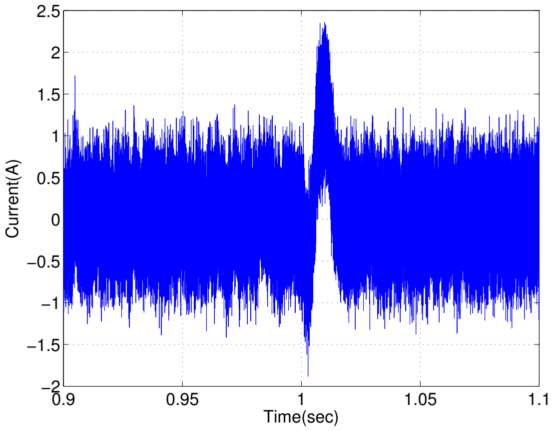

Figure 3.21: I_q current response in the rectification mode: a step load disturbance is injected at 1 sec by changing the load resistance from 40Ω to 20Ω

3.7.5 Experimental results for regeneration mode

The control objective of regeneration mode is the same as before, which is to keep the DC bus voltage at 80 V, and i_q current at zero for unity power factor. Prior to the regeneration mode, the converter is operating in rectification mode. At around $1sec$, an extra current is injected in the DC bus, which resulted in initial overshoot of DC bus voltage and the MPVC regulates the DC bus voltage around $80V$ as shown in Figure 3.24. Figure 3.25 and 3.25 show the closed-

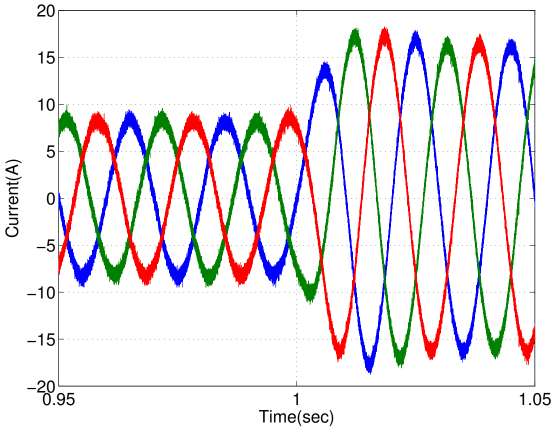

Figure 3.22: Three-phase current in rectification mode

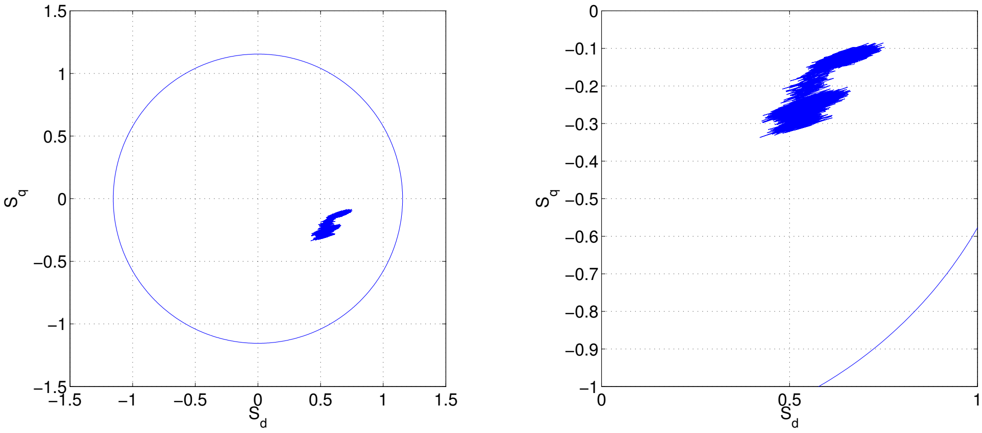

(a) (b)

Figure 3.23: Response of S_d and S_q in rectification mode: (a) response of S_d and S_q with respect to the circle representing the maximum linear modulation region in (3.80) and (b) zoomed-in view of S_d and S_q

loop responses of i_d and i_q in regeneration mode. It is seen that the steady-state value of i_d is negative which indicates that the current flow is reversed compared to the rectification mode. In this case the extra current injected into DC bus is converted to AC currents which feeds back into the main grid. For unity power factor operation, i_q is still maintained around zero. Figure 3.28 shows the corresponding switching control inputs of S_d and S_q.

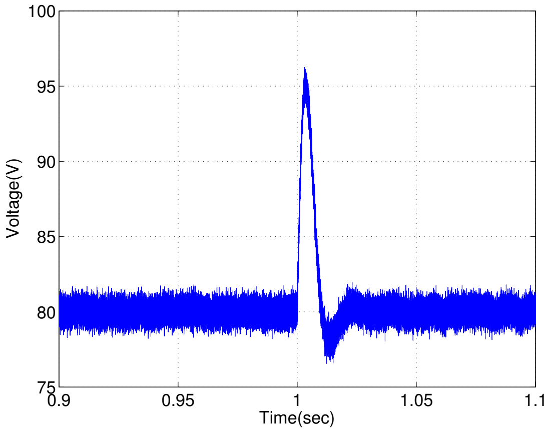

Figure 3.24: DC bus voltage response when a step disturbance input is injected to activate the regeneration mode.

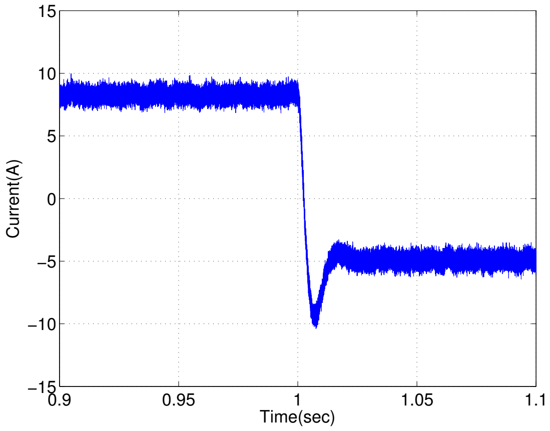

Figure 3.25: Response of I_d current: a mode change occurs at 1 sec from rectification mode to regeneration mode

3.7.6 Constrained Control

In this set of experimental results, the DC voltage is also maintained at $80V$ in the presence of operational constraints while load and mode changes occur. In the rectification mode, the load variations are generated using the variation of resistance in the DC load, while in the regeneration mode, an extra current is injected in the DC bus at the time interval $4 \leq t \leq 5$. The constraints are specified as $0.48 \leq S_d \leq 0.88$ and $-0.29 \leq S_q \leq 0.2$. Figure 3.29 shows

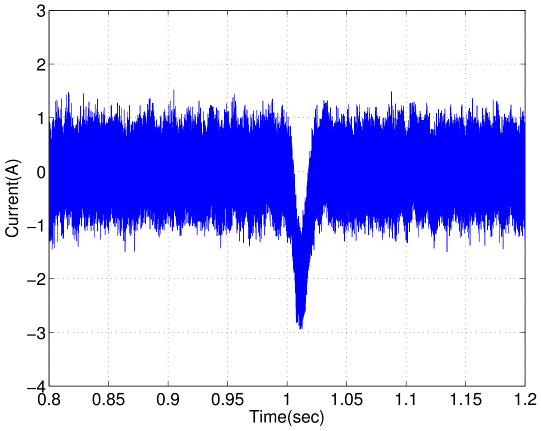

Figure 3.26: Response of I_q current: a mode change occurs at 1 sec from rectification mode to regeneration mode

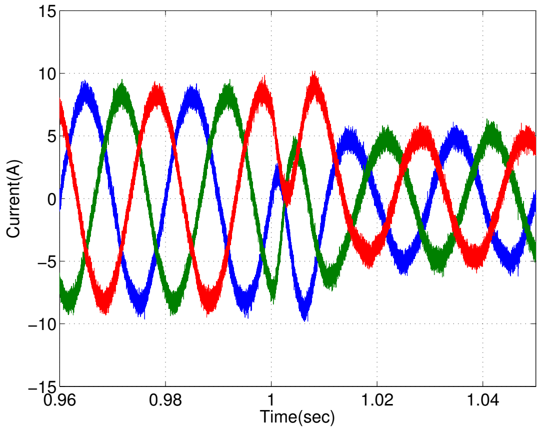

Figure 3.27: Response of three phase current: at 1 sec the mode is changed from rectification mode to regeneration mode

the responses of S_d and S_q with respect to the constraints whilst Figure 3.30 illustrates the variation of S_q with respect to S_d. It is seen that all constraints are satisfied. With the constraints on the amplitudes of the control signals, Figure 3.31 shows the responses of i_d and i_q currents. At the time interval $2 \leq t \leq 3$ second, because the required steady-state values for S_d and S_q to achieve unity power factor operation are beyond the specified lower limits, there is a steady-state error for the i_q current, showing that the q-axis current

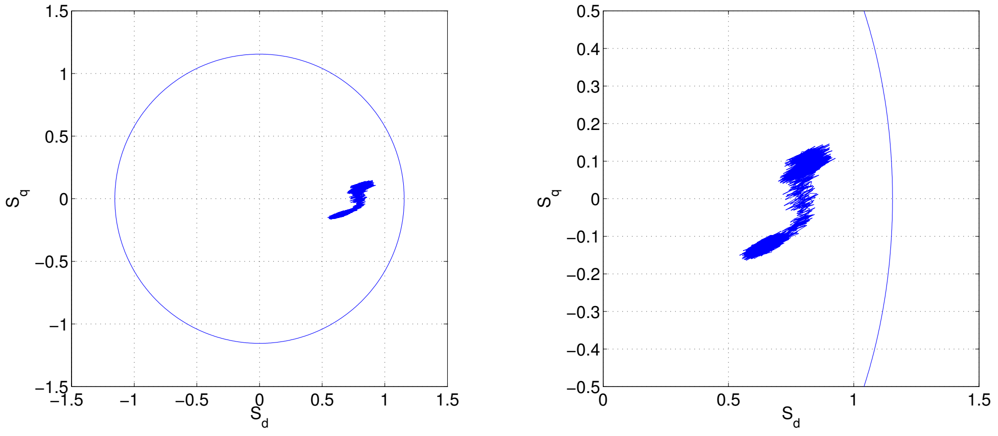

(a) (b)

Figure 3.28: Response of S_d and S_q in regeneration mode: (a) response of S_d and S_q with respect to the circle representing the maximum linear modulation region in (3.80) and (b) zoomed-in view of S_d and S_q

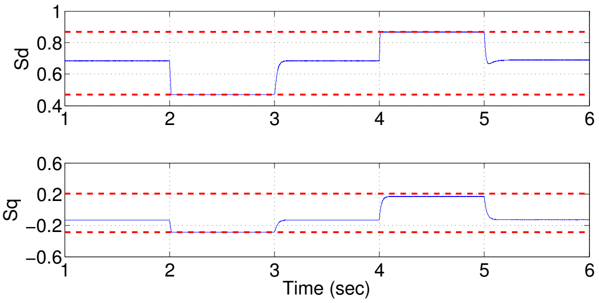

Figure 3.29: Plot of constrained control inputs of S_d and S_q. Amplitude limits of S_d and S_q (dashed-line); S_d and S_q (solid line).

no longer operates at zero in the steady-state. Similarly, in the regeneration mode ($4 \leq t \leq 5$), the required steady-state value for S_d and S_q to achieve unity power factor operation is beyond the specified upper limit, as a result, the q-axis current is not at zero in the steady-state. These conclusions are drawn from the observations of the plots of S_d and S_q, where the constraints are active in the steady-state operations of these two intervals.

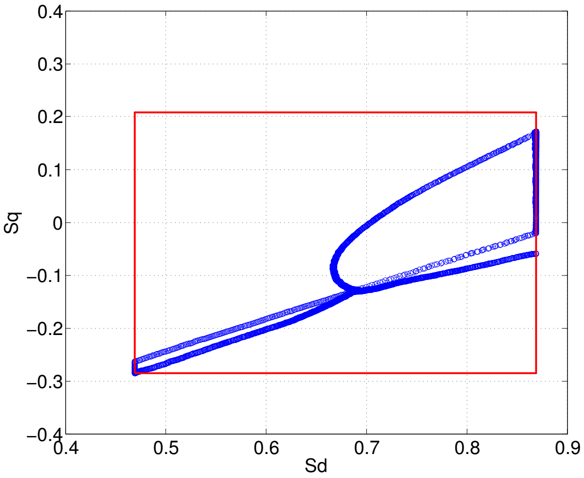

Figure 3.30: Variation of control inputs S_d and S_q: The rectangular box represents the control input constraints formed by (3.85).

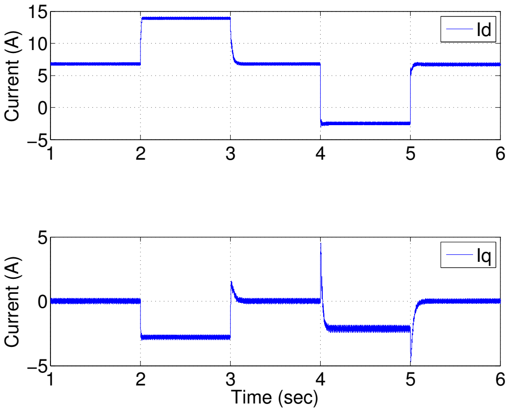

Figure 3.31: Responses of i_d and i_q in constrained control: a step load change of R_{dc} from 40Ω to 20Ω. A regenerative power source is injected between 4 and 5 sec

3.8 Conclusions

This chapter has investigated the design and implementation of a continuous-time model predictive control system for a grid-connected VSC. In particular, a centralised control of DC-bus voltage and the grid currents is presented with a pre-stabilisation technique known as a prescribed degree of stability as well damping ratio in the algorithm to provide an effective tuning parameter for the desired closed-loop performance. In comparison to the traditional cascaded PI control structure, the presented method offers not only the simplified control structure, but also the robustly stabilising controller that ensures the desired closed-loop performance under parametric uncertainties. To avoid the over-modulation of switching inputs, hard constraints based on the maximum linear modulation region have been formulated and implemented in the synchronous reference frame.

Chapter 4

Model Predictive Current Control with LCL filter

4.1 Introduction

The harmonics generated by the switching of the VSC are the main factor for causing grid voltage distortions which adversely affects the near-by sensitive equipment and the connected loads [42]. As the power ratings of the VSC increases, especially for applications above several kilowatts, harmonics distortion becomes an important consideration in the systems design phase [69]. For the VSC considered so far in this work, the input inductance (L filter) of the VSC have been used to reduce these harmonics. However, as the power rating of the VSC increases, a higher value of inductances are required as the switching frequency is reduced to minimise the switching losses. So realizing practical input filters becomes difficult due to the price rises and the poor dynamic responses.

These problems can be alleviated by using an LCL filter which has a better filtering characteristics even with comparatively smaller size of passive components than L filter [77]. This makes an LCL well suited for high-power conversion systems and have already been widely employed in wind farms of over hundreds of kilowatts [47],[67]. Typically, an LCL filter is connected to a grid-connected three phase VSC as shown in Figure 4.1, which is made up of three reactors with resistance and inductance on the converter side, three reactors

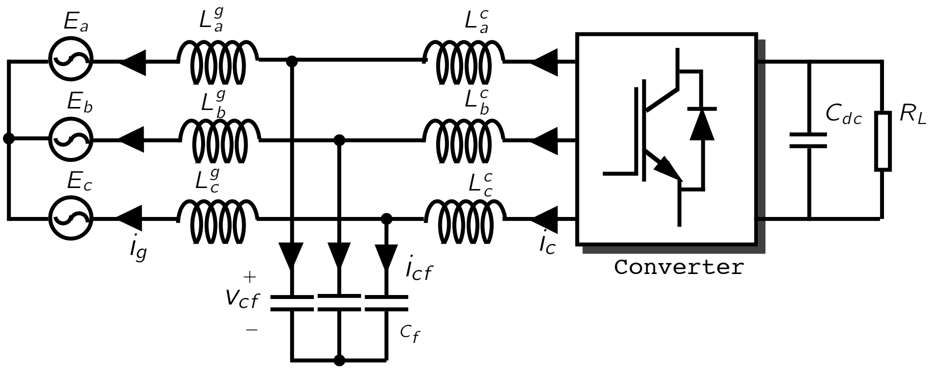

Figure 4.1: Three-phase voltage source converter with an LCL filter: The subscript g indicates the grid-side and c denotes the converter side for each components and measurements.

with resistance and inductance on the grid side, and three capacitors (each of them damped with a resistor).

In this chapter, we begin with analysing the frequency characteristics of the LCL filter in Section 4.2. The analysis identifies the resonant frequency of the LCL filter which must be sufficiently damped to avoid inducing excessive harmonics on the grid current. Following from the analysis, the MPC based current control method is presented in section 4.3 based on the reduced-order model of LCL filter which adopts the disturbance rejection controller to reduce the effect of resonance of LCL filter.

4.2 Frequency Characteristics of the LCL Filter

Assuming all filter losses are negligible (e.g. iron losses), LCL filter can be simplified to a per-phase equivalent circuit shown in Figure 4.2, and considering

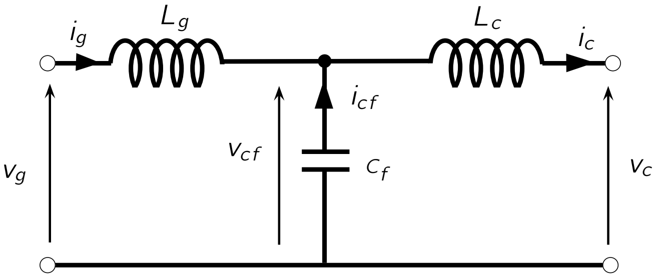

Figure 4.2: Single-phase equivalent circuit of LCL filter neglecting filter losses

$z_{L_gC}^2 = \frac{1}{L_gC_f}$ and $\omega_{res}^2 = \frac{L_T z_{L_gC}^2}{L_c}$ $(L_T = L_g + L_c)$ the transfer function of the LCL filter is given as follows [96],[41]

$$G(s) = \frac{i(s)}{v(s)} = \frac{1}{L_s}\frac{(s^2 + z_{LC}^2)}{(s^2 + \omega_{res}^2)} \tag{4.1}$$

where L_c is the converter-side inductor, L_T is the sum of grid-side and transformer inductance, C_f is parallel capacitor of LCL filter. Based on the transfer function in (4.1), the amplitude frequency characteristics of the LCL filter is calculated and compared to the L-filter as shown in Figure 4.3. It can be seen that the LCL filter has a better filtering characteristics in a higher frequency region, where the most of PWM switching harmonics appears. Furthermore, based on the parameters of both filters in Table 4.2, the total inductances in both filters are same, which indicates that even smaller source inductance in LCL filter

Table 4.1: System parameters of grid-connected VSC with an LCL filter

Symbol	Parameter Name	Value	Unit
L_c	Input filter inductance (converter side)	2.0	mH
L_g	Input filter inductance (grid side)	0.75	mH
C_f	Filter Capacitance	16.1	μF

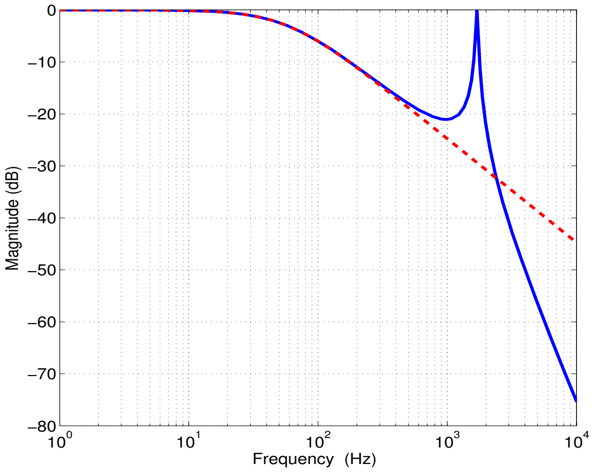

Figure 4.3: Comparison of amplitude frequency characteristics between L filter (dotted) and LCL filter: Based on the filter parameters given in Table 4.2, the resonant peak of the LCL filter is shown at 1694 Hz

can be used to achieve the similar filtering characteristic which potentially can reduce the overall cost significantly. However, since LCL filter is essentially a high order filter which has a resonant peak at the frequency given by [44],

$$f_r = \frac{1}{2\pi}\sqrt{\frac{L_g + L_c}{C_f L_g L_c}} \tag{4.2}$$

Hence, despite the aforementioned advantages, stabilising the system incorporating the LCL filter becomes a challenging problem, especially when the resonance peak of the LCL filter is excited by a feedback controller or an external load which in both cases result in excessive input current ripples or even possibly a closed-loop instability.

For a closer illustration of the associated stability problem with LCL filter, Figure. 4.4 shows the closed-loop response of three phase I_{abc} current of a current controller without proper damping of the LCL filter resonance. It can be seen that excessive ripples are present in the input currents, and the frequency

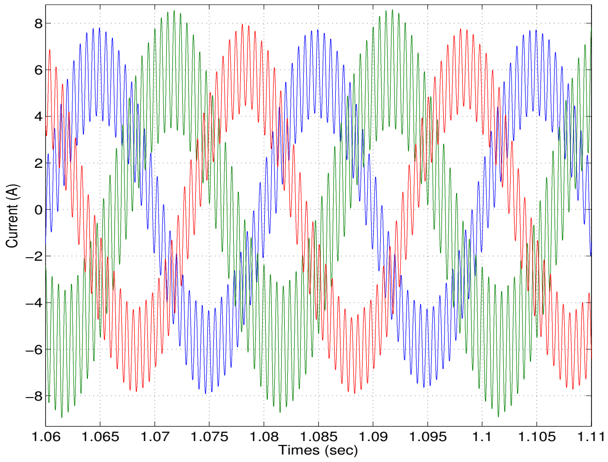

Figure 4.4: Simulation result of three phase current I_{abc} with undamped LCL filter resonance

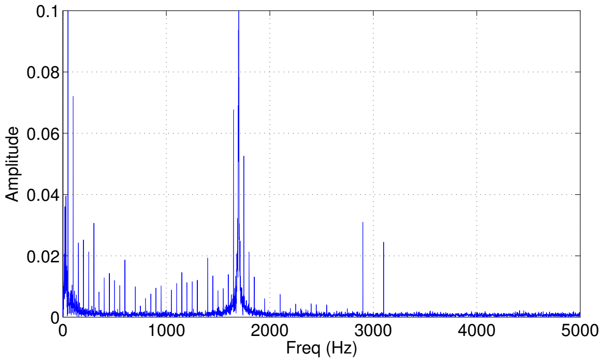

Figure 4.5: Frequency spectrum of a phase current with undamped LCL filter resonance: LCL filter resonant harmonic is shown as 1694 Hz

spectrum of the input current shown in Figure. 4.5 confirms that frequency of the ripple input current aligns with the resonance frequency of the LCL filter.

4.2.1 Damping methods of LCL filter

Various approaches have been suggested in the literature to damp the amplification of current and voltages at the resonant frequency of LCL filter. The most straightforward approach is the passive damping method. This method intro-

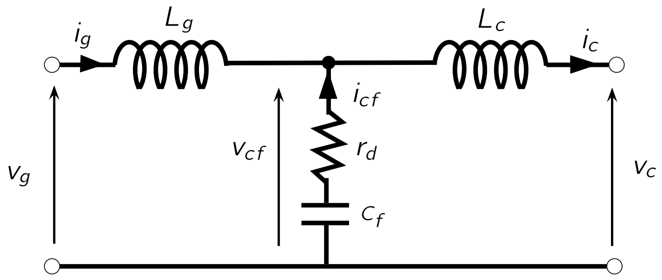

Figure 4.6: Single-phase equivalent circuit of LCL filter with a passive damping resistor (r_d)

duces a damping resistor in the LCL filter circuit as shown in Figure 4.6 where the transfer function is given as follows.

$$G(s) = \frac{i(s)}{v(s)} = \frac{1}{Ls}\frac{(s^2 + R_d C_f z_{LC}^2 s + z_{LC}^2)}{s^2 + s^2 + R_d C_f \omega_{res}^2 + \omega_{res}^2} \tag{4.3}$$

Comparing the frequency characteristics between damped and undamped LCL filter as shown in Figure 4.7, the resonant peak is substantially reduced in the case of passive damping circuit. However, by introducing the damping resistor in the circuit, the overall effectiveness of the LCL filter is reduced as it incurs more power losses which also compromises its attenuation factor at higher frequencies, hence neutralizing those benefits originally introduced by the undamped LCL filters [111]. An analytical design approach for passively damping LCL-filters was discussed in [77], however, due to the physical losses the passive damping approach is often limited to a specific application [60].

An alternative approach is the active damping approach. Generally, this is a

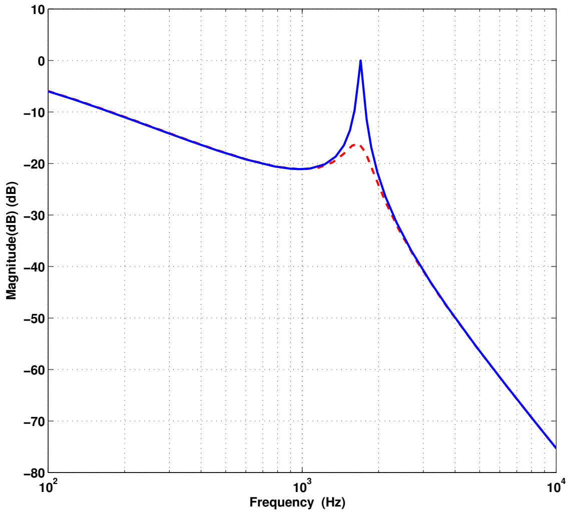

Figure 4.7: Comparison of frequency characteristics between passively damped LCL filter ($r_d = 1.5\Omega$) and undamped LCL filter (solid line)

software-based approach that requires no physical components to suppress the resonance of LCL filter, therefore it does not incur any physical power losses [77],[44],[45],[96],[105]. However the most of these methods relies on the feedback of the other control variables such as capacitor voltages or currents to the current control loop, which forms as an extra damping term to suppress the resonance of the LCL filter. Therefore, the realisation of this scheme often requires a more circuitry and sensors, in turn it may increases the circuit complexity and the cost. A comprehensive review on various active damping approaches for LCL filters and their resonance damping performances can be found in [77].

In the following section, a model predictive current control method is presented based on the reduced-order model of the LCL filter to control a three phase VSC with an LCL filter. In order to compensate the instability caused by the inherent undamped mode of the LCL filter, the disturbance rejection control term is used to suppress a high frequency disturbance.

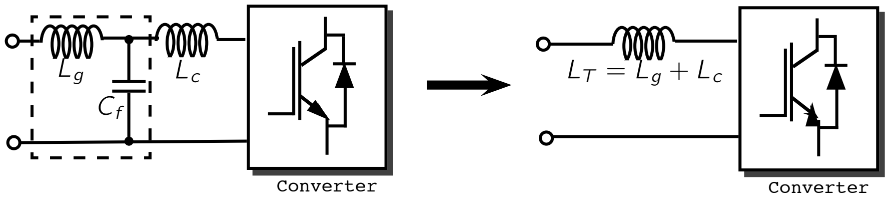

Figure 4.8: Approximation of LCL filter to L filter equivalent

4.3 MPCC with Finite-frequency H_∞ control

The previously mentioned stability problem associated with the LCL filter (see Figure 4.4 and 4.5) is largely due to the simplification in the control design that ignores the undamped mode of LCL filter (i.e.reduced-order model design). The underlying problem of such simplification is the closed-loop interaction between the current controller and the undamped dynamics of LCL filter [77],[19],[63]. In order to overcome this instability caused by the resonant dynamics of LCL filter, this section presents a model predictive current control strategy based on a reduced-order model of the LCL filter with a model-based disturbance rejection controller.

Firstly, the reduced order model LCL filter used in the proposed control design is obtained by approximating the LC part of the filter as shown in Figure 4.8. The approximation is valid because the LC part of the LCL filter aims to primarily reduce the high-frequency current harmonics [20]. Based on this assumption, the reduced-order model of LCL filter is obtained as below

$$\dot{x}_m(t) = A_m x_m(t) + B_m u(t) \tag{4.4}$$

$$y(t) = C_m x_m(t) \tag{4.5}$$

where A_m, B_m, C_m and X_m are given as

$$A_m = \begin{bmatrix} -\frac{R_T}{L_T} & \omega \\ -\omega & -\frac{R_T}{L_T} \end{bmatrix}, B_m = \begin{bmatrix} \frac{-v_{dco}}{2L_T} & 0 \\ 0 & \frac{-v_{dco}}{2L_T} \end{bmatrix}, \tag{4.6}$$

$$C_m = \begin{bmatrix} 1 & 0 \\ 0 & 1 \end{bmatrix}, x_m = \begin{bmatrix} i_d \\ i_q \end{bmatrix}, u = \begin{bmatrix} S_d \\ S_q \end{bmatrix} \tag{4.7}$$

where $L_T = L_c + L_g$ and $R_T = R_c + R_g$ are the value of total inductance and ESR in the LCL filter respectively. Note that the order of the model in (4.4) is kept same as the L-fiter system.

However, because the reduced-order model in (4.4) neglects the resonant part of LCL filter, the performance of the current tracking will be affected as we observed in Figure 4.4–4.5. To overcome this problem, a novel current control scheme which mitigates this resonance problem with the reduced-order model is presented in the following section.

4.3.1 Control Overview

The control scheme proposed in this section is shown in Figure 4.9, where the main current controller comprises of disturbance rejection control and nominal predictive control parts. The predictive control part is calculated on-line and steers the nominal system states to the desired set-point of i_d and i_q currents subject to hard constraints. The control design for this part follows the same process as in previous sections, which optimises the derivative of the control input, $\dot{u}(t)$, with respect to the following cost function in a receding horizon manner,

$$J = \int_0^{T_p} x(t_i + \tau \mid t_i)^T Q x(t_i + \tau \mid t_i) d\tau + \dot{u}^T R \dot{u} \tag{4.8}$$

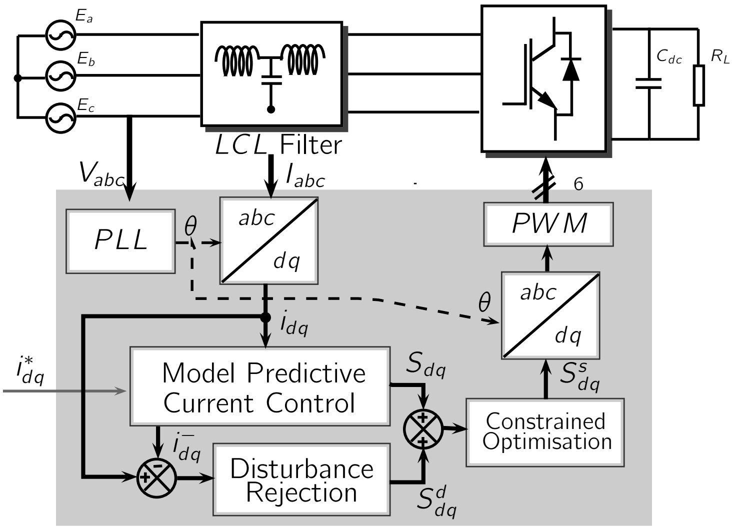

Figure 4.9: Overview of the MPCC with disturbance rejection controller for Grid-Connected VSC with an LCL filter: i^*_{dq} and i^-_{dq} indicates the reference current inputs and the nominal trajectory of i_{dq} respectively. The S_{dq} and S^d_{dq} corresponds to the nominal predictive and disturbance rejection control inputs respectively and S^s_{dq} is the constrained control input.

The actual control input applied to system is then obtained as follows

$$u(t) = u(t - \Delta t) + \dot{u}(t)\Delta t \tag{4.9}$$

where Δt is the sampling time of the discrete implementation.

The design for the nominal control input considers a disturbance free case, however because the model of LCL filter has been simplified, the influence of LCL filter resonance can be viewed as a disturbance $w(t)$ acting on the reduced-order system (4.4), which can be described as,

$$\dot{x}(t) = Ax(t) + Bu(t) + w(t) \tag{4.10}$$

The influence of state disturbance $w(t)$ on the actual system implies that if the control (4.9) computed from the conventional optimal control problem is applied to the uncertain system, it is not possible to establish robust exponential stability of the system (4.10).

To illustrate this effect in an intuitive manner, let us consider $x_e(t_i) = x(t_i) - \bar{x}(t_i)$ to be the error between the actual system state and nominal state at timestep t_i respectively, and the corresponding nominal model of the following form

$$\dot{\bar{x}}(t) = A\bar{x}(t) + Bu(t) \tag{4.11}$$

The actual system and the closed-loop state prediction at time step t_i are given as follows

$$x(t_i + \tau \mid t_i) = e^{A\tau}x_0(t_i) + \int_0^\tau e^{A(\tau-\gamma)}B\bar{u}(\gamma)d\gamma + \int_0^\tau e^{A(\tau-\gamma)}w(\gamma)d\gamma \tag{4.12}$$

$$\bar{x}(t_i + \tau \mid t_i) = e^{A\tau}x_0(t_i) + \int_0^\tau e^{A(\tau-\gamma)}B\bar{u}(\gamma)d\gamma \tag{4.13}$$

From (4.12) and (4.13), the error between the actual system and predicted nominal state at time t_i is

$$x_e(t_i + \tau \mid t_i) = \int_0^\tau e^{A(\tau-\gamma)}w(\gamma)d\gamma \tag{4.14}$$

Hence the error dynamics are stable if and only if the open-loop system is stable, and the error dynamics are independent of the reference. However, it is easy to see that due to the presence of disturbance $w(t)$ the evolution of actual state may diverge from the nominal optimal state.

In order to mitigate the influence of the disturbance, we introduce an extra control term in (4.9), namely the disturbance rejection control, to keep the actual state close to the nominal state, for which the following form of the control input is used as similar to the tube-based MPC design [32] .

$$u(t) = \bar{u}(t) + K_d(x(t) - \bar{x}(t)) \tag{4.15}$$

where $\bar{u}(t)$, $\bar{x}(t)$ and $x(t)$ denotes the nominal control input in (4.9), the nominal closed-loop state and the measured state of i_d and i_q currents respectively. The nominal closed-loop state $\bar{x}$ is calculated based on the state equation with the nominal control input (4.9). In (4.15), the disturbance rejection control law (K_d) is designed off-line based on a stabilising state feedback control policy, to keep the evolution of the constrained system around the nominal trajectory in the presence of disturbance. In fact the disturbance rejection control plays a role of an active damping method here which will reduce the effect of LCL filter resonance on the closed-loop response.

Now to see how the error between the actual system state and nominal state propagates over time using the control input in (4.15), the actual system with state disturbance and the nominal system are defined as

$$\dot{x}(t) = Ax(t) + B\bar{u}(t) - BK_d(x(t) - \bar{x}(t)) + w(t) \tag{4.16}$$

$$\dot{\bar{x}}(t) = A\bar{x}(t) + B\bar{u}(t) \tag{4.17}$$

The error dynamics between the actual system state (4.16) and nominal state (4.17) at time step t can be expressed as.

$$x_e(t_i + \tau \mid t_i) = \int_0^{\tau} e^{A_k(\tau-\gamma)} w(\gamma) d\gamma \tag{4.18}$$

Thus, if the disturbance rejection control law K_d is chosen to stabilize the open-loop matrix A, the error dynamics will be stable as well. Furthermore the above approach gives a freedom of shaping the error signal by appropriately choosing the disturbance rejection control K_d.

It is easy to see that the robustness properties of proposed controller is fundamentally determined by the disturbance rejection controller K_d, which bounds on the error between actual state x and nominal state $\bar{x}$. For instance, one can expect to have a good disturbance rejection properties if a relatively large feedback gain K_d is selected, however this immediately limits the available nominal control input hence will affect the tracking performance of the nominal predictive controller. So there is an inevitable trade-off between disturbance rejection properties and controller performance. In the following section, we describe both part of control design for LCL filter in detail.

4.3.2 Nominal Predictive Current Control

The nominal predictive control part of the design is designed based on the response of the reduced-order model of (4.4) in the synchronous-reference frame. To achieve a zero steady-state error in the synchronous-reference frame, the model in (4.4) is augmented with integrators for output variables of the interest which in this case are active current i_d and reactive current i_q. Therefore, in conjunction with the original plant model, the augmented state space model is defined as:

$$\begin{bmatrix} \dot{z}(t) \\ \dot{y}(t) \end{bmatrix} = \overbrace{\begin{bmatrix} A_m & o_2^T \\ C_m & o_{2\times 2} \end{bmatrix}}^{A} \begin{bmatrix} z(t) \\ y(t) \end{bmatrix} + \overbrace{\begin{bmatrix} B_m \\ o_{2\times 2} \end{bmatrix}}^{B} \dot{u}(t) \tag{4.19}$$

$$y(t) = \underbrace{\begin{bmatrix} o_2 & I_2 \end{bmatrix}}_{C} \begin{bmatrix} z(t) \\ y(t) \end{bmatrix} \tag{4.20}$$

where I_2 is the identity matrix with dimensions 2×2; o_2 is a 2×2 zero matrix and two auxiliary variables are first chosen as $z(t) = \dot{x}_m(t)$ and $y(t) = C_m x_m(t)$, where $x_m(t) = [i_d(t) \;\; i_q(t)]^T$.

From this model, a pre-stabilisation technique as described in Chapter 3 is applied to tune the desired closed-loop response of the unconstrained MPC, which yields the following control signal form.

$$\dot{u}(t) = -Kx(t) + \dot{v}(t) \tag{4.21}$$

where the auxiliary control signal $v(t)$ represents the perturbations to the unconstrained MPC and the state-feedback law K in (4.21) is designed to place the closed-loop poles in the complex plane to satisfy the decay rate and damping ratio. Consequently using the control input (4.21), the closed-loop model prediction in the continuous-time is given by the following,

$$x_k(t_i + \tau \mid t_i) = e^{A_k \tau} x(t_i) + \int_0^{\tau} e^{A_k(\tau-\gamma)} B\dot{v}(\gamma) d\gamma \tag{4.22}$$

where $A_k = (A - BK)$. Following the same framework as in previous chapters, the auxiliary control signal $\dot{v}(\tau)$ for two switching inputs are parametrized using Laguerre function expansions.

For optimising the switching control inputs of S_d and S_q, the following quadratic cost function is considered.

$$J = \int_0^{T_p} \left[x_k(t_i + \tau \mid t_i)^T Q x_k(t_i + \tau \mid t_i) + \dot{v}(\tau)^T R_L \dot{v}(\tau) \right] d\tau \tag{4.23}$$

where Q and R_L are symmetric positive definite and positive semi-definite matrices, written as $Q > 0$ and $R_L \geq 0$ respectively. Substituting the model prediction and rearranging the above terms, and minimising with respect to the control input, the unconstrained minimization of the above cost function yields

$$\eta = -\Omega^{-1} \Psi x(t_i) \tag{4.24}$$

for the definition of Ω and Ψ (see also Chapter 3). By the principle of receding horizon control, the optimal auxiliary control input $\dot{v}(t)$ for the unconstrained problem at time t_i is

$$\dot{v}(t_i) = \begin{bmatrix} L_1^T(0) & 0_{L2}^T \\ 0_{L1}^T & L_2^T(0) \end{bmatrix} \begin{bmatrix} \eta_1 \\ \eta_2 \end{bmatrix} \tag{4.25}$$

where 0_{L1} and 0_{L2} are the zero column vectors with the same dimensions as $L_1(\tau)$ and $L_2(\tau)$. From (4.25), the derivative of the control signal $\dot{u}(t)$ without constraints is given by

$$\dot{u}(t) = -Kx(t) - \begin{bmatrix} L_1^T(0) & o_{L2}^T \\ o_{L1}^T & L_2^T(0) \end{bmatrix} K_{mpc} x(t) \tag{4.26}$$

where $K_{mpc} = -\Omega^{-1}\Psi$. Finally, the actual control signal $u(t)$ is given by

$$u(t_i) = u(t_i - \Delta t) + \dot{u}(t_i)\Delta t \tag{4.27}$$

where Δt is the sampling interval. Here, the first feedback control gain K is designed off-line whilst the actual control signal, corresponding to K_{mpc} is solved on-line.

4.3.3 Disturbance Rejection Control

The main role of the disturbance rejection control is to minimise the disturbance caused by the unmodeled dynamics of LCL filter and to keep the evolution of the i_d and i_q currents within neighbourhood of the optimal current trajectories. For this purpose, the main focus of K_d is to suppress the disturbance caused by the LCL filter resonance (i.e. the unmodeled disturbance of the LCL filter) such that the closed-loop disturbance rejection control guarantees the following finite frequency H_∞ constraints,

$$\sup_{\omega_1<\omega<\omega_2} \| G(j\omega) \|_\infty < \gamma \tag{4.28}$$

where $G(j\omega) = C_m(sI_{n_1} - A_m)^{-1}B_m$ is the transfer function of VSC. There are several control design techniques available to exist in the literature for finite frequency domain control problems. The most well-known approach is the weighting function approach where a low/band/highpass filter is added to the system in series to emphasise a particular frequency range. This method has been proven useful in practice, however, the additional weights increase the system complexity. Besides, the process of selecting appropriate weights can be time-consuming. An alternative approach is to grid the frequency axis. This approach has a practical significance, but it lacks a rigorous performance guarantee in the design process.

Departing from the conventional methodologies of weighting function and frequency gridding, recently the generalised KYP lemma (GKYP) based on celebrated KYP lemma have been developed by Iwasaki and Hara [43]. The GKYP lemma establishes the equivalence between a frequency domain property and an LMI over a finite frequency range, which is found to be very useful for the analysis and synthesis problems in practical applications, where imposed performance requirements are over chosen finite frequency ranges. In this work, the disturbance rejection control law based on GKYP lemma is considered. In particular, by using the generalized KYP lemma, the focus is on the design of a state feedback control law of k_d based on matrix inequalities such that the resulting closed-loop system is asymptotically stable with a prescribed level of disturbance attenuation in the frequency range of LCL filter resonance.

To facilitate the finite frequency H_∞ control design, extensive use of the following lemma is presented for which the proof can be found in [43],[38],[80].

Lemma 4.3.1 *(GKYP lemma [43]) Defining the transfer function $G(s)$ from the input to the output as*

$$G(j\omega) = C(j\omega I - A)^{-1}B + D \tag{4.29}$$

the following inequalities are equivalent

- *The frequency domain inequality*

$$\begin{bmatrix} G(j\omega) \\ I \end{bmatrix}^T \overbrace{\begin{bmatrix} 1 & 0 \\ 0 & -\gamma^2 \end{bmatrix}}^{\Pi} \begin{bmatrix} G(j\omega) \\ I \end{bmatrix} < 0 \tag{4.30}$$

- *The LMI*

$$\begin{bmatrix} A & B \\ I & 0 \end{bmatrix}^T \Xi \begin{bmatrix} A & B \\ I & 0 \end{bmatrix} + \begin{bmatrix} C & D \\ 0 & I \end{bmatrix}^T \Phi \begin{bmatrix} C & D \\ 0 & I \end{bmatrix} < 0 \tag{4.31}$$

  where for $Q > 0$ the matrix Γ can be defined based on the frequency region of interest as below

  - *For low frequency range $|\omega| < \omega_l$*

$$\Xi = \begin{bmatrix} -Q & P \\ P & \omega_l^2 Q \end{bmatrix} \tag{4.32}$$

  - *For middle frequency range $\omega_1 \leq \omega \leq \omega_2$*

$$\Xi = \begin{bmatrix} -Q & P + j\omega_c Q \\ P + j\omega_c Q & -\omega_l \omega_h Q \end{bmatrix} \tag{4.33}$$

$$\omega_c = (\omega_l + \omega_h)/2$$

- *For high frequency range* $|\omega| \geq \omega_h$

$$\Xi = \begin{bmatrix} Q & P \\ P & -\omega_h^2 Q \end{bmatrix} \tag{4.34}$$

Lemma 4.3.2 *(Projection Lemma [38],[80]) Let* Γ,Λ,Θ *be given, there exists a matrix* F *satisfying* $\Gamma F \Lambda + (\Gamma F \Lambda)^T + \Theta < 0$ *if and only if the following two conditions hold*

$$\Gamma^{\perp}\Theta\Gamma^{\perp^T} < 0, \Lambda^{T^{\perp}}\Theta\Lambda^{T^{\perp T}} < 0 \tag{4.35}$$

Lemma 4.3.3 *(Reciprocal Projection Lemma [80]) For a given matrix* $Y = Y^T > 0$*, the following statements are equivalent*

- $\psi + S + S^T < 0$
- *The following LMI is feasible for W*

$$\begin{bmatrix} \Psi + Y - (W + W^T) & S^T + W^T \\ S + W & -Y \end{bmatrix} < 0 \tag{4.36}$$

In this section, we are interested in designing a state feedback controller

$$u(t) = -Kx(t) \tag{4.37}$$

where K must be designed to reduce the resonant harmonics of the LCL filter. Based on the following state-space representation of the open-loop system,

$$\dot{x}(t) = Ax(t) + Bu(t) + B_0 w(t) \tag{4.38}$$

$$y(t) = Cx(t) \tag{4.39}$$

the closed-loop system is obtained by substituting (4.37) into (4.38)

$$\dot{x}(t) = \overbrace{(A - BK)}^{A_k} x(t) + B_0 w(t) \tag{4.40}$$

$$y(t) = Cx(t) \tag{4.41}$$

In next, we present the H_∞ control problem to minimise the H_∞ norm from the disturbance inputs $w(t)$ to the controlled output $y(t)$ over the fixed frequency range $\omega_l \le \omega_c \le \omega_h$, where the ω_c corresponds to the resonant frequency of LCL filter.

According to Lemma 4.3.1, the finite frequency specification in the middle frequency is given as

$$\begin{bmatrix} G(j\omega) \\ I \end{bmatrix}^T \Pi \begin{bmatrix} G(j\omega) \\ I \end{bmatrix} < 0, \omega_l \le \omega \le \omega_h \tag{4.42}$$

which is equivalent to

$$\begin{bmatrix} A_k & B_0 \\ I & 0 \end{bmatrix}^T \Xi \begin{bmatrix} A_k & B_0 \\ I & 0 \end{bmatrix} + \begin{bmatrix} C & D \\ 0 & I \end{bmatrix}^T \Phi \begin{bmatrix} C & D \\ 0 & I \end{bmatrix} < 0 \tag{4.43}$$

Following from the result in [43], an alternative condition of the above inequality can be rewritten as

$$W^T(J\Xi J^T + H\Pi H^T)W < 0 \tag{4.44}$$

$$U(J\Xi J^T + H\Pi H^T)U^T < 0 \tag{4.45}$$

where

$$J = \begin{bmatrix} I & 0 \\ 0 & I \\ 0 & 0 \end{bmatrix}, \Xi = \begin{bmatrix} -Q & P + j\omega_c Q \\ P + j\omega_c Q & -\omega_l \omega_h Q \end{bmatrix} \tag{4.46}$$

$$\Pi = \begin{bmatrix} I & 0 \\ 0 & -\gamma^2 I \end{bmatrix}, H = \begin{bmatrix} 0 & 0 \\ C^T & 0 \\ 0 & I \end{bmatrix} \tag{4.47}$$

$$W = \begin{bmatrix} I & 0 & 0 \\ 0 & 0 & I \end{bmatrix}^T, U = \begin{bmatrix} A_k^T & I & 0 \\ B_0^T & 0 & I \end{bmatrix}^T \tag{4.48}$$

According to the Lemma 4.3.2, the inequalities (4.44) and (4.45) are equivalent to

$$J\Xi J^T + H\Pi H^T + \Gamma F \Lambda + (\Gamma F \Lambda)^T \tag{4.49}$$

where

$$\Gamma = \begin{bmatrix} -I \\ A_k^T \\ B_0^T \end{bmatrix}, \Lambda = \begin{bmatrix} 0 \\ I \\ 0 \end{bmatrix}^T \tag{4.50}$$

Applying the Schur's complement to (4.49), we can obtain

$$\begin{bmatrix} -Q & P + j\omega_c Q - F & 0 & 0 \\ \star & -\omega_l \omega_h Q + F^T A_k + A_k F & F^T B_0 & C^T \\ \star & \star & -\gamma^2 I & 0 \\ \star & \star & \star & -I \end{bmatrix} < 0 \tag{4.51}$$

where the symbol ⋆ denotes the symmetric entries. Therefore, if there exists a positive scalar γ, symmetric matrices P, $Q > 0$ and matrix F such that the LMI (4.51) is feasible, then the closed-loop system in (4.40) satisfies the finite frequency condition in (4.42).

Now let us impose the stability condition, where we consider the following Lyapunov's inequality with a decay rate written as

$$(A - BK)^T P + P(A - BK) + 2\alpha P < 0 \tag{4.52}$$

$$P > 0 \tag{4.53}$$

where P is the Lyapunov matrix.

Letting $S^T = (A - BK)X + \alpha X$ and $\psi = 0$, the inequality with a decay rate can be rewritten as

$$\psi + S + S^T = (A - BK)X + X(A - BK)^T + 2\alpha X < 0 \tag{4.54}$$

where $X = P^{-1}$. According to the Lemma 4.3.3 the above equation is also equivalent to

$$\begin{bmatrix} Y - (W + W^T) & (A - BK)X + \alpha X + W^T \\ X(A - BK)^T + \alpha X + W & -Y \end{bmatrix} < 0 \tag{4.55}$$

Multiplying (4.55) on the left and on the right by $diag[I, P_s]$ with $P_s = X^{-1}$ gives

$$\begin{bmatrix} Y - (W + W^T) & (A - BK) + \alpha I + W^T P_s \\ (A - BK)^T + \alpha I + P_s W & -P_s Y P_s \end{bmatrix} < 0 \tag{4.56}$$

Multiplying (4.56) on the left and on the right by $diag[W^{T^{-1}}, I]$ and $diag[W^{-1}, I]$

respectively with $F = W^{-1}$ gives

$$\begin{bmatrix} F^T Y F - (F + F^T) & F^T(A - BK) + \alpha F^T + P_s \\ (A - BK)^T F + \alpha F + P_s & -P_s Y P_s \end{bmatrix} < 0 \qquad (4.57)$$

Applying the Schur complement in (4.57) yields

$$\begin{bmatrix} -(F + F^T) & F^T(A - BK) + \alpha F^T + P_s & F^T \\ (A - BK)^T F + \alpha F + P_s & -P_s Y P_s & 0 \\ F & 0 & -Y^{-1} \end{bmatrix} < 0 \qquad (4.58)$$

Considering the variable $Y = P_s^{-1}$ to (4.59) yields

$$\begin{bmatrix} -(F + F^T) & F^T(A - BK) + \alpha F^T + P_s & F^T \\ (A - BK)^T F + \alpha F + P_s & -P_s & 0 \\ F & 0 & -P_s \end{bmatrix} < 0 \qquad (4.59)$$

Since the inequalities in (4.51) and (4.59) are nonlinear, we perform a congruence transformation to (4.51) and (4.59) by pre and post-multiplying $\text{diag}\big(F^{-1}, F^{-1}, I, I\big)$ and $\text{diag}\big(F^{-1}, F^{-1}, I\big)$ respectively. Furthermore, by setting $\widehat{Q} = (F^{-1})QF^{-1}, \widehat{P} = (F^{-1})PF^{-1}, \widehat{P_s} = (F^{-1})P_sF^{-1}, \widehat{K} = KF^{-1}, \widehat{F} = F^{-1}$, we can derive the following LMI

$$\begin{bmatrix} -(\widehat{F} + \widehat{F^T}) & \widehat{F^T}A^T - B\widehat{K} + \alpha\widehat{F} + \widehat{P_s} & \widehat{F} \\ \star & -P_s & 0 \\ \star & \star & -\widehat{P_s} \end{bmatrix} < 0 \qquad (4.60)$$

$$\begin{bmatrix} -\widehat{Q} & \widehat{P} + j\omega_c\widehat{Q} - \widehat{F} & 0 & 0 \\ \star & -\omega_l\omega_h\widehat{Q} + sym(A\widehat{F} - B\widehat{K}) & B_0 & \widehat{F}^T C^T \\ \star & \star & -\gamma^2 I & 0 \\ \star & \star & \star & -I \end{bmatrix} < 0 \qquad (4.61)$$

where the symbol $\star$ and $sym(X)$ denotes symmetric entries and $X+X^T$ respectively. Therefore if inequalities (4.60)–(4.61) have a set of feasible solutions (i.e. there exits P, P_s, $Q>0$ and matrix F), the state feedback gain which satisfies the finite frequency specification in (4.28) is given by $K=\widehat{K}F^{-1}$.

4.3.4 Constrained Control

As was shown in (4.15), the control input to the VSC consists of the input of MPCC, $\bar{u}(t)$ and the disturbance rejection control input, $u_d(t)$

$$u(t_i)=\bar{u}(t_i)+\overbrace{K_d(x(t_i)-\bar{x}(t_i))}^{u_d(t_i)} \tag{4.62}$$

In order to keep the the amplitude of switching inputs within a linear modulation region, it is required that the control input of $u(t)$ is bounded by the hard constraint as shown below,

$$u_{min}\leq u(t_i)\leq u_{max} \tag{4.63}$$

where the u_{min} and u_{max} are the limits corresponding to the operation of the converter such that $u^{min}=[S_d^{min}\ S_q^{min}]^T$ and $u^{max}=[S_d^{max}\ S_q^{max}]^T$.

To express the above inequalities in terms of constrained input of $\bar{u}(t_i)$, we can rewrite (4.63) based on (4.62) as,

$$u_{min}-u_d(t_i)\leq\bar{u}(t_i)\leq u_{max}-u_d(t_i) \tag{4.64}$$

Since the control input $\bar{u}(t_i)$ is parametrised using the orthonormal basis functions in the design of predictive control as shown

$$u(t_i)=u(t_i-\Delta t)+\begin{bmatrix} L_1^T(0) & o_{L2}^T \\ o_{L1}^T & L_2^T(0)\end{bmatrix}\begin{bmatrix}\eta_1\\ \eta_2\end{bmatrix}\Delta t \tag{4.65}$$

where Δt is the sampling interval for implementation. The constraints for the control signal for the lower limit is represented as

$$u^{min} - u_d(t) - u(t_i - \Delta t) \leq \begin{bmatrix} L_1^T(0) & o_{L2}^T \\ o_{L1}^T & L_2^T(0) \end{bmatrix} \begin{bmatrix} \eta_1 \\ \eta_2 \end{bmatrix} \Delta t \tag{4.66}$$

for the upper limit as

$$\begin{bmatrix} L_1^T(0) & o_{L2}^T \\ o_{L1}^T & L_2^T(0) \end{bmatrix} \begin{bmatrix} \eta_1 \\ \eta_2 \end{bmatrix} \Delta t \leq u^{max} - u_d(t_i) - u(t_i - \Delta t) \tag{4.67}$$

Based on the above constraints and given that $\bar{u}(t_i)$ is defined by $\bar{u} = [S_d \;\; S_q]^T$, the predictive control problem with hard constraints imposed in the design becomes the problem of finding the optimal solution of the quadratic cost function

$$\begin{aligned} &\underset{\eta}{\text{minimize}} \quad J = \eta^T \Omega \eta + 2\eta^T \Psi x(t_i) \\ &\text{subject to} \quad \begin{bmatrix} L_1^T(0) & o_{L2}^T \\ o_{L1}^T & L_2^T(0) \end{bmatrix} \begin{bmatrix} \eta_1 \\ \eta_2 \end{bmatrix} \Delta t \leq \begin{bmatrix} u^{max} - u_d(t_i) - u(t_i - \Delta t) \\ -u^{min} - u_d(t) - u(t_i - \Delta t) \end{bmatrix} \end{aligned} \tag{4.68}$$

As before, primal-dual method of Hildrethis Quadratic Programming algorithm is chosen to provide the numerical solution to the above constrained optimal problem [109]

4.4 Experimental Results

4.4.1 MPCC with finite frequency H_∞ control

The experimental validation of the method proposed in section 4.3 is carried out based on the system parameter shown in Table 4.2. For controller parameters, The Laguerre parameters are selected as $N1 = N2 = 4$ and $p1 = 1.5$; $p2 = 1.5$.

Table 4.2: System parameters of grid-connected VSC with an LCL filter

Symbol	Parameter Name	Value	Unit
L_s	Input filter inductance (converter side)	2.0	mH
L_g	Input filter inductance (grid side)	0.75	mH
C_f	Filter Capacitance	16.1	μF
R_s	Input filter ESR (converter side)	0.1	Ω
R_g	Input filter ESR (grid side)	0.1	Ω
C_{dc}	DC-link Capacitance	700	μF
R_{dc}	DC-link load resistance	20–40	Ω
V_g	Grid Voltage	30	V
F_g	Grid Frequency	50	Hz

$Q = C^TC$ and $R = 0.2I$. The prediction horizon is selected as T_p = 50 for the nominal MPCC. The disturbance rejection control law in (4.69) is obtained by solving set of LMI (4.60)–(4.61) for the frequency range between $10000 \le \omega \le 12000$ [rad/sec] with decay rate $\beta = 200$.

$$K_d = \begin{bmatrix} -0.0228 & 0.0148 & 0.0017 & -0.0001 \\ -0.0149 & -0.0233 & -0.0001 & 0.0008 \end{bmatrix} \tag{4.69}$$

In order to validate the proposed method and to show the comparison with and without the disturbance rejection control, an experiment validation is carried out at the beginning with the disturbance rejection control input u_d first disabled, hence the nominal current control based on reduced-order model is only used to control the i_d and i_q current. Consequently, the phase current of LCL filter in this period, shown in Figure 4.10 contains the excessive harmonics due to the resonance in the LCL filter. Similarly, the i_d and i_q current of LCL filter is also distorted as shown in Figure 4.11. The frequency spectrum in Figure 4.12 confirms the presence of the LCL filter resonance in the distorted phase current in Figure 4.10.

In order to suppress this resonant harmonics in the current, the disturbance

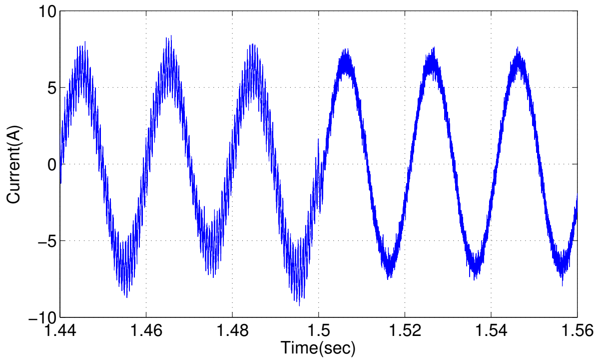

Figure 4.10: The response of phase current I_a of LCL filter with/without the disturbance rejection control: Prior to 1.5 sec, disturbance rejection control is disabled and at 1.5 sec a small transient response in the phase current is caused by switching on the disturbance rejection control.

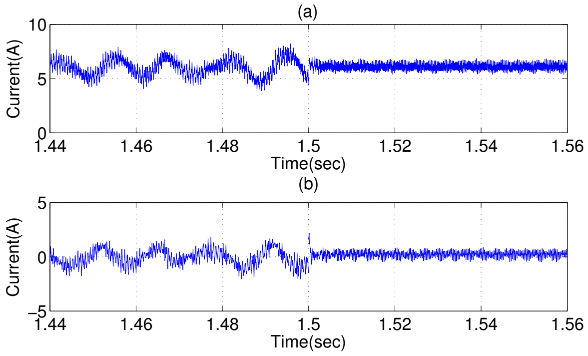

Figure 4.11: The response of I_d (a) and I_q (b) current of LCL filter with/without the disturbance rejection control: at 1.5 sec, the disturbance rejection control is enabled to damp the LCL filter resonance

rejection controller is activated at 1.5 sec. As a result, a reduction of resonant harmonics is achieved which can be seen from the response of phase current and the i_d and i_q current in Figure. 4.10 and 4.11 respectively. More clearly, the frequency spectrum of the phase current in Figure 4.13 shows the relative reduction of LCL filter resonance harmonics compared to Figure 4.12.

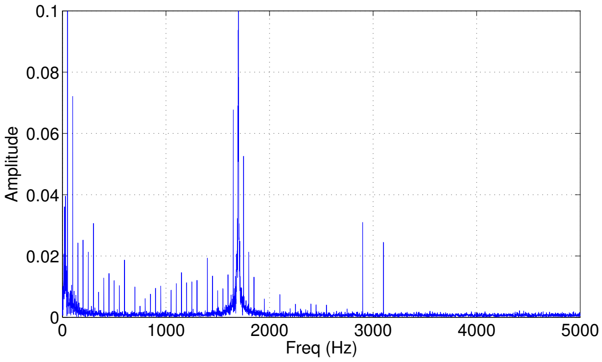

Figure 4.12: Frequency spectrum of the phase current I_a of LCL filter without the disturbance rejection control

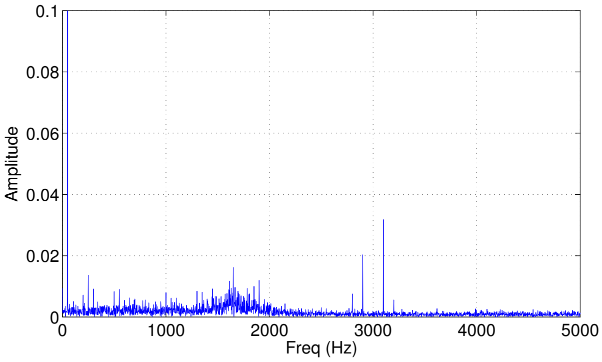

Figure 4.13: Frequency spectrum of the phase current I_a of LCL filter with the disturbance rejection control

Comparison with Entire-frequency approach

To illustrate the effectiveness of the proposed disturbance rejection controller in the finite frequency domain, a comparison is made between the finite frequency controller in section and H_∞ state feedback controller, which is designed over the entire frequency range based on the following condition.

$$\begin{bmatrix} AX + XA^{'} + B_0Y + Y^{'}B_0^{'} & \star & \star \\ -CX + DY & -\gamma^2 I & \star \\ B_0^{'} & C^{'} & -1 \end{bmatrix} < 0 \tag{4.70}$$

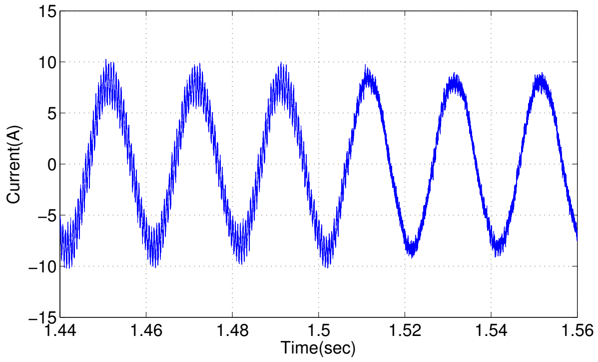

Figure 4.14: The response of phase current based on entire frequency approach

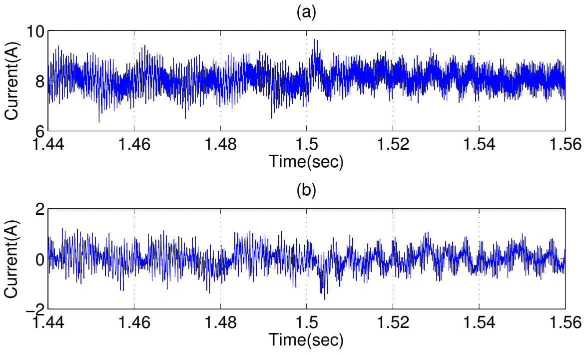

Figure 4.15: The response of Idq current based on entire frequency approach

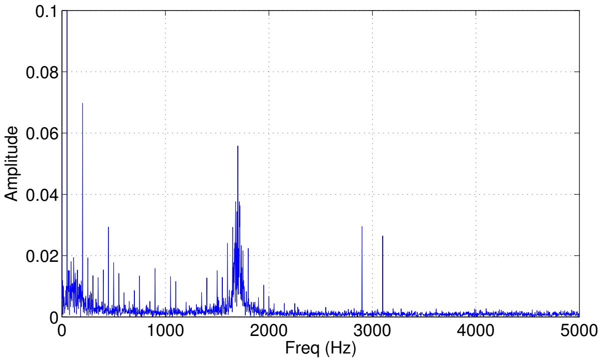

Figure 4.16: The frequency spectrum phase current based on entire frequency approach

where the symbol $\star$ denotes the term induced by symmetry. The resulting control law based on LMI (4.70) with the attenuation factor set to $\gamma = 200$ is obtained as

$$K_d^{\infty} = \begin{bmatrix} -0.0245 & 0.0515 & -0.0004 & 0.0308 \\ -0.0550 & -0.0207 & -0.0328 & 0.0022 \end{bmatrix} \tag{4.71}$$

To compare the K_d^{∞} and K_d in (4.69), the nominal MPCC part and test conditions are kept same and the the amount of attenuation of resonant harmonics in the current are observed.

The response of phase current and i_d and i_q currents based on the disturbance rejection control in (4.71) are shown in Figure 4.14 and Figure 4.15 respectively. In overall, the results shows similar responses to the previous section where damping of LCL filter resonance occurs after activating the disturbance rejection controller at 1.5 sec. For a precise comparison, the frequency-spectrum of phase current in Figure 4.16 is compared to Figure 4.13. This result shows that the finite-frequency controller approach gives a better attenuation of LCL filter resonant harmonics than the entire-frequency approach.

Rectification Mode

Having validated the performance of the proposed method in attenuating the LCL filter resonance, the following two sections presents experimental results for the rectification and the regeneration mode. For both modes of the operation, the control objective is to control the i_d current to follow the reference input i_d^* current, and i_q current at zero for unity power factor.

To validate the proposed controller in rectification mode, a step change in the reference input of i_d^* current is applied from 6A to 10A. The response of i_d current in Figure 4.17 (a) shows a good tracking performance to a reference

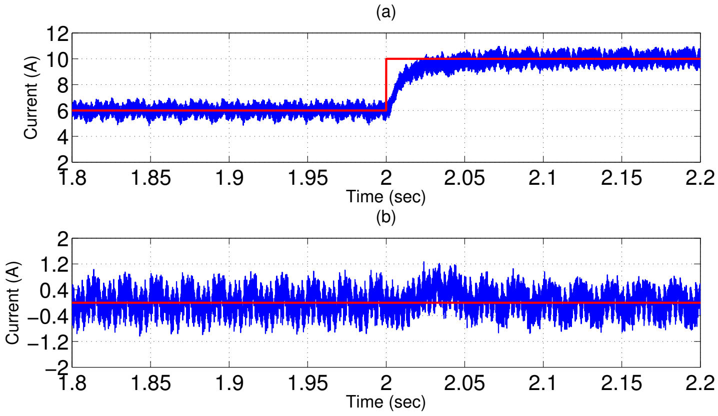

Figure 4.17: Plot of phase current with input constraints for the case when the input constraint is violated when the disturbance rejection controller is activated after 1.5 *sec*.

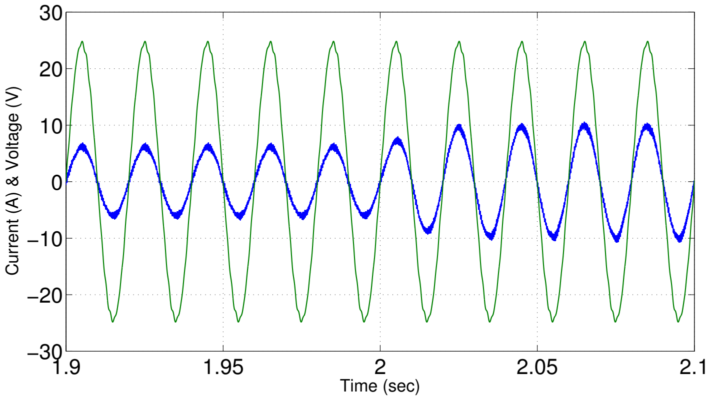

Figure 4.18: Plot of phase current with input constraints for the case when the input constraint is violated when the disturbance rejection controller is activated after 1.5 *sec*.

input while drawing an extra current from the grid, i_q is also well maintained around zero (see Figure 4.17 (b)) which results in zero phase shift between phase voltage and phase current (i.e unity power factor) as shown in Figure 4.18.

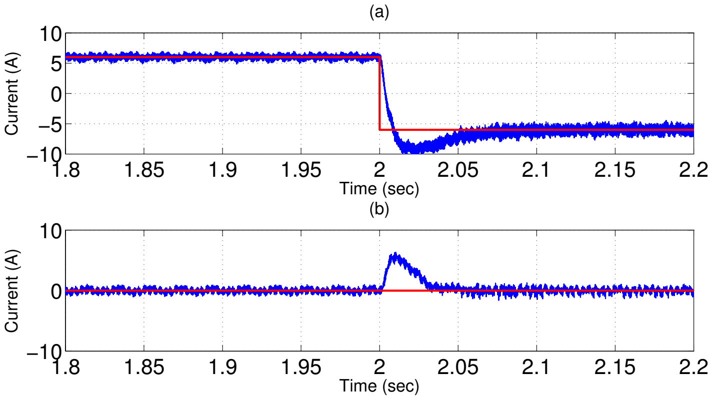

Figure 4.19: Plot of phase current with input constraints for the case when the input constraint is violated when the disturbance rejection controller is activated after 1.5 sec.

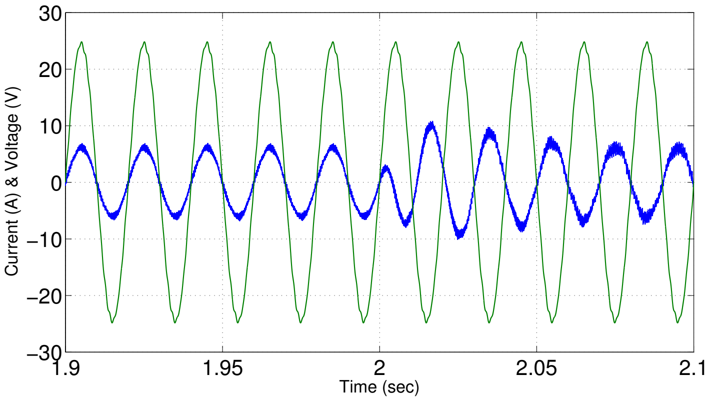

Figure 4.20: Plot of phase current with input constraints for the case when the input constraint is violated when the disturbance rejection controller is activated after 1.5 sec.

Regeneration Mode

To experimentally validate the proposed controller in regeneration mode, the VSC is first kept to operate at rectification mode at the start of the experiment. At around $2sec$, an extra current is then injected in the DC-bus, which resulted in initial overshoot of DC bus voltage. This in turn caused an external reference generator (in this case PI control) to change the reference input of i_d current.

Figure 4.19 shows the closed-loop responses of i_d and i_q to a step change in the reference inputs from 6A to -6A. The result shows a good tracking response of i_d current to the reference input and the negative sign of i_d current after 2 sec indicates that the current flow is reversed and the extra current injected into DC bus is converted and feeds back into the main grid. The response i_q current in Figure 4.19 (b) also shows that the reactive current is well regulated around zero. To confirm the unity power factor operation, Figure 4.20 show the corresponding phase current and voltage output which are 180° out of phase each other in regeneration mode.

Constrained Control

An experimental validation is carried out to test the input constraints in the proposed MPCC with disturbance rejection control. For an illustrative purpose, a test is first carried out by considering the saturation limit for the nominal MPCC control input only, in other words the disturbance rejection control input u_d is omitted from the upper and lower saturation limit in (4.66) and (4.67) as shown below.

$$u^{min} - u(t_i - \Delta t) \leq \begin{bmatrix} L_1^T(0) & o_{L2}^T \\ o_{L1}^T & L_2^T(0) \end{bmatrix} \begin{bmatrix} \eta_1 \\ \eta_2 \end{bmatrix} \Delta t \leq u^{max} - u(t_i - \Delta t) \tag{4.72}$$

The main purpose of this test is to see the effect of disturbance control input on the feasibility of the original input constraint.

The response of control inputs for the test is shown in Figure 4.21, where we can see that after the disturbance rejection controller is activated at 1.5 sec, the original input constraints are violated due to the disturbance rejection inputs. There are almost no change in the response of i_{dq} current as shown in Figure 4.22.

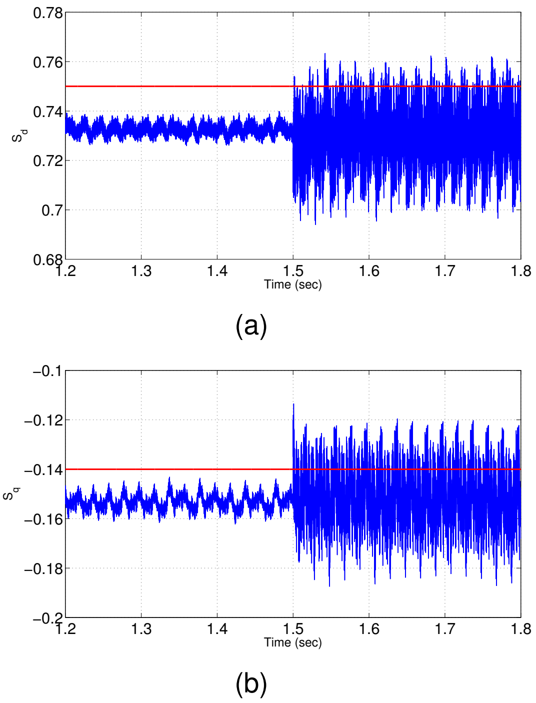

(a)

(b)

Figure 4.21: Plot of control inputs S_d (a) and S_q (b) with constraints set to set to 0.75 and -0.14 respectively: The input constraint (shown in red) for both inputs are violated when the disturbance rejection controller is activated after 1.5 sec.

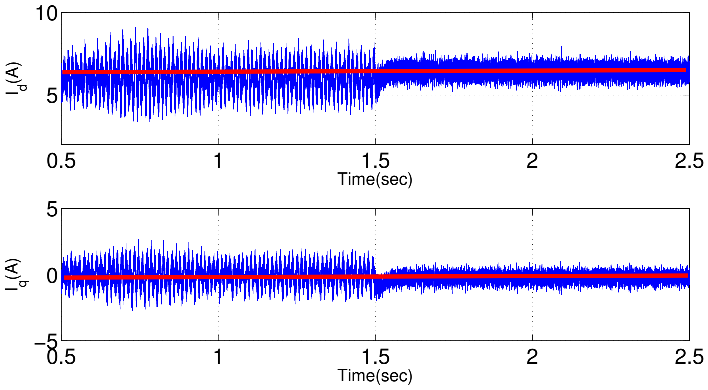

Figure 4.22: The response of i_d and i_q currents for the case when the input constraint is violated when the disturbance rejection controller is activated after 1.5 sec.

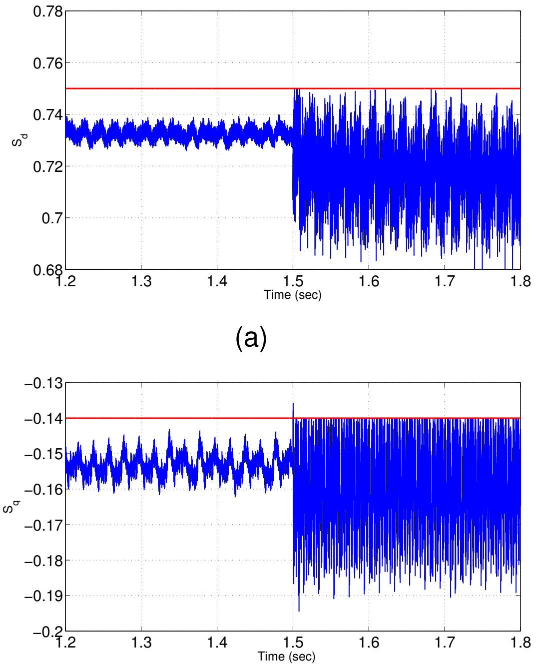

(a)

(b)

Figure 4.23: Plot of control inputs S_d (a) and S_q (b) with constraints set to set to 0.75 and -0.14 respectively: The input constraint (shown in red) for both inputs are violated when the disturbance rejection controller is activated after 1.5 sec.

Now, the proposed control input constraint of the following linear inequalities is applied.

$$u^{min} - u_d(t_i) - u(t_i - \Delta t) \leq \begin{bmatrix} L_1^T(0) & o_{L2}^T \\ o_{L1}^T & L_2^T(0) \end{bmatrix} \begin{bmatrix} \eta_1 \\ \eta_2 \end{bmatrix} \Delta t \leq u^{max} - u_d(t_i) - u(t_i - \Delta t) \quad (4.73)$$

With the use of this inequality constraints, the input constraints of the nominal MPCC is reduced by the amount of control input required for the disturbance rejection, hence the feasibility of the original input constraint can be still guaranteed in the presence of disturbance. This is similar to a constraint-tightening approach which has been used to guarantee the feasibility in robust MPC problem.

Figure 4.23 is the response of control inputs based on (4.73) which shows

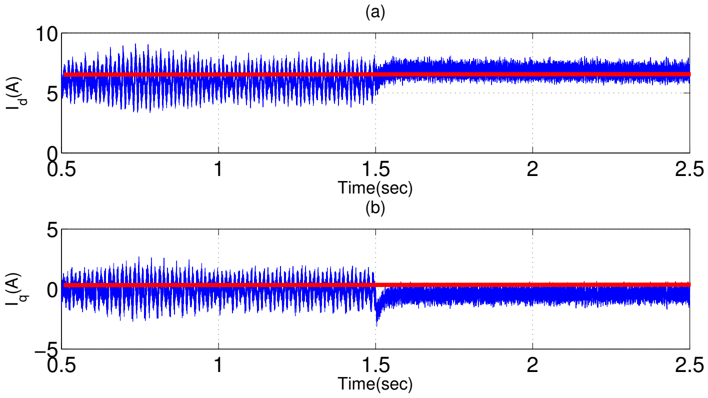

Figure 4.24: Plot of phase current with input constraints for the case when the input constraint is violated when the disturbance rejection controller is activated after 1.5 sec.

that the input constraints are satisfied even when the disturbance rejection control is activated after 1.5 sec. As mentioned, this is achieved by tightening the original input constraint for the nominal MPCC. However, as shown in Figure 4.24 the tracking performance of i_q current is affected since the available control input is reduced as a result of tightened constraints. (Note that the switching input constraints are chosen aggressively to highlight the effect of constraint tightening.)

Comparison with L filter

Lastly, the response of input current based on L filter and LCL filter is compared and shown in Figure 4.25 and Figure 4.26. As can be seen that if the LCL filter resonance is sufficiently damped, the overall current harmonics in LCL filter is significantly lower than the L filter despite having the same size of passive components which is the main benefit of employing an LCL filter.

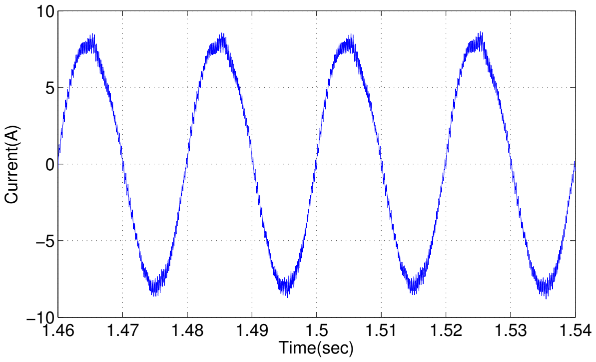

Figure 4.25: The response of phase current based on L filter

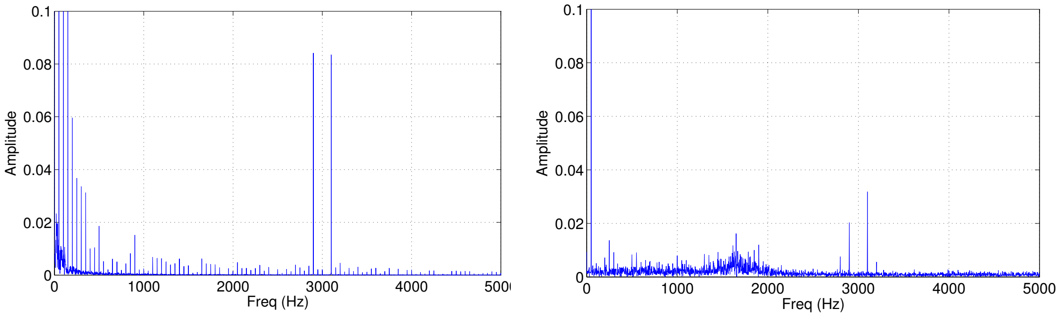

(a)

(b)

Figure 4.26: Comprison of frequency spectrum of phase current between (a) L filter and (b) LCL filter

4.5 Conclusions

This chapter presented a model predictive current control method for grid-connected VSC with an LCL filter. The presented method in this chapter utilised a reduced-order model of LCL filter, which required only the input currents, namely i_d and i_q current and their derivatives as system states. However, in order to overcome the LCL filter resonance issue with a reduce-order model design, a separate disturbance rejection controller is designed to reduce the effect of resonance. In the experimental results, it showed a satisfactory performance of both tracking reference inputs and mitigating the LCL filter resonance.

Finally the constrained control performance is analysed where we highlighted the effect of constraint tightening on the control performance.

CHAPTER 5

Model Predictive Resonant Current Control

5.1 Introduction

The chapter presents a model predictive control scheme that tracks periodic reference current inputs of i_α and i_β in the stationary frame. The main idea of the proposed scheme is based on the internal model principle which states that a feedback control system must contain the resonant module of $\frac{1}{s^2+\omega^2}$ to track sinusoidal type reference inputs with zero steady-state errors. To satisfy this condition, the proposed control scheme embeds the resonant module of $\frac{1}{s^2+\omega^2}$ in the model of VSC in the stationary frame, where ω is the main grid frequency. From this model, the future prediction of states and optimum switching inputs are computed by minimizing the error function between the predicted and measured input currents (i_α and i_β).

The design of the proposed control scheme which we referred to as model predictive resonant controller (MPRC) is described in Section 5.2. A robust MPRC scheme is also presented to improve the robustness under grid frequency variations. In Section 5.3, an extension of MPRC is presented to selectively compensate for multiple harmonics caused by the grid voltage harmonics (mainly fifth and seventh in three-phase systems). The proposed scheme builds on a similar idea as in [65], to control the nominal current dynamics and to null the harmonic at a specific frequency by resonant harmonic compensator which ensures the overall system stability in the presence of harmonic distortions. To close the chapter the experimental validations are presented.

5.2 Model Predictive Resonant Current Control

Conventionally the majority of control design methods for the current control have been implemented in the synchronous-reference frame. From the control design point of view, the synchronous-reference frame implementation allows a straightforward application of classical controller synthesis tools, since AC variables, such as grid voltages and currents appear in DC vector quantities, which leads to a simple derivation of a LTI model. However, the computational load required for this transformation is substantial due to the constant tracking of the phase angle, where for a grid-connected VSC a phase locked loop (PLL) is often used to track the phase angle of the grid voltage.

Another transformation called stationary frame also exists for the control system design of the three phase VSC [88]. The main advantage of transforming into this frame is the reduction of computational loads due to a simpler transformation as in (5.1),

$$T_{\alpha\beta} = \begin{bmatrix} 1 & -\frac{1}{2} & -\frac{1}{2} \\ 0 & \frac{\sqrt{3}}{2} & -\frac{\sqrt{3}}{2} \end{bmatrix} \tag{5.1}$$

Note also that the phase angle information is also no longer required in the transformation.

The overview of the proposed MPRC system based on this frame of transformation is shown in Figure 5.1. The main objective of the MPRC system is to control the $i_{\alpha\beta}$ in the stationary frame, where the reference input of respective currents are assumed to be given from the outer control loop. As it also can be seen in the figure, the main control system no longer requires a grid-

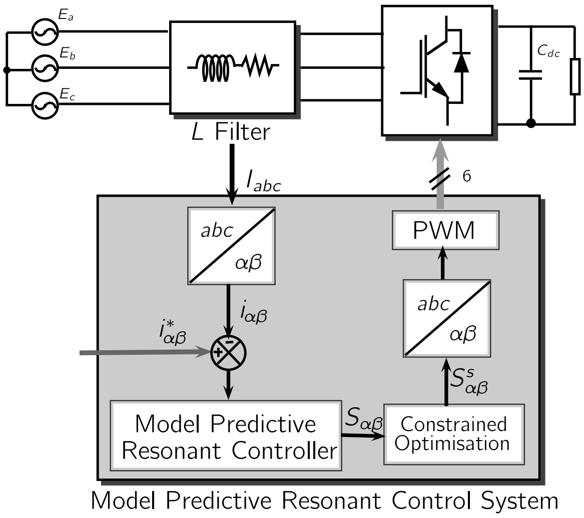

Figure 5.1: An overview of the proposed MPRC system: $i^*_{\alpha\beta}$ are the reference current inputs and '$abc/\alpha\beta$' block corresponds to the stationary transformation based on (5.1). $S_{\alpha\beta}$ and $S^s_{\alpha\beta}$ are unconstrained and constrained control inputs respectively.

synchronisation module (i.e. PLL) due to a simpler transformation in 5.1.

To proceed with the design of MPRC, the model of VSC in terms of i_α and i_β in the stationary frame is first considered as shown below,

$$\begin{aligned} L_s\frac{di_\alpha}{dt} &= -Ri_\alpha + e_\alpha - v_\alpha \\ L_s\frac{di_\beta}{dt} &= -Ri_\beta + e_\beta - v_\beta \end{aligned} \tag{5.2}$$

where e_α,e_β and i_α, i_β are the stationary frame grid voltages and input currents respectively. v_α and v_β denote control inputs with

$$v_\alpha = \frac{S_\alpha v_{dc}}{2} \tag{5.3}$$

$$v_\beta = \frac{S_\beta v_{dc}}{2} \tag{5.4}$$

where S_α and S_β are the switching functions. The DC-link bus voltage equation can be expressed as,

$$C\frac{dv_{dc}}{dt} = \frac{3(S_\alpha \cdot i_\alpha + S_\beta \cdot i_\beta)}{4} - \frac{v_{dc}}{R_L} \tag{5.5}$$

Considering only the dynamics of input currents in the stationary frame (i.e. i_α and i_β currents), an LTI model in the following equation is used in the design of the MPRC.

$$\dot{x}_m(t) = A_m x_m(t) + B_m u(t) \tag{5.6}$$

$$y(t) = C_m x_m(t) \tag{5.7}$$

where A_m, B_m and C_m are defined as

$$A_m = \begin{bmatrix} -\frac{R}{L_s} & 0 \\ 0 & -\frac{R}{L_s} \end{bmatrix}, B_m = \begin{bmatrix} \frac{-v_{dco}}{2L_s} & 0 \\ 0 & \frac{-v_{dco}}{2L_s} \end{bmatrix} \tag{5.8}$$

$$C_m = \begin{bmatrix} 1 & 1 \\ 0 & 1 \end{bmatrix}, x_m = \begin{bmatrix} i_\alpha \\ i_\beta \end{bmatrix}, u = \begin{bmatrix} S_\alpha \\ S_\beta \end{bmatrix} \tag{5.9}$$

v_{dco} is the chosen operating voltage of the DC-link bus. Since the stationary frame is based on the main frequency rather than phase angle, in contrast to the synchronous reference frame, the reference inputs in this frame are sinusoidal signals with their periods determined by the frequency of the main grid.

In order to track the sinusoidal inputs with no steady state error, the resonant module of the form $\frac{1}{s^2+\omega^2}$ is embedded in the model in (5.6). This is done by first defining the auxiliary control signal $u_s(t)$ as the function that satisfies the following differential equation

$$\frac{d^2u(t)}{dt^2} + \omega_o^2 u(t) = u_s(t) \tag{5.10}$$

and the auxiliary state variable $z(t)$ as

$$\frac{d^2x_m(t)}{dt^2} + \omega_o^2 x_m(t) = z(t) \tag{5.11}$$

where in this case ω_o is the frequency of the main grid. From (5.10) it is seen that $u_s(t)$ is the inversely filtered control signal by the sinusoidal dynamics. By using the auxiliary variables, the state space model in (5.6) can be transformed into

$$\frac{dz(t)}{dt} = A_m z(t) + B_m u_s(t) \tag{5.12}$$

and note that

$$\begin{aligned}
\frac{d^2y(t)}{dt^2} &= C_m \frac{d^2x_m}{dt^2} \\
&= C_m \frac{d^2x_m}{dt^2} + \omega_o^2 C_m x_m(t) - \omega_o^2 C_m x_m(t) \\
&= C_m z(t) - \omega_o^2 y(t)
\end{aligned}$$

Finally, an augmented state space model is expressed as

$$\begin{bmatrix} \frac{dz(t)}{dt} \\ \frac{d^2y(t)}{dt^2} \\ \frac{dy(t)}{dt} \end{bmatrix} = \overbrace{\begin{bmatrix} A_m & 0_2 & 0_2 \\ C_m & 0_2 & -\omega_0^2 I_2 \\ 0_2 & I_2 & 0_2 \end{bmatrix}}^{A} \overbrace{\begin{bmatrix} z(t) \\ \frac{dy(t)}{dt} \\ y(t) \end{bmatrix}}^{x} + \overbrace{\begin{bmatrix} B_m \\ 0_2 \\ 0_2 \end{bmatrix}}^{B} u_s(t) \tag{5.13}$$

where I_2 and 0_2 are 2×2 identity and zero matrices respectively.

Based on the augmented model in (5.13) where the control signal to the model is the filtered control, at the current time, t_i, the predicted state variable $x(t_i + \tau \mid t_i)$ at the future time τ, $\tau > 0$ is described by the following equation

$$x(t_i + \tau \mid t_i) = e^{A\tau} x(t_i) + \int_0^{\tau} e^{A(\tau-\gamma)} B u_s(\gamma) d\gamma \tag{5.14}$$

From a practical point of view, there are a couple of problems associated with the use of the augmented system matrix in the predictive control design. First, the open-loop eigenvalues of the augmented matrix (5.13) have complex eigenvalues on the imaginary axis, which as previously illustrated in section 3.3, it will lead to an numerical conditioning problem. Second, the embedded resonant mode of the form $\frac{1}{s^2+\omega^2}$ assumes the grid frequency to be fixed at the resonant frequency. However it is generally known that the grid frequency fluctuates around the main frequency [96],[65],[6] and the magnitude of fluctuation depends on the grid condition. As summarized in [6], for grid-connected systems a control strategy must allow the system to ride-through under a large variation of grid condition. In particular with the grid frequency, a frequency variation as large as $\pm 1Hz$ for PV systems [4] and $\pm 5Hz$ for WT systems [7] can be expected which must be coped by the controller.

In the design of Proportional-Resonant (PR) control design [65],[88], where the PR controller of $G(s)$ is defined as

$$G(s) = K_p + K_r \frac{s}{s^2 + \omega^2} \tag{5.15}$$

The common remedies for the above PR controller for the frequency variation is to introduce a damping term (ω_c) to mitigate the sensitivity issue with frequency variation as below

$$G(s) = K_p + K_r \frac{\omega_c s}{s^2 + 2\omega_c s + \omega^2} \tag{5.16}$$

or as suggested in [6] some type of adaptive frequency scheme is necessary. Introducing the term ω_c in (5.16) however reduces the magnitude at the resonant frequency, therefore a designer must tune the frequency response of (5.16) to satisfy both tracking and robust performance.

In the case of MPRC considered here, if there is also a sufficient fluctuation of the grid frequency from the resonant frequency (ω), a mismatch between the state prediction in (5.14) and the actual state will affect the tracking performance and even possibly the stability of MPRC.

In order to improve the robustness against the frequency fluctuation while also improving the numerical conditioning, the proposed MPRC design is built on the concept of closed-loop paradigm (CLP) approach as described in section 3.4, which has the following control input

$$u_s(t) = -Kx(t) + \dot{v}(t) \tag{5.17}$$

where K is an unconstrained linear control law and $\dot{v}(t)$ is the auxiliary control input. Since the auxiliary control input $\dot{v}(t)$ in (5.17) is used for constraint handling, the design of K is the key focus here to ensure the robustness against the grid frequency fluctuation.

In order to systematically find a robustly stabilising control law K, we will first derive the uncertain system matrix A in terms of the embedded resonant frequency of ω which we assume to vary within a known interval,

$$\omega \in [\omega^{min}, \quad \omega^{max}] \tag{5.18}$$

where ω^{min} and ω^{max} are the expected minimum and maximum grid frequency respectively during the operation of the converter.

From (5.18), the uncertain augmented model in terms of the resonant frequency variation is specified as follows

$$A_1 = \begin{bmatrix} A_m & 0_2 & 0_2 \\ C_m & 0_2 & -\omega_{min}^2 I_2 \\ 0_2 & I_2 & 0_2 \end{bmatrix} \quad A_2 = \begin{bmatrix} A_m & 0_2 & 0_2 \\ C_m & 0_2 & -\omega_{max}^2 I_2 \\ 0_2 & I_2 & 0_2 \end{bmatrix} \tag{5.19}$$

Based on the uncertain model of grid frequency, a robustly stabilising control law K is found from the LQR-LMI optimisation problem (see Section 3.3.3 for detailed derivation) as follows,

$$\begin{aligned} \underset{X}{\text{minimize}} \quad & \mathbf{Tr}(QP) + \mathbf{Tr}(X) \\ \text{subject to} \quad & A_i P + P A_i^T + BY + Y^T B^T < 0 \\ & \begin{bmatrix} X & R^{\frac{1}{2}} Y \\ Y^T R^{\frac{1}{2}} & P \end{bmatrix} > 0, P > 0, i = 1, 2 \end{aligned} \tag{5.20}$$

if the above condition is satisfied to yield symmetric matrices $X \in \mathbb{R}^{n \times n}$ and $Y \in \mathbb{R}^{m \times n}$, then the LQR controller given by $K = YX^{-1}$ ensures the stability of closed-loop system under the grid frequency variations.

Assuming that we have obtained a robust control law K, substituting the closed-loop control signal in (4.21) into the state dynamic equation, the closed-loop model prediction is obtained as follows,

$$x_k(t_i + \tau \mid t_i) = e^{A_k \tau} x(t_i) + \int_0^{\tau} e^{A_k(\tau - \gamma)} B \dot{v}(\gamma) d\gamma \tag{5.21}$$

where $A_k = (A - BK)$. Based on the predictions of the unconstrained optimal behaviour in (5.21), the global optimal control input is found with respect to the cost function,

$$J = \int_0^{T_p} \left[x_k(t_i + \tau \mid t_i)^T Q x_k(t_i + \tau \mid t_i) + \dot{v}(\tau)^T R \dot{v}(\tau) \right] d\tau \tag{5.22}$$

From herein, each auxiliary input signal of $\dot{v}(t)$ is described with a Laguerre function expansion, where by choosing two continuous-time Laguerre function vectors $L_1(\tau)$ and $L_2(\tau)$, the control signal $\dot{v}$ is represented by

$$\dot{v}(\tau) = \begin{bmatrix} L_1^T(\tau) & 0_{L2}^T \\ 0_{L1}^T & L_2^T(\tau) \end{bmatrix} \begin{bmatrix} \eta_1 \\ \eta_2 \end{bmatrix} \tag{5.23}$$

where 0_{L1} and 0_{L2} are the zero column vectors with the same dimensions as $L_1(\tau)$ and $L_2(\tau)$. The predicted state vector, denoted by $x(t_i + \tau \mid t_i)$ based on the control parametrization is described by the following equation

$$x(t_i + \tau \mid t_i) = e^{A_k \tau} x(t_i) + \int_0^\tau e^{A_k(\tau-\gamma)} \begin{bmatrix} B_1 L_1^T(\gamma) & B_2 L_2^T(\gamma) \end{bmatrix} d\gamma \begin{bmatrix} \eta_1 \\ \eta_2 \end{bmatrix} \tag{5.24}$$

With $\eta^T = [\eta_1^T \ \eta_2^T]$, the cost function used in MPRC has the form

$$J = \int_0^{T_p} e(t_i + \tau \mid t_i)^T Q e(t_i + \tau \mid t_i) d\tau + \eta^T R_L \eta \tag{5.25}$$

where

$$e(t_i + \tau \mid t_i) = \begin{bmatrix} r'(t) - y(\tau \mid t_i) \\ r(t_i) - y(\tau \mid t_i) \end{bmatrix} \tag{5.26}$$

where $r(t_i)$ is the set-point and $r'(t_i)$ is derivative of the set-point. The weighting matrices Q and R_L are symmetric positive definite and positive semi-definite matrices, written as $Q > 0$ and $R_L \geq 0$ respectively. By substituting the predicted state variables into the cost function, the unconstrained minimization with respect to the parameter vector η in the cost function (3.75), is given as follows

$$\eta = -\Omega^{-1} \Psi x(t_i) \tag{5.27}$$

By the principle of receding horizon control, the optimal control $\dot{v}(t)$ for the unconstrained problem at time t_i is

$$\dot{v}(t_i) = \overbrace{\begin{bmatrix} L_1^T(0) & o_{L2}^T \\ o_{L1}^T & L_2^T(0) \end{bmatrix}}^{L_0^T} \begin{bmatrix} \eta_1 \\ \eta_2 \end{bmatrix} \tag{5.28}$$

Now, the control signal $u_s(t)$ is given by

$$u_s(t) = (-K + K_{mpc})x(t) \tag{5.29}$$

where $K_{mpc} = -L_0^T \Omega^{-1} \Psi$. From the control signal $u_s(t)$, and using the relationship between $u_s(t)$ and $u(t)$ from (5.10), the actual control signal $u(t)$ can be derived by the following equation,

$$\begin{bmatrix} \dot{u}(t_i) \\ u(t_i) \end{bmatrix} = \begin{bmatrix} 0 & -\omega_o^2 I_2 \\ I_2 & 0 \end{bmatrix} \begin{bmatrix} \dot{u}(t_i) \\ u(t_i) \end{bmatrix} \Delta t + \begin{bmatrix} I_2 \\ 0 \end{bmatrix} u_s(t_i)\Delta t + \begin{bmatrix} \dot{u}(t_i) \\ u(t_i) \end{bmatrix} \tag{5.30}$$

In the above, the actual control signal $u(t_i)$ is computed using the optimal signal $u_s(t_i)$ and the previous states of control $\dot{u}(t_{i-1})$ and $u(t_{i-1})$.

Remark 5.2.1 *It is also possible that by tuning the Q and R weighting matrices in the cost function to reduce the sensitivity towards the frequency variation. However, an obvious advantage of the proposed scheme is that it provides a systematic way of designing a predictive controller to improve the robustness.*

5.2.1 Constrained Control

As we have shown previously, it is important to limit the amplitude of the switching input S_α and S_β to be within a linear region as shown in Figure. In order to constrain the control input in MPRC, linear inequalities in terms of control input u is included in the cost function, where from (5.30), we can express $\dot{u}(t)$ and

$u(t)$ as function of the parameter vector η ($u_s(t) = L(0)^T\eta$)

$$\dot{u}(t_i) = \overbrace{-\omega_0^2 u(t_i - 1)\Delta t + \dot{u}(t_i - 1)}^{c1} - Kx(t_i)\Delta t + L(0)^T\eta\Delta t \tag{5.31}$$

$$\begin{aligned} u(t_i) &= \dot{u}(t_i)\Delta t + u(t_i - 1) \\ &= \overbrace{-\omega_0^2 u(t_i - 1)\Delta^2 t + \dot{u}(t_i - 1)\Delta t + u(t_i - 1)}^{c2} - Kx(t_i)\Delta t + L(0)^T\eta\Delta t \end{aligned} \tag{5.32}$$

Given that the switching function constraints are bounded by the following hard constraints,

$$u_{min} \leq u(t_i) \leq u_{max} \tag{5.33}$$

where $u(t_i) = [S_\alpha(t_i) \;\; S_\beta(t_i)]$, u_{min} and u_{max} are the corresponding switching input limits.

The constraint on the control input $u(t)$ are then expressed as

$$L(0)^T\Delta t^2\eta \leq u_{max} - c2 - Kx(t_i)\Delta t \tag{5.34}$$

$$-L(0)^T\Delta t^2\eta \leq -u_{min} + c2 - Kx(t_i)\Delta t \tag{5.35}$$

With the operational constraints specified, the predictive control problem with hard constraints imposed in the design becomes the problem of finding the optimal solution of the quadratic cost function

$$\begin{aligned} \underset{\eta}{\text{minimize}} \quad & J = \eta^T\Omega\eta + 2\eta^T\Psi x(t_i) \\ \text{subject to} \quad & \begin{bmatrix} L(0)^T\Delta t^2 \\ L(0)^T\Delta t^2 \end{bmatrix}\eta \leq \begin{bmatrix} u_{max} - c2 - Kx(t_i)\Delta t \\ -u_{min} + c2 - Kx(t_i)\Delta t \end{bmatrix} \end{aligned} \tag{5.36}$$

In this work, primal-dual method of Hildreth's Quadratic Programming algorithm is chosen to provide the numerical solution to the above constrained

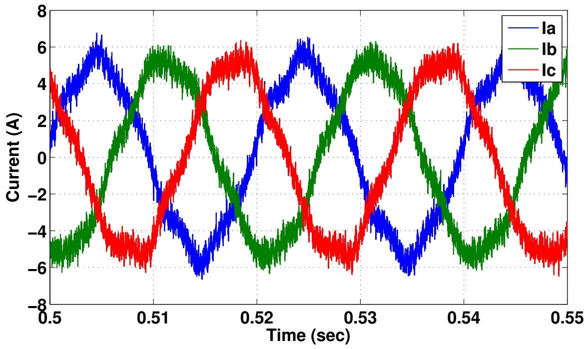

Figure 5.2: Distorted three-phase currents due to distorted grid voltage.

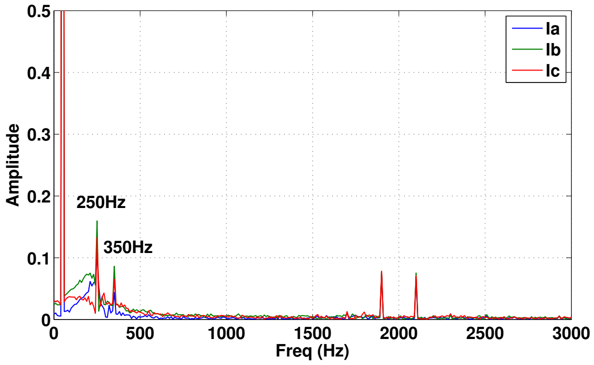

Figure 5.3: Frequency spectrum of three-phase current showing 5^{th} (250Hz) and 7^{th} (350Hz) harmonics due to the distorted grid voltage.

optimal problem [109]

5.3 MPRC with Selective Harmonic Compensation

So far we have assumed the condition of grid voltage to be stable, balanced and non-distorted. However, due to faults, resonances and overloads etc. the actual grid voltage condition varies which may give rise to uncontrolled oscillations in the active and reactive power delivered to the network. In three phase systems, the main grid voltage harmonic distortion appears in 5^{th} and 7^{th} harmonics of the grid frequency and the grid voltage harmonics influence the current controller and generate current harmonics [65],[96]. Figure 5.2 shows the effect of distorted grid voltage on the closed-loop response of grid current based on MPRC of the previous section. Figure 5.3 is the frequency spectrum of the corresponding distorted grid current. As it can be seen from both figures that a single MPRC tuned at one frequency is not sufficient to compensate the grid voltage distortion on the current, which indicates that the bandwidth of MPRC needs to be extended to cover the frequencies of 5^{th} and 7^{th} harmonics.

In this section, the design of MPRC is extended in the stationary reference frame to include a 'plug-in' resonant harmonic compensator which is able to null the harmonic at a specific frequency. The overall control structure shown in Figure 5.4 which mainly consists of nominal and disturbance rejection controller. The nominal control part in this case is the MPRC tuned at the grid frequency which controls the i_α and i_β currents to follow the desired reference inputs based on the on-line constrained optimizations problem. Under the nominal switching inputs and in the absence of disturbances, the trajectories of i_α and i_β currents are designed to follow the closed-loop response of this nominal controller. In order to ensure the stability and optimality in the presence of grid voltage disturbances, a feedback disturbance rejection control is used to keep the actual state of i_α and i_β currents close to the nominal state trajectories based on the error between the actual system state and nominal state. Mathematically, the proposed scheme in the figure can be represented as follows

$$u(t) = \bar{u}(t) + K_{h5}(x(t) - \bar{x}(t)) + K_{h7}(x(t) - \bar{x}(t)) \tag{5.37}$$

where $\bar{u}(t)$ is the nominal control input from the MPRC, $\bar{x}(t) = [i_{\alpha}^{-} \;\; i_{\beta}^{-}]^T$ is the nominal current trajectories and the disturbance rejection term of K_{h5} and K_{h7}

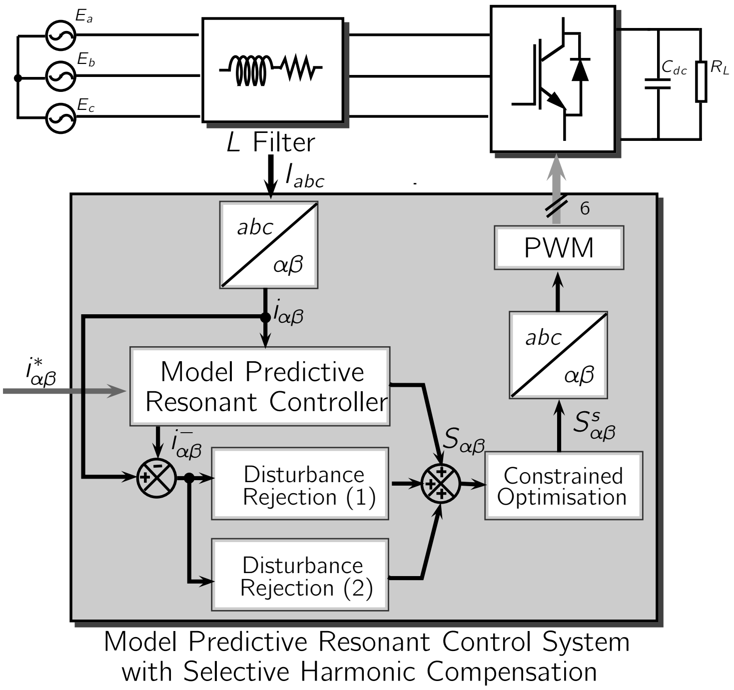

Figure 5.4: Overview of the MPRC with selective harmonic compensations: Disturbance rejection part corresponds to the 5^{th} and 7^{th} harmonic compensations. $i^*_{\alpha\beta}$ and $i^-_{\alpha\beta}$ indicates the reference current inputs and the nominal trajectory respectively. The $S_{\alpha\beta}$ corresponds to the combined control inputs and $S^s_{\alpha\beta}$ is the constrained control input.

belong to disturbance rejection components which are designed to reject the 5^{th} and 7^{th} harmonics in the grid current respectively.

The following section discusses the detailed design of model-based selective harmonic compensator, K_{h5} and K_{h7}.

5.3.1 Model-based Selective Harmonic Compensator

Based on the internal model principle, in order to reject 5^{th} and 7^{th} harmonics the following augmented model of the converter is considered in the stationary-reference frame

$$\begin{bmatrix} \frac{dz(t)}{dt} \\ \frac{d^2y(t)}{dt^2} \\ \frac{dy(t)}{dt} \end{bmatrix} = \overbrace{\begin{bmatrix} A_m & 0_2 & 0_2 \\ C_m & 0_2 & -\omega^2_{h5,7} I_2 \\ 0_2 & I_2 & 0_2 \end{bmatrix}}^{A_{h5,7}} \begin{bmatrix} z(t) \\ \frac{dy(t)}{dt} \\ y(t) \end{bmatrix} + \overbrace{\begin{bmatrix} B_m \\ 0_2 \\ 0_2 \end{bmatrix}}^{B_{h5,7}} u_{s_{5,7}}(t) \tag{5.38}$$

where ω_{h_5} and ω_{h_7} are the targeted harmonic frequency of 250 Hz and 750 Hz respectively. In fact the augmented model in (5.38) is the same as in (5.13) except the frequency of embedded resonant module.

From the above model, the harmonic compensator is designed to find a control law (i.e. $u(t) = K_{5,7}x(t)$) that minimise the following cost function.

$$J = \int_0^\infty e(t)^T Q e(t) + u^T_{s_{5,7}}(t) R u_{s_{5,7}}(t) \tag{5.39}$$

where

$$e(t) = \begin{bmatrix} \bar{x}'(t) - x(t) \\ \bar{x}(t) - x(t) \end{bmatrix} \tag{5.40}$$

$x(t) = [i_\alpha \;\; i_\beta]^T$ is the measured current in the stationary frame. $\bar{x}(t) = [i_\alpha^- \;\; i_\beta^-]^T$ and $\bar{x}'(t)$ are the nominal and derivative of the nominal stationary frame current trajectory respectively. $Q \geq 0$ and $R > 0$ are symmetric matrices which are used to set the optimal performance of each compensator.

Whilst the stability of each compensator is guaranteed by the above LQR design, we are further interested in imposing a stability condition on the overall system in Figure 5.4 which includes each harmonic compensator as well as the unconstrained control law used in the nominal MPRC.

The main motivation here is based on the fact that the closed-loop stability of the overall system can be considered by taking a similar approach as in the Piecewise Affine (PWA) systems stability analysis (see [30] for the analysis of the PWA systems), where we look for the common matrix P (i.e. terminal weighting matrix) and K_i (state feedback law) that satisfy the condition below,

$$\begin{cases} P > 0, \\ (A_i + B_i K_i)^T P + P(A_i + B_i K_i) < 0 \end{cases} \tag{5.41}$$

Based on the above condition, we find a quadratic Lyapunov function $V(x) = x^T P x, P > 0$ that bounds the cost function such that

$$\frac{d}{dt} V(x) \leq -x^T \left(Q + K_i^T R K_i \right) x, \quad i = 1, 5, 7 \tag{5.42}$$

where K_5 and K_7 are the state feedback control law for 5^{th} and 7^{th} harmonic compensator respectively. The state feedback control law of K_1 corresponds to an unconstrained control law in MPRC as

$$\dot{u}(t) = -K_1 x(t) + \dot{v}(t) \tag{5.43}$$

where K_1 is designed based on the same cost function as in (5.39), and as we described in section 3.4, this controller also acts as a terminal cost controller to guarantee the stability of the MPRC.

To see how the condition on (5.42) sets the bound on the cost function of (5.39), let us consider for some $P = P^T > 0$, we can derive

$$\frac{d}{dt} V(x) = \frac{d}{dt} (x_t^T P x_t) \leq -x^T \left(Q + K_i^T R K_i \right) x \, dt \tag{5.44}$$

based on the second method of Lyapunov stability. Integrating this inequality from $t = 0$ to $t = t_f$, (5.44) becomes

$$x_{t_f}^T P x_{t_f} - x_0^T P x_0 \leq - \int_0^T x^T \left(Q + K_i^T R K_i \right) x \, dt \tag{5.45}$$

Since we know that $x_{t_f}^T P x_{t_f} \geq 0$ which holds for $t \rightarrow \infty$, we have

$$\int_0^{\infty} x^T \left(Q + K_i^T R K_i \right) x \, dt \leq x_0^T P x_0 \tag{5.46}$$

thus by finding a suitable matrix P the cost function can be bounded.

To find the terminal weighting P matrix and the corresponding state feedback control laws in (5.42), the above LQR problem is formulated using the following matrix inequalities, [22]

$$\begin{cases} P > 0, \\ x^T \left((A_i + B_i K_i)^T P + P(A_i + B_i K_i) \right) x < -x^T \left(Q + K_i^T R K_i \right) x \end{cases} \tag{5.47}$$

Furthermore, we impose an upper bound ($\gamma > 0$) on $x^T P x \geq 0$ such that

$$x^T P x \leq \gamma \tag{5.48}$$

For obvious reasons it is useful to transform the nonlinear matrix inequality (5.47) into an LMI. To do that, we employ the Schur complements based technique (see Appendix) [22].

$$\begin{bmatrix} (A_i + B_i K_i)^T P + P(A_i + B_i K_i) & K_i^T & I \\ K_i & -R^{-1} & 0 \\ I & 0 & -Q^{-1} \end{bmatrix} \geq 0 \tag{5.49}$$

Also for the inequality in (5.48)

$$\gamma - x^T (P^{-1})^{-1} x \geq 0 \tag{5.50}$$

$$\begin{bmatrix} \gamma & x^T \\ x & P^{-1} \end{bmatrix} \geq 0 \tag{5.51}$$

Pre and post multiplying (5.49) by $diag[P^{-1}, I, I]$ and consider the variables $X = P^{-1}$ and $Y_i = K_i P^{-1}$ and we obtain the following LMIs

$$\begin{bmatrix} A_iX + XA_i^T + BY + Y_i^T B^T & Y_i^T & X \\ Y_i & -R^{-1} & 0 \\ X & 0 & -Q^{-1} \end{bmatrix} \geq 0 \tag{5.52}$$

$$\begin{bmatrix} \gamma & x^T \\ x & X \end{bmatrix} \geq 0 \tag{5.53}$$

$$X > 0 \tag{5.54}$$

The problem is summarized to

$$\text{minimise} \quad \gamma \tag{5.55}$$

$$\text{subject to} \quad \begin{bmatrix} A_iX + XA_i^T + BY_i + Y_i^T B^T & Y_i^T & X \\ Y_i & -R^{-1} & 0 \\ X & 0 & -Q^{-1} \end{bmatrix} \geq 0 \tag{5.56}$$

$$\begin{bmatrix} \gamma & x^T \\ x & X \end{bmatrix} \geq 0 \tag{5.57}$$

$$X > 0 \tag{5.58}$$

Therefore, if the LMI (5.55) is feasible then the terminal weight and the feedback gains are recovered as $P = X^{-1}$ and $K_i = Y_i P^{-1}$ and it directly follows that the function $V(x) = x^T P x$ is a common quadratic Lyapunov function which ensures that the closed-loop system is asymptotically stable on some region of attraction, e.g., the level set given by the $\gamma > 0$.

Based on the state feedback found from the above LMI, and using the similar approximation as in (5.30), the control signals of each harmonic compensator can be computed as follows

$$\begin{bmatrix} \dot{u}_{h_{5,7}}(t_i) \\ u_{h_{5,7}}(t_i) \end{bmatrix} = \begin{bmatrix} 0 & -\omega_{h_{5,7}}^2 I_2 \\ I_2 & 0 \end{bmatrix} \begin{bmatrix} \dot{u}_{h_{5,7}}(t_i) \\ u_{h_{5,7}}(t_i) \end{bmatrix} \Delta t \quad + \begin{bmatrix} I_2 \\ 0 \end{bmatrix} u_{s_{5,7}}(t_i)\Delta t + \begin{bmatrix} \dot{u}_{h_{5,7}}(t_{i-1}) \\ u_{h_{5,7}}(t_{i-1}) \end{bmatrix} \tag{5.59}$$

where $u_{s_5}(t_i) = -K_{h_5}e(t_i)$ and $u_{s_7}(t_i) = -K_{h_7}e(t_i)$ are respectively. Finally, the control input with harmonic compensator is given as

$$u(t_i) = \bar{u}(t_i) + u_{h_5}(t_i) + u_{h_7}(t_i) \tag{5.60}$$

5.3.2 Constrained Control

The formulation of constraints on the control input follows the similar process as in the previous section, except that there are now disturbance rejection control inputs for rejecting 5^{th} and 7^{th} harmonics.

As it was defined in (5.60), the actual control input to the VSC can be formulated as follows

$$u_H(t_i) = u(t_i) + u_{h_5}(t_i) + u_{h_7}(t_i) \tag{5.61}$$

where the disturbance control inputs $u_{h_5}(t)$ and $u_{h_7}(t)$ are given in (5.59) and the constrained MPRC control input of $u(t)$ in terms of parameter vector η is given as

$$\begin{aligned} u(t_i) &= \dot{u}(t_i)\Delta t + u(t_i - 1) \qquad (5.62) \\ &= \overbrace{-\omega_0^2 u(t_i - 1)\Delta^2 t + \dot{u}(t_i - 1)\Delta t + u(t_i - 1)}^{c2} + L(0)^T \eta \Delta t \end{aligned}$$

Here, the switching function constraint are bounded by the following hard constraints,

$$u_{min} \leq u_H(t_i) \leq u_{max} \tag{5.63}$$

where $u_{min} = [S_\alpha^{min} \;\; S_\beta^{min}]^T$ and $u_{max} = [S_\alpha^{max} \;\; S_\beta^{max}]^T$ are the minimum and maximum switching inputs in the stationary reference frame respectively.

Based on (5.61) and (5.62), the constraints on the control input $u(t)$ are then expressed as

$$L(0)^T \Delta t^2 \eta \leq u_{max} - c2 - u_{h_5}(t_i) - u_{h_7}(t_i) \tag{5.64}$$

$$-L(0)^T \Delta t^2 \eta \leq -u_{min} + c2 + u_{h_5}(t_i) + u_{h_7}(t_i) \tag{5.65}$$

It immediately follows that when there are no disturbance (i.e. $u_{h_5}(t) = 0$ and $u_{h_7}(t) = 0$) the above constraints are exactly same as in (5.34). But in the case of grid disturbances, the original input constraints are reduced by the amount of control input required for the disturbance rejection, which ensures that the original input constraint in (5.63) is still satisfied (i.e. feasibility). In terms of control performance, this also implies that if there is a large disturbances in the system the available nominal control input of MPRC is consequently limited, hence affects the tracking performance of the nominal system, whereas if there is only a small or no disturbance, the tracking performance is mainly determined by the nominal MPRC.

With the operational constraints specified, the following quadratic cost function is used to find the constrained optimal input of the MPRC:

$$\begin{aligned} \underset{\eta}{\text{minimize}} \quad & J = \eta^T \Omega \eta + 2\eta^T \Psi x(t_i) \\ \text{subject to} \quad & \begin{bmatrix} L(0)^T \Delta t^2 \\ L(0)^T \Delta t^2 \end{bmatrix} \eta \leq \begin{bmatrix} u_{max} - c2 - u_{h_5}(t_i) - u_{h_7}(t_i) \\ -u_{min} + c2 + u_{h_5}(t_i) + u_{h_7}(t_i) \end{bmatrix} \end{aligned} \tag{5.66}$$

5.4 Experimental Result

The experimental validation of MPRC is performed using the laboratory set-up as described in Appendix, where the proposed MPRC is controlled digitally using xPC target. The system parameters used in the experimental set-up are shown in Table. 5.1.

Table 5.1: Grid-connected VSC system parameters

Symbol	Parameter Name	Value	Unit
V_{grid}	Grid Voltage	30	V
f_{grid}	Grid Frequency	50	Hz
L_s	Input Filter Inductance	8.9	mH
R_L	Input Filter ESR	8.3	Ω
C_{dc}	DC-link Capacitance	700	μF
R_{dc}	Load Resistance	$20-40$	Ω

5.4.1 Model Predictive Resonant Control

An experimental validation of the MPRC is conducted for rectification and regeneration modes. In the rectification mode, the converter draws the current from the main grid to maintain a boosted DC bus voltage. In order to simulate the rectification mode, a resistive load (R_{dc}) is connected to the DC bus and the reference values of i_α and i_β are chosen to maintain a constant DC bus voltage. Figure 5.5 shows good tracking responses of i_α and i_β to its reference inputs in steady-state, as well as its transient response to a step change in reference inputs from 5 A_{peak} to 8 A_{peak} at 1 sec. Figure 5.6 and 5.7 show the measured control inputs of S_α and S_β respectively, where the dotted-line indicates the corresponding saturation limit for each input. A box constraint for control inputs similar to the one in Section can also be used here, however by employing the sinusoidally varying constraints respect to the control input, we can also limit

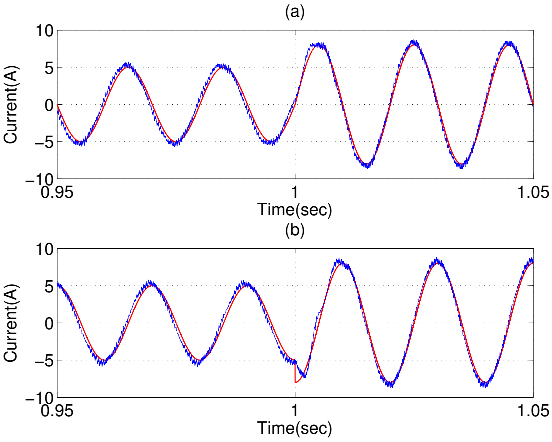

Figure 5.5: The measured response of I_α currents (a) and I_β currents (b) in rectification mode: a step change of the reference current inputs (red) occurs at 1 sec.

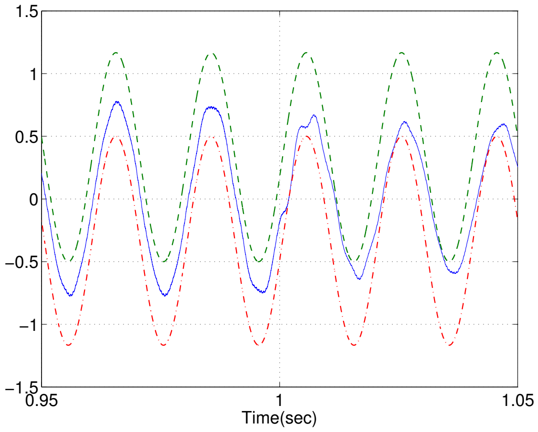

Figure 5.6: The measured response of control input (S_α) in rectification mode: the dotted line is the corresponding control saturation limit.

the slew-rate on the control input at the same time. As it can be seen from both figures that input constraints are satisfied during the step change in reference inputs from 5 A_{peak} to 8 A_{peak} at 1 sec. Figure 5.8 is the plot of grid current in the α-β axis respectively.

The proposed MPRC is also tested in the regeneration mode, where the mode is triggered by the over-voltage in the DC bus. In order to simulate this mode, the converter is first placed in the rectification mode to control the DC

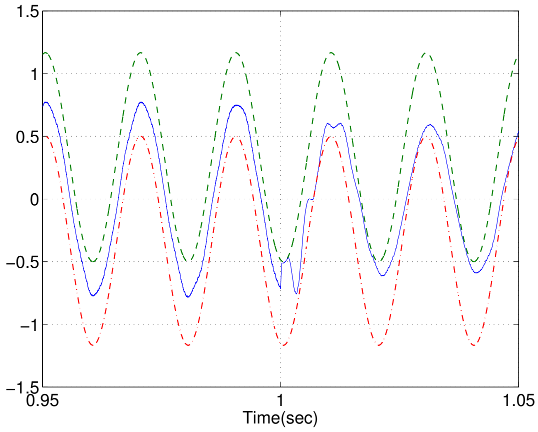

Figure 5.7: The measured response of control input (S_β) in rectification mode: the dotted line is the corresponding control saturation limit.

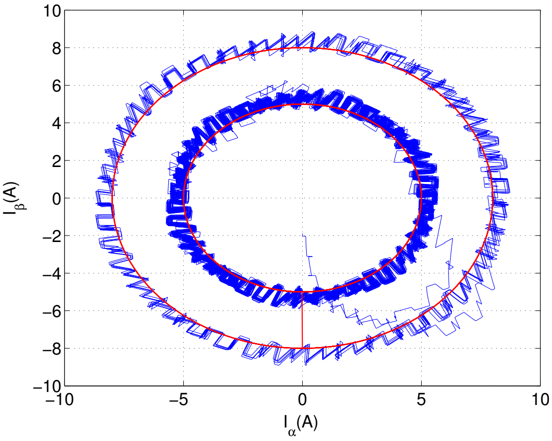

Figure 5.8: The measured response of grid current with reference inputs (red) in the stationary reference frame axis (α-β axis): rectification mode.

bus voltage to a desired level. After that an over-voltage in the DC bus voltage is caused by an external source, which in turn changed the reference inputs of i_α and i_β to re-direct the input current from the DC-bus to the main grid. Figures 5.9 and 5.10 show responses of i_α,i_β currents obtained from the experimental data which illustrates a good transient response, when the mode is switched from the rectification to regeneration mode at 2 sec. Moreover, as shown in 5.11 and 5.12 when the mode transition occurs at 2 sec, the switching control inputs of S_α and S_β are constrained within the saturation limit, and as we mentioned the

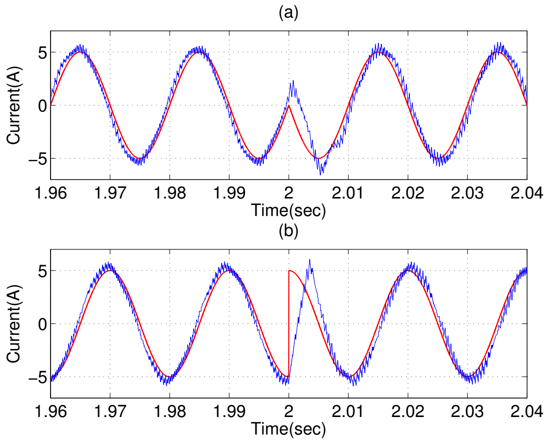

Figure 5.9: The measured response of I_α currents (a) and I_β currents (b) in regeneration mode: a step change of the reference current inputs (red) due to mode change occurs at 2 sec.

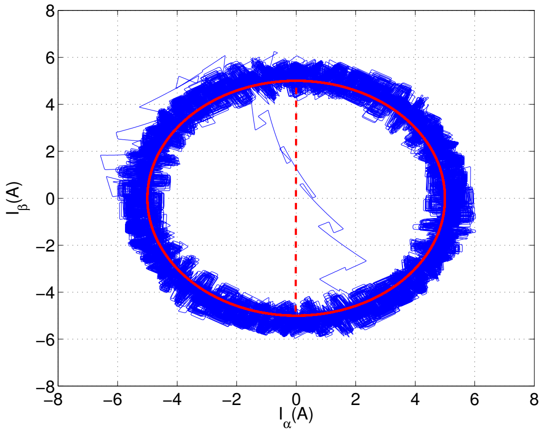

Figure 5.10: The measured response of grid current with reference inputs (red) in the stationary reference frame axis (α-β axis): regeneration mode.

slew-rate of switching inputs are limited at the same time.

MPRC under Grid Frequency Variation

Due to the well-regulated main grid, an arbitrary variation of the actual grid frequency as large as $\pm 5Hz$ was not possible to achieve in the laboratory set up used in this work. Therefore, in order to validate the method proposed, a numerical simulation model based on Simulink's Simpowersystems toolbox

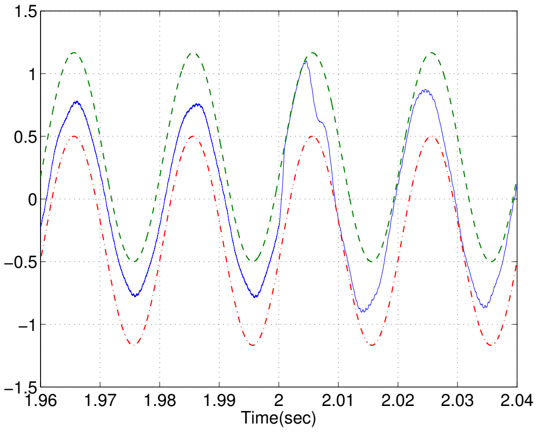

Figure 5.11: The measured response of control input (S_α) in regeneration mode: the dotted line is the corresponding control saturation limit.

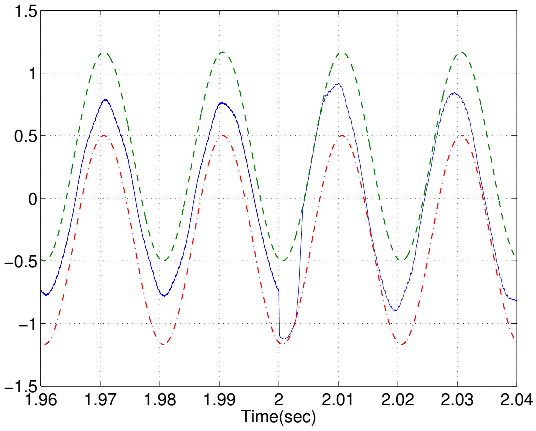

Figure 5.12: The measured response of control input (S_β) in regeneration mode: the dotted line is the corresponding control saturation limit.

is used. The dynamic representation of the simulation model is same as the actual system and the same parameters as shown in Table 5.1 is used. The clear advantage of using the simulation in this case is that the grid fault such as frequency variation can now be inserted artificially.

To validate the robust MPRC in, a step change in the grid frequency of $\pm 5Hz$ is first injected at around 0.72 sec. Clearly this is simulating the worst-case scenario since it is highly unlikely that the actual grid frequency varies in a step manner with such a large magnitude. Figure. 5.13 shows the response of phase

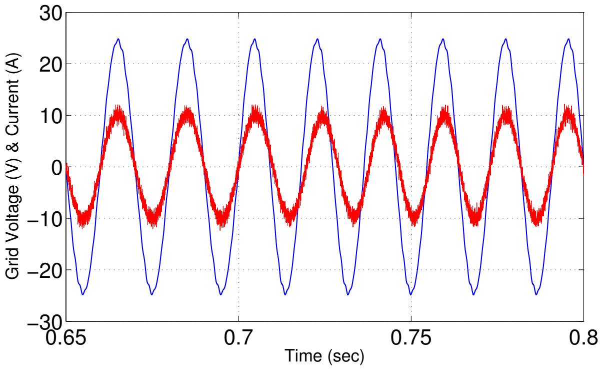

Figure 5.13: The simulated response of a grid voltage V_a (blue) and current I_a (red) under a step change of grid frequency from $50Hz$ to $55Hz$ at 0.72 sec.

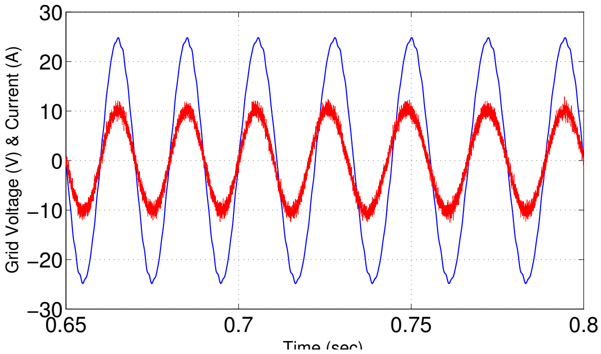

Figure 5.14: The simulated response of a grid voltage V_a (blue) and current I_a (red) under a step change of grid frequency from $50Hz$ to $45Hz$ at 0.72 sec.

current based on robust MPRC, when the grid frequency is step changed from $50Hz$ to $55Hz$. It can be seen that the phase current are well tracked despite a large change in the grid frequency. Figure. 5.14 is the response of the phase current when a step change in the grid frequency from $50Hz$ to $45Hz$. Again the response of the phase current adapts well to the change in grid frequency. As shown in Table, the response time is well within the specified regulation. Figure. 5.15 shows the response of phase current for the grid frequency variation of $1Hz$, which has no transient effect of the phase current.

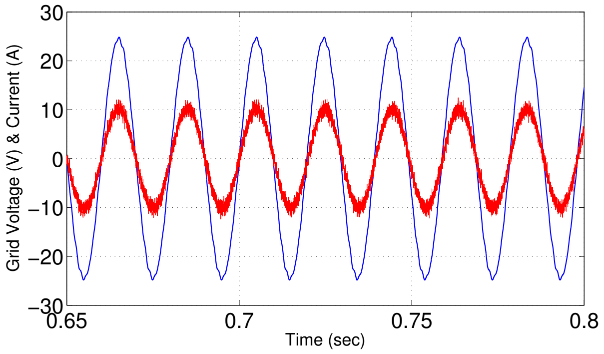

Figure 5.15: The simulated response of a grid voltage V_a (blue) and current I_a (red) under a step change of grid frequency from $50Hz$ to $51Hz$ at 0.72 sec.

5.4.2 MPRC with Selective Harmonic Compensations

Based on the same system parameter, the experimental validation of the control scheme proposed in section 5.3 is carried out by simulating the grid voltage distortions. The following control gains are used for each harmonic compensator:

$$K_5 = \begin{bmatrix} -0.09 & 0 & 1.97e-06 & 0 & 2.79e-07 & 0 & -0.03 & 0 \\ 0 & -0.09 & 0 & 1.97e-06 & 0 & 2.79e-07 & 0 & -0.03 \end{bmatrix} \tag{5.67}$$

$$K_7 = \begin{bmatrix} -0.79 & 0 & -1.68e-06 & 0 & 3.67e-06 & 0 & -0.03 & 0 \\ 0 & -0.79 & 0 & -1.68e-06 & 0 & 3.67e-06 & 0 & -0.03 \end{bmatrix} \tag{5.68}$$

Figure 5.16 and 5.17 first show the distorted three phase grid current due to grid voltage distortion and its frequency spectrum. Figure 5.18 shows the response of i_α and i_β current and the nominal closed-loop current trajectories. As it can be seen that the measured currents of i_α and i_β are distorted compared to the desired nominal current trajectories.

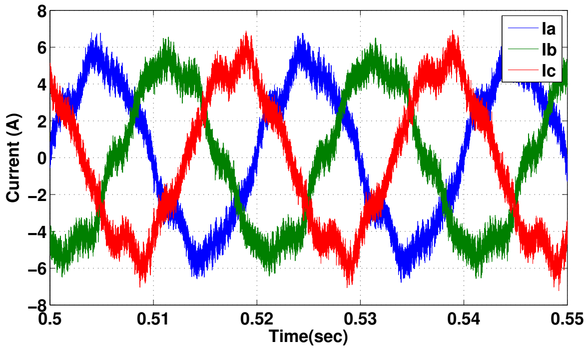

Figure 5.16: The distorted three-phase current due to grid voltage harmonics

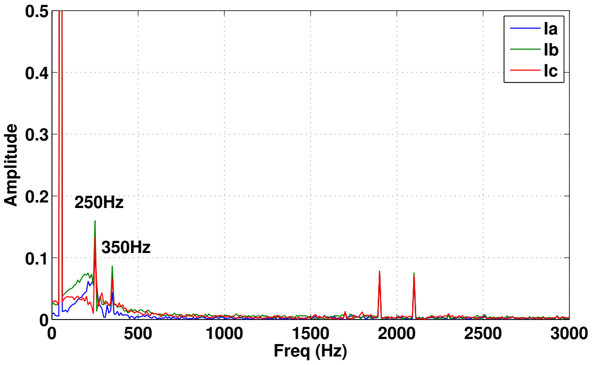

Figure 5.17: The frequency spectrum of the distorted three-phase current due to grid voltage harmonics

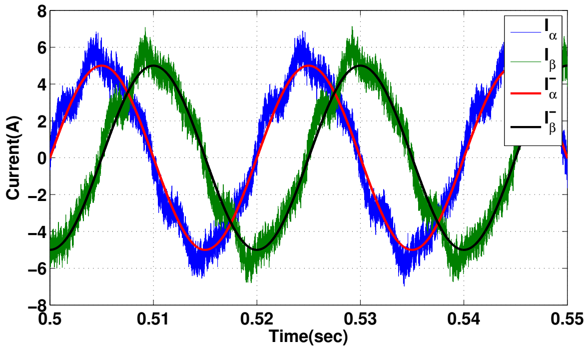

Figure 5.18: The measured response of the i_α (blue) and i_β (green) current and the corresponding nominal trajectories of i_α (red) and i_β (black) current.

In order to reduce the harmonics in the grid current, the selective harmonic compensation scheme is applied to eliminate the 5^{th} and 7^{th} harmonics in the grid current.

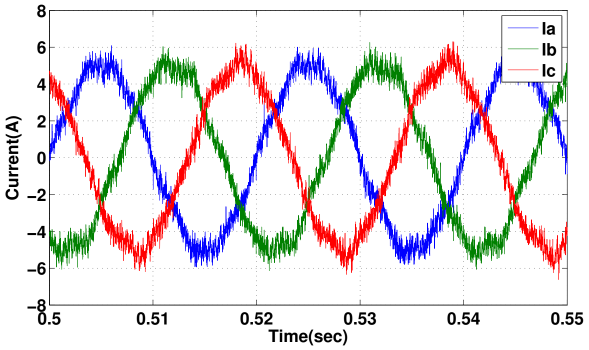

Figure 5.19: The measured response of three-phase current after applying the 5^{th} harmonic compensation.

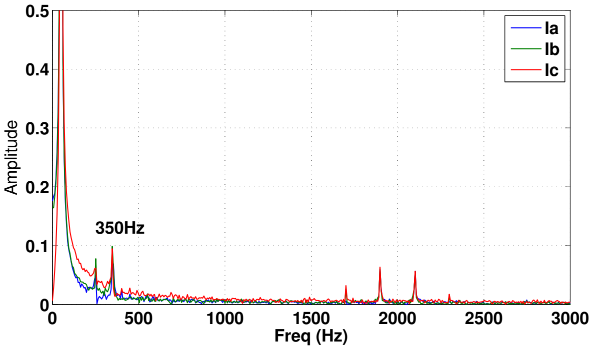

Figure 5.20: The frequency spectrum of three-phase current after applying the 5^{th} harmonic compensation.

To illustrate the efficacy of the selective harmonic compensation, a validation is first carried out to eliminate the 5^{th} harmonic in the current. As shown in the frequency spectrum of the grid current in Figure 5.20, the magnitude of the 5^{th} harmonic is reduced significantly and consequently the three-phase current and i_α and i_β current shown in Figure 5.19 and 5.21 are less distorted than the one shown in Figure 5.16.

Now to reduce the 5^{th} and 7^{th} harmonics in the grid current, the selective harmonic compensation of both harmonics is applied. Figures 5.22,5.23 and 5.24 show the the significant reduction in both harmonics after applying the 5^{th} and 7^{th} harmonics compensation along with the main MPRC.

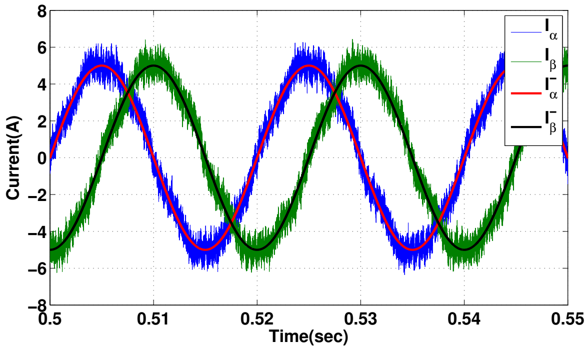

Figure 5.21: The measured response of the i_α (blue) and i_β (green) current and the corresponding nominal trajectories of i_α (red) and i_β (black) current after applying the 5^{th} harmonic compensation.

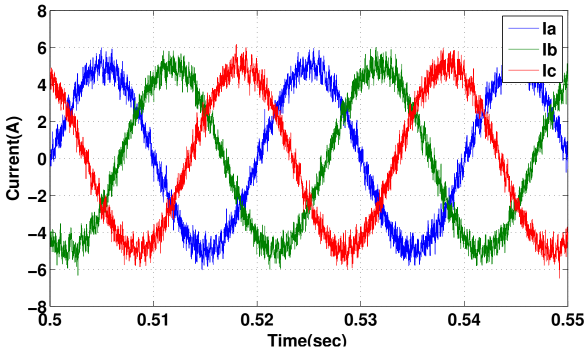

Figure 5.22: The measured response of three-phase current after applying the 5^{th} and 7^{th} harmonic compensation.

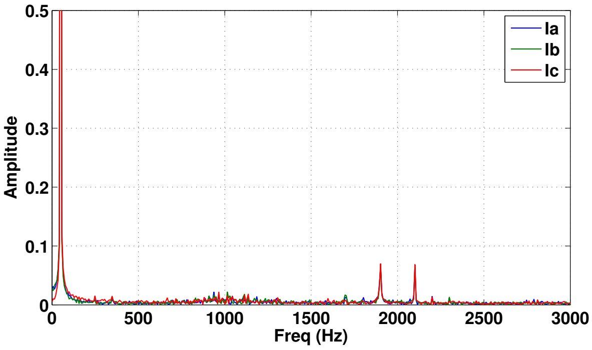

Figure 5.23: The frequency spectrum of three-phase current after applying the 5^{th} and 7^{th} harmonic compensation.

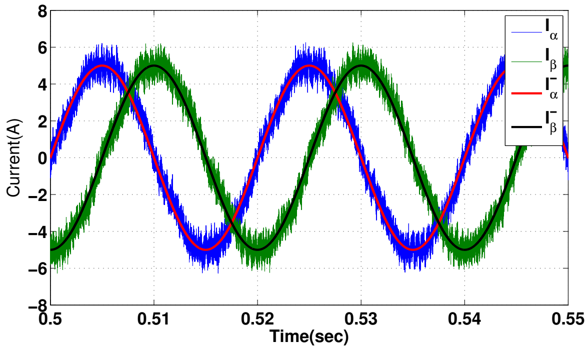

Figure 5.24: The measured response of the i_α (blue) and i_β (green) current and the corresponding nominal trajectories of i_α (red) and i_β (black) current after applying the 5^{th} and 7^{th} harmonic compensation.

5.5 Conclusions

This chapter presented a model predictive resonant control (MPRC) scheme for controlling the grid current in the stationary frame. The main idea of the presented method was to embed a sinusoidal resonant module in the system model to follow the sinusoidally varying current reference inputs. Following from the description of the augmented model, a practical problem regarding grid frequency variations was considered. For this problem, we have proposed a robustly stabilising feedback law and introduced it into the design of MPRC by using the concept of closed-loop paradigm approach. For another commonly encountered problem in the grid-connected VSC, problems of multiple harmonic distortions on the grid current caused by grid voltage harmonics were investigated and it presented a control solution that eliminates unwanted harmonics while preserving the stability of the overall control system. All of the presented methods were experimentally validated and showed a satisfactory performance.

CHAPTER 6

Predictive Current Control with Finite Control Set

6.1 Introduction

So far in this work, the switching control signals are converted to discretised switching signals through a PWM module which allowed the converter output voltage to be linearly controlled by the applied voltage inputs. However, to implement the control strategies using the PWM, an extra computational load and a specialised hardware are required to generate the correct PWM pulses and controller timings.

In a bid to simplify the implementation and to enhance the lack of flexibility in the PWM based control method, a cost function based switching technique known as finite control set model predictive control (FCS-MPC) is considered in this chapter. In section 6.2, based on a generic framework of FCS-MPC, we propose a FCS-MPC scheme that handles the system constraints on-line while minimising the cost funtion based on a one-step ahead prediction. In section 6.3, an application of FCS-MPC to a grid connected VSC is explained based on the proposed scheme in section 6.2. To close the chapter, experimental results are presented in the last section.

6.2 FCS-MPC with Constraints

The main concept of a finite control set MPC approach is to use a discrete time model of VSC to predict the future behaviour of the grid current at each sampling instant. Based on the model prediction, a cost function is generally evaluated by exploring the combination of finite number of switching states over a finite horizon [100], For instance, the following cost function is often used to compute the optimal switching input.

$$J_i = |i^*_{dq} - i^P_{dq}(S_i)| + |i^*_{dq} - i^P_{dq}(S_i)| \quad \text{FOR I} = 0..7 \tag{6.1}$$

where $i^P_{dq}(S_i)$ is the prediction of current trajectories for each switching vector in the synchronous reference frame which can be calculated as

$$i_d(k+1) = i_d(k) + \frac{\Delta t}{L_s}(-Ri_d(k) + \omega L_s i_q(k) + e_d(k) - v_d(S_i)) \tag{6.2}$$

$$i_q(k+1) = i_q(k) + \frac{\Delta t}{L_s}(-v_q(S_i) - Ri_q(k) - \omega L_s i_d(k)) \tag{6.3}$$

In three-phase VSC case, there are eight possible switching inputs. Naturally by taking the all of eight possible switching inputs, evaluation of the cost function leads to eight different costs and the control action with the minimum cost is applied in the next sampling instant.

One of the concerned point for FCS-MPC, in particular with the above cost function in (6.1) is the lack of guaranteed stability in the formulation [8]. This issue stems from the fact that the cost function in (6.1) only penalises deviation of state trajectories from the reference inputs, and there is no proper weighting term or the terminal constraint to impose the stability. Furthermore, for a finite control set system, the asymptotic stability becomes too strong requirement, since the state trajectory does not converge and tend to oscillate around the

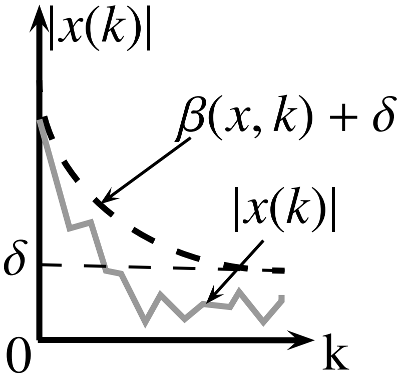

Figure 6.1: The concept of practical stability: The system is said to be practically stable if there exists a positive constant δ, and a function $\beta(|x|,k)$, which is monotonically decreasing in k and monotonically increasing in $|x|$, such that $|x| \leq \beta(|x|,k)+\delta$ [17],[9]

origin or the desired system reference [17],[9],[11], which makes even harder to establish the guaranteed stability condition. In the recent work by [8], the stability problem of FCS-MPC is analysed by first considering the error due to approximation of nominal inputs with finite control set (i.e. quantisation error), as bounded state disturbances. Based on this observation, the stability problem of FCS-MPC, is then considered using the concept of practical stability, where the term practical is used to differentiate from the asymptotic stability to emphasise a condition of stability in the neighbourhood of the origin, which can be illustrated intuitively as shown in Figure 6.1. To satisfy the practical stability, they proposed to redesign the cost function of (6.1) according to the following theorem.

Theorem 6.2.1 *Let* $\mathcal{D}_{\delta_N} = \{x \in \mathbb{X}_{\mho} : |x| \leq \delta_N\}$ *be a neighbourhood of the origin,* *where*

$$\delta_N^2 = \left(\frac{1 + (1-\rho)N}{\lambda_{min}(Q)(1-\rho)}\right)|W|\Delta_q^2 \tag{6.4}$$

in which $\rho = 1 - \frac{\lambda_{min}(Q)}{\lambda_{max}(P)} \in (0, 1)$. *If the cost function is designed such that the terminal cost satisfies that*

- *The matrix P is the solution to the following ARE*

$$A_K^T P A_K - P + Q^* = 0, \quad Q^* = Q + K^T R K \tag{6.5}$$

  where $A_k = A - BK$.

- *There exists a local controller* $k_f(x)$ *which satisfies the following condition in the terminal region*

$$V_f(f(x, k_f(x))) - V_f(x) + \ell(x, k_f(x)) < \gamma \tag{6.6}$$

  for all $x \in \mathbb{X}_f$ *and some* $\gamma \geq 0$.

then FCS-MPC is Practically Asymptotically Stable

The detailed proof of this theorem can be found in [93],[8]. The main essence of the above theorem is to consider the cost function of FCS-MPC as a candidate Lyapunov function and design the terminal cost based on Algebraic Riccati Equation (ARE). Hence the associated terminal region $\mathbb{X}_f$ is first defined based on a continuous (convex) control set and a local controller $k_f(x)$ is found to characterise an ultimately bounded set $\mathcal{D}_{\delta_N}$ by considering the quantisation error as a bounded disturbance. This idea stems from a widely known technique in establishing the stability of MPC which is to use a fixed stabilising controller for the terminal region $\mathbb{X}_f$ [93]. In this case, the ultimately bounded set $\mathcal{D}_{\delta_N}$

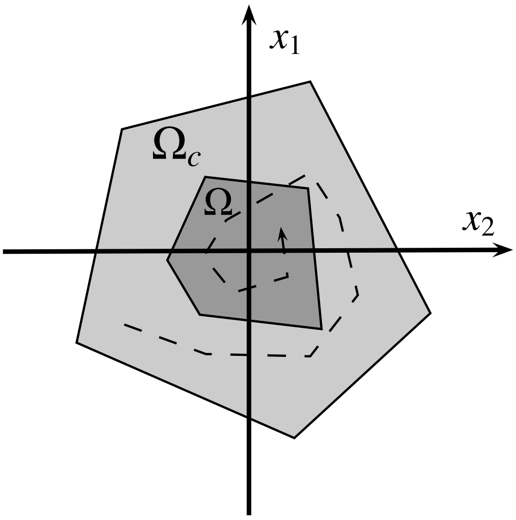

Figure 6.2: The concept of proposed FCS-MPC: the initial state inside the Ω_c (feasibility) is steered into the invariant set Ω in finite steps to guarantee the stability.

represents a terminal region for a local controller $k_f(x)$ with a bounded disturbance. Furthermore, it is shown in [8] that this ultimate bounded set is subset of the terminal region $\mathcal{D}_{\delta_N} \subseteq \mathbb{X}_f$ to guarantee a sufficient stability condition. Based on the above stability analysis result, a FCS-MPC scheme is proposed in this section to handle system constraints in the on-line optimization problem to guarantee the stability and feasibility of FCS-MPC.

As illustrated in Figure 6.2, the main objective of the proposed scheme is to control the system state in side Ω_c, which is a maximal controlled invariant into a smaller invariant set Ω in the neighbourhood of the equilibrium in finite time to guarantee the stability of FCS-MPC. The control input that steers the system state inside the invariant set is computed from a quadratic cost function based on a finite control input set. For this purpose, the dual mode predictive control scheme [79],[76],[101] is employed to handle state constraints along the predicted trajectories such that the state evolution is bounded in a predetermined invariant set.

To illustrate the main idea of the proposed scheme, the following discrete-time model in a state space framework is considered.

$$x_{k+1} = Ax_k + Bu_k \tag{6.7}$$

where the control input u_k belongs to a finite control set of p elements, such that

$$u_k = \{u_1, u_2, \ldots, u_p\} \tag{6.8}$$

and let us first consider the dual-mode predicted control law as

$$\begin{cases} u_k & = -Kx_k + c_k,\ k = 0, \ldots, n_c - 1 \\ u_k & = -Kx_k, \qquad\qquad k \geq n_c \end{cases} \tag{6.9}$$

where K is an unconstrained linear control law and c_k is the auxiliary control input that perturbs from the optimal unconstrained control input to ensure hard constraints.. The basic idea of the dual-mode control is to apply the constraints on the auxiliary input c_k up to a chosen horizon n_c, and after that the unconstrained control law K is applied beyond n_c, which in essence, the following cost function is solved in the dual-mode control scheme [79]:

$$J = \overbrace{\sum_{k=0}^{n_c-1} x_k^T Q x_k + u_k^T R u_k}^{J_{n_c}} + \overbrace{\sum_{k=n_c}^{\infty} x_k^T Q x_k + u_k^T R u_k}^{J_\infty} \tag{6.10}$$

where the cost beyond the horizon n_c can be viewed as a terminal control law.

Now let us illustrate the main idea of this section by first considering the system description given in (6.7) and the following cost function.

$$J = \sum_{k=0}^{\infty} x_k^T Q x_k + u_k^T R u_k \tag{6.11}$$

where Q and R matrices are positive and semi-positive definite. In order to re-parametrise the cost function (6.11) in terms of c_k, let us first define $A_k = A - BK$, where K is the state feedback gain in (6.9). Substituting (6.9) into (6.7), we can derive the closed-loop state prediction as

$$\begin{cases} x_{k+1} &= A_k x_k + Bc_k,\ k = 0, \ldots, n_c - 1 \\ x_{k+1} &= A_k x_k, \qquad\qquad k \geq n_c \end{cases} \tag{6.12}$$

Now based on the dual-mode control law (6.9) and the closed-loop state prediction (6.12), the cost function (6.11) can be re-parametrised in terms of c_k. At first, the cost function is re-derived for when $k \geq n_c$ (J_∞ in (6.10)) which is calculated as follows:

$$J = \sum_{k=0}^{\infty} \left[(A_k^i x_k)^T Q (A_k^i x_k) + (-KA_k^i x_k)^T R (-KA_k^i x_k) \right] \tag{6.13}$$

$$= x_k^T \overbrace{\sum_{k=0}^{\infty} \left[(A_k^i)^T Q (A_k^i) + (A_k^i)^T K^T R K A_k^i \right]}^{P} x_k \tag{6.14}$$

where $P = Q + K^T R K + A_k^T P A_k$. Using the above result and substituting dual-mode control law (6.9) and the closed-loop state prediction (6.12) into the cost function (6.11) yields (the following derivation is from [84]):

$$\begin{aligned}
J =& x_{k+n_c} P x_{k+n_c} + \sum_{k=0}^{n_c-1} \left[x_k^T Q x_k + (-K x_k + c_k)^T R (-K x_k + c_k) \right] \qquad (6.15)\\
=& (A_k x_{n_c-1} + B c_{k+n_c-1})^T P (A_k x_{n_c-1} + B c_{k+n_c-1}) + \\
& x_{n_c-1}^T Q x_{n_c-1} + (-K x_{n_c-1} + c_{k+n_c-1})^T R (-K x_{n_c-1} + c_{k+n_c-1}) \\
& + \sum_{k=0}^{n_c-2} \left[x_k^T Q x_k + (-K x_k + c_k)^T R (-K x_k + c_k) \right] \\
=& x_{k+n_c-1}^T (Q + KRK + A_k^T P A_K) x_{k+n_c-1} + c_{k+n_c-1}^T (R + B^T P B^T) c_{k+n_c-1} \\
& + 2 x_{k+n_c-1}^T (K^T R + A_k^T P B) x_{k+n_c-1} \\
& + \sum_{k=0}^{n_c-2} \left[x_k^T Q x_k + (-K x_k + c_k)^T R (-K x_k + c_k) \right] \qquad (6.16)
\end{aligned}$$

Moreover, assuming P as the solution of Riccati equation and given that

$$\begin{aligned}
A_k^T P B - K^T R =& (A - BK)^T P B - K^T R \\
=& A^T P B - K^T B^T P B - K^T R \\
=& A^T P B - A^T P B (B^T P B + R)^{-1} R \\
& - A^T P B (B^T P B + R)^{-1} B^T P B \\
=& A^T P B \left[I - (B^T P B + R)^{-1} (R + B^T P B) \right] \\
=& 0 \qquad (6.17)
\end{aligned}$$

we can write:

$$\begin{aligned}
J =& x_{k+n_c-1}^T P x_{k+n_c-1} + c_{k+n_c-1}^T (R + B^T P B^T) c_{k+n_c-1} \\
& + \sum_{k=0}^{n_c-2} \left[x_k^T Q x_k + (-K x_k + c_k)^T R (-K x_k + c_k) \right] \qquad (6.18)
\end{aligned}$$

Similarly:

$$
\begin{aligned}
J &= x_{k+n_c-1}^T P x_{k+n_c-1} + \sum_{k=0}^{n_c-2} \left[x_k^T Q x_k + (-Kx_k + c_k)^T R (-Kx_k + c_k) \right] \\
&= x_{k+n_c-2}^T P x_{k+n_c-2} + c_{k+n_c-2}^T (R + B^T P B^T) c_{k+n_c-2} \\
&+ \sum_{k=0}^{n_c-3} \left[x_k^T Q x_k + (-Kx_k + c_k)^T R (-Kx_k + c_k) \right]
\end{aligned}
\tag{6.19}
$$

which leads to

$$
\begin{aligned}
J &= x_{k+n_c-1}^T P x_{k+n_c-1} + \sum_{k=0}^{n_c-2} \left[x_k^T Q x_k + (-Kx_k + c_k)^T R (-Kx_k + c_k) \right] \\
&= x_{k+n_c-2}^T P x_{k+n_c-2} + c_{k+n_c-2}^T (R + B^T P B^T) c_{k+n_c-2} \\
&+ \sum_{k=0}^{n_c-3} \left[x_k^T Q x_k + (-Kx_k + c_k)^T R (-Kx_k + c_k) \right]
\end{aligned}
\tag{6.20}
$$

By rearranging it, we can also write as:

$$
\begin{aligned}
J &= x_{k+n_c-2}^T P x_{k+n_c-2} + c_{k+n_c-1}^T (R + B^T P B^T) c_{k+n_c-1} + c_{k+n_c-2}^T (R + B^T P B^T) c_{k+n_c-2} \\
&+ \sum_{k=0}^{n_c-3} \left[x_k^T Q x_k + (-Kx_k + c_k)^T R (-Kx_k + c_k) \right]
\end{aligned}
$$

By repeating the above calculations and expressing all the terms in the sum eventually leads to

$$
J = \sum_{k=0}^{n_c-1} c_{k+i}^T (R + B^T P B^T) c_{k+i} + x_k^T P x_k \tag{6.21}
$$

Note here that the unconstrained control law K in (6.9) and P matrix in the above cost function are chosen based on the stability condition specified in Theorem 6.2.1.

Now let us consider the system constraints as specified below,

$$\begin{aligned} \underline{X} \leq x_k \leq \overline{X} \\ \underline{U} \leq u_k \leq \overline{U} \end{aligned} \tag{6.22}$$

where $\underline{X}, \overline{X}$ and $\underline{U}, \overline{U}$ are state and control input constraints respectively. To guarantee the feasibility of the optimisation problem subject to constraints, it is necessary to augment the cost function (6.21) to include linear inequality constraints which represents a positive invariant set satisfying the constraints. There are two main invariant set, namely an ellipsoid and polyhedra invariant set. The ellipsoid invariant set is popular due to its link with Lyapunov stability theory and can easily be computed using LMI. However the serious drawback is that the set is too conservative and can not handle the asymmetric constraints. On the other hand polyhedral invariant set does not have the problem of being too conservative and also can handle asymmetric constraints. In the following, we consider the polyhedral invariant set for FCS-MPC.

For the dual model scheme in (6.9), when $k \geq N$ the resulting closed loop system (A_k) can be considered as an unforced linear system which constraints are not active. The largest set of initial conditions for which an unforced linear system satisfies all constraints is often referred to as the Maximal Admissible Set (MAS) denoted by $\mathcal{O}_\infty$.

$$\mathcal{O}_\infty = \{x : CA_k x \in \mathcal{Z}, -KA_k x \in \mathcal{U}, A_k x \in \mathcal{X}\} \tag{6.23}$$

Due to the infinite horizon, the computation of the above set $\mathcal{O}_\infty$ is intractable.

Based on the results of Gilbert and Tan [40], if the system is closed-loop stable and $\mathcal{O}_\infty$ is closed and bounded, the MAS $(\mathcal{O}_\infty)$ is finitely determined such that $\mathcal{O}_\infty$=$\mathcal{O}_{t+1}$= $\mathcal{O}_t$, in turn $\mathcal{O}_\infty \subseteq \mathcal{O}_{t+1} \subseteq \mathcal{O}_t$. The set $\mathcal{O}_t$ is the set of initial conditions for which all constraints are fulfilled up until time t.

$$\mathcal{O}_t = \{x : CA_k x \in \mathcal{Z}, -KA_k x \in \mathcal{U}, A_k x \in \mathcal{X}, \forall i \in \{1, 2, \ldots, t\}\} \tag{6.24}$$

The determination of MAS is explained in detail in [40], [97],[85] and it is also possible to obtain the MAS using the routines available in the Multi-Parametric Toolbox [62].

Now considering when $k \leq N$ in (6.9), the the auxiliary control c_k is used as a perturbation to satisfy the constraints, therefore an extension of MAS, referred to as MCAS (maximum control admissible set) to incorporate c_k can be defined as follows [97]:

$$Sc = \{x : \exists C \ \text{s.t.} \ M_0 x + N_0 C \leq d_0\} \tag{6.25}$$

For $c_k > 0$, the resulting MCAS in (6.25) is larger than the MAS, as increasing the control horizon n_c implies more time-steps to move the state into the MAS through the action of perturbations. Hence, the MCAS gets larger as n_c increases. Finally, by incorporating the constraints in (6.25), the optimization function in (6.21) is rewritten as

$$J = \sum_{k=0}^{n_c-1} C_{k+i}^T (R + B^T P B^T) C_{k+i} + x_k^T P x_k \tag{6.26}$$

$$\textit{subject to} \ \ M_0 x + N_0 C \leq d_0 \tag{6.27}$$

6.3 Application to Voltage Source Converter

The scope of the proposed FCS-MPC is set to control the current in synchronous reference frame, hence we assume that there exists a DC-bus voltage controller which commands the reference input for d-axis current (i_d) to stabilise the DC-bus voltage. Also, we assume that three-phase grid voltage is balanced and symmetric, and the load is resistive. The following state space model of the converter in discrete time is considered in the design.

$$x(k+1) = A_k x(k) + B_k u_d(k) \tag{6.28}$$

$$y(k) = C_k x(k) \tag{6.29}$$

where

$$A = \begin{bmatrix} 1 - T_s \frac{R}{L_s} & \omega \\ -\omega & 1 - T_s \frac{R}{L_s} \end{bmatrix}, \quad B = \begin{bmatrix} \frac{-T_s}{2L_s} & 0 \\ 0 & \frac{-T_s}{2L_s} \end{bmatrix}, \quad C = \begin{bmatrix} 1 & 0 \\ 0 & 1 \end{bmatrix} \tag{6.30}$$

and the state and control inputs are $x = [i_d, i_q]^T$ and $u_d = T_{dq} S_{abc}$ respectively, where T_{dq} is the synchronous reference transformation matrix and the finite switching inputs, S_{abc} in three phase frame is given as

Table 6.1: Switching vectors of three phase VSC

S_i	S_a	S_b	S_c
S_0	0	0	0
S_1	1	0	0
S_2	1	1	0
S_3	0	1	0
S_4	0	1	1
S_5	0	0	1
S_6	1	0	1
S_7	1	1	1

For each switching vectors, we can associate the voltage vectors in the synchronous-reference frame as shown in Table 6.2. To keep the system states, namely i_d and i_q currents closely to the reference trajectories, the cost function

Table 6.2: Synchronous-reference frame transformed switching vectors of three phase VSC

S_i	V_d	V_q
S_0	0	0
S_1	$\frac{2}{3}V_{dc}cos\theta$	$-\frac{2}{3}V_{dc}sin\theta$
S_2	$\frac{2}{3}V_{dc}cos(\theta - \frac{2\pi}{3})$	$-\frac{2}{3}V_{dc}sin(\theta - \frac{2\pi}{3})$
S_3	$\frac{2}{3}V_{dc}cos(\theta - \frac{4\pi}{3})$	$-\frac{2}{3}V_{dc}sin(\theta - \frac{4\pi}{3})$
S_4	$-\frac{2}{3}V_{dc}cos\theta$	$\frac{2}{3}V_{dc}sin\theta$
S_5	$-\frac{2}{3}V_{dc}cos(\theta - \frac{2\pi}{3})$	$\frac{2}{3}V_{dc}sin(\theta - \frac{2\pi}{3})$
S_6	$-\frac{2}{3}V_{dc}cos(\theta - \frac{4\pi}{3})$	$\frac{2}{3}V_{dc}sin(\theta - \frac{4\pi}{3})$
S_7	0	0

in (6.26) is modified to include the prediction penalty term as shown below,

$$J = \sum_{k=0}^{n_c-1} C_{k+i}^T (R + B^T P B^T) C_{k+i} + x_k^T P x_k + J_p \tag{6.31}$$

$$\textit{subject to } \; M_0 x + N_0 C \leq d_0 \tag{6.32}$$

where the extra term that penalises the predicted behaviour (J_p) is defined via

$$J_p = |x^* - x_i^p(C_k)| \tag{6.33}$$

Considering that the auxiliary control input C_k in (6.31) belongs to the finite set of inputs as,

$$C_k = \{S_0, S_1, \ldots, S_7\} \tag{6.34}$$

which represents the eight possible switching states of the converter, the $x_i^p(C_k)$ is the predicted state variables of the system for each possible control action. The optimisation problem in (6.31) can not readily be solved using a general quadratic programming solver such as the one we presented earlier in sections. Instead, due to the integer variables of switching input, the above optimisation

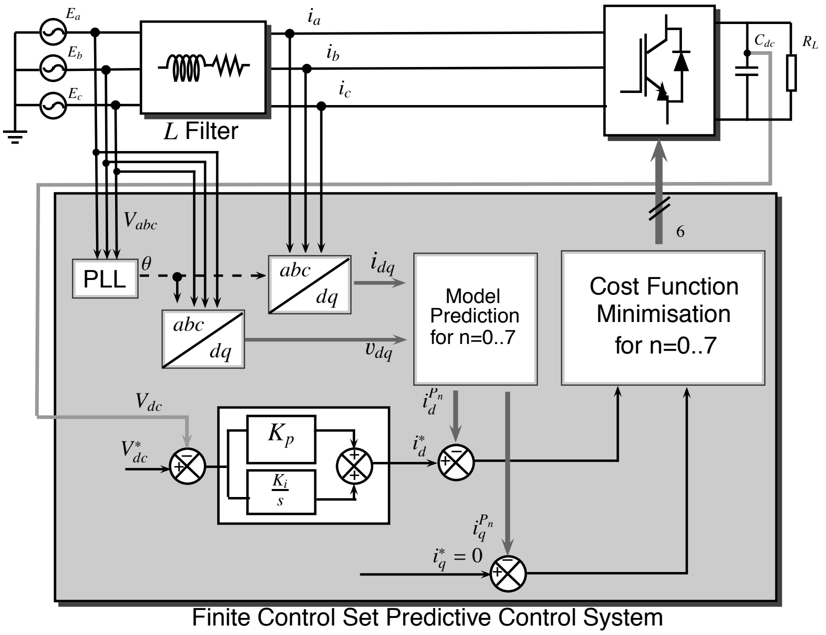

Figure 6.3: Finite control set predictive control system for grid-connected VSC: Model Prediction and Cost Minimisation part is executed iteratively for all possible switching inputs ($n = 0..7$) at each sampling instant. The switching inputs to the converter are directly controlled based on the cost minimisation

problem is regarded as an integer quadratic programming (IQP), which in general one needs to consider the method called branch and bound, to efficiently solve the problem. In this work, given that there are only eight switching inputs and by keeping the length of prediction horizon relatively small (for a computational reason, one-step ahead prediction is used), the computational load becomes insignificant. Hence it is computationally feasible to enumerate the all possible combination of inputs in the cost function (6.31), subsequently the cost function values are compared and the solution generating the minimum value is taken as the optimal solution.

Finally, the overall control scheme of FCS-MPC is shown in Figure 6.3, and it can be seen that the PWM module is no longer required, which instead the switching inputs are directly computed from the cost function minimisation.

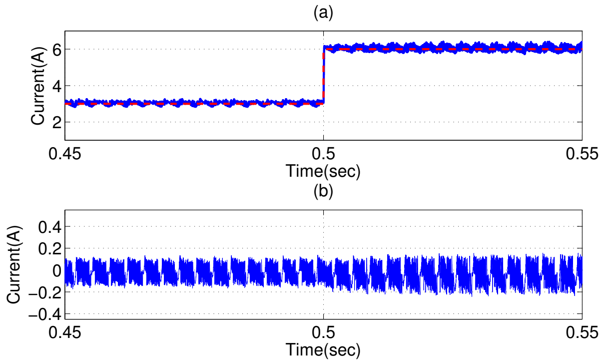

Figure 6.4: The simulated response of (a) i_d and (b) i_q current (blue) to a step change in reference i_d current (red) from 3 A to 6 A.

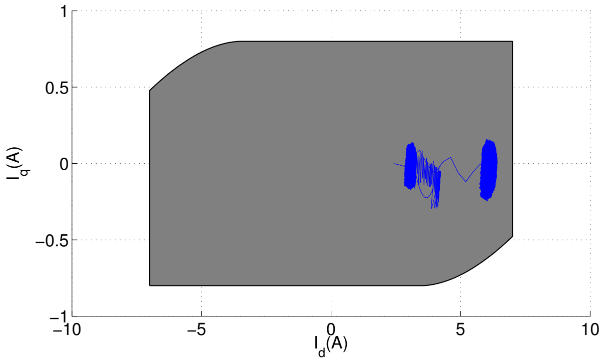

Figure 6.5: The plot of simulated i_d and i_q currents (blue) to a step change in reference i_d current from 3 A to 6 A with MCAS.

6.4 Simulation and Experimental Results

The proposed FCS-MPC in section 6.2 is validated both experimentally and using the nonlinear simulation model. The system parameter used for both validations are shown in Table 6.3.

The cost function parameter is set as $n_c = 1$, $Q = I_2$ and $R = 0.1 * I_2$ and following from the Theorem 6.2.1 we obtain

$$P = \begin{bmatrix} 50.2787 & -0.0000 \\ -0.0000 & 50.2787 \end{bmatrix}, K = \begin{bmatrix} -0.0157 & -0.0000 \\ -0.0000 & -0.0157 \end{bmatrix} \tag{6.35}$$

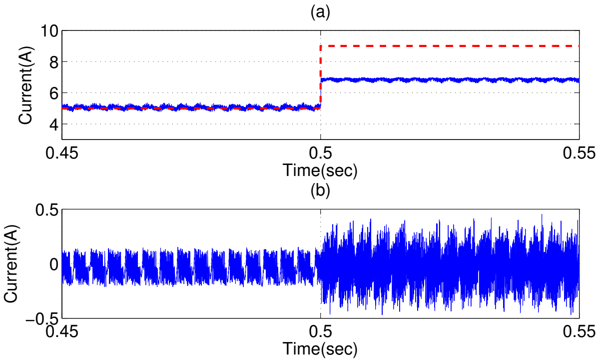

Figure 6.6: The simulated response of (a) i_d and (b) i_q current (blue) for a step change in reference i_d current (red) from 5 A to 8 A.

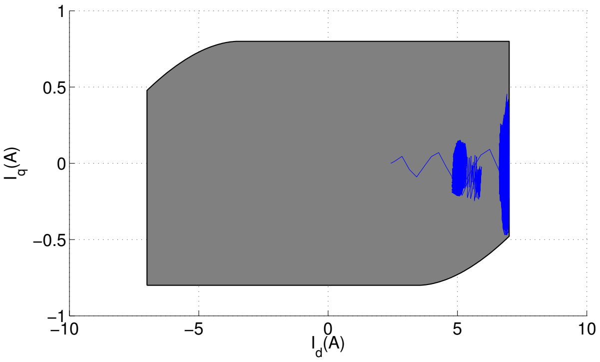

Figure 6.7: The plot of simulated i_d and i_q currents (blue) to a step change in reference i_d current from 5 A to 8 A with MCAS.

By setting the constraints for i_d and i_q currents as

$$-0.7A \leq i_q(k) \leq 0.7A \tag{6.36}$$

$$-7A \leq i_d(k) \leq 7A \tag{6.37}$$

and on the above cost function parameters, a MCAS is obtained on a procedure described in section 6.2 which is shown as a grey area in Figure 6.5. Note here that the constraints specified in 6.36 represents the maximum allowed level of current in the converter. This is usually defined based on various factors such

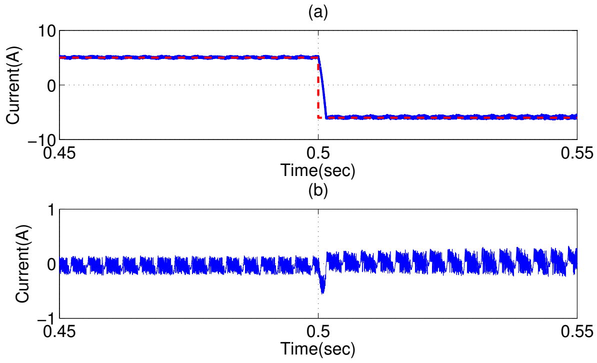

Figure 6.8: The simulated response of i_d and i_q current (blue) for a step change in reference i_d current (red) from 5 A_{peak} to -6 A_{peak}.

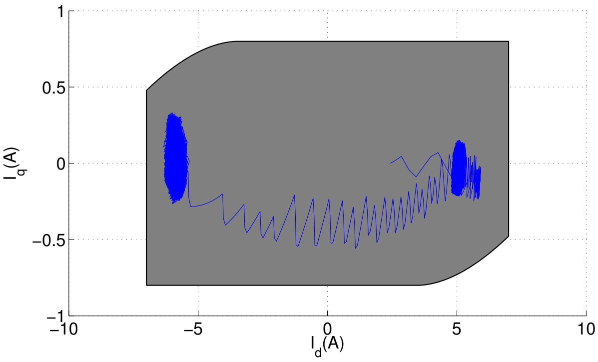

Figure 6.9: The simulated response of i_d and i_q currents (blue) to a step change in reference i_d current from 5 A to -6 A with MCAS.

as power rating of IGBT and the whole system but in this case the current limits are chosen for the demonstration purposes.

First we discuss the simulation results of rectification mode. Figure 6.4 and Figure 6.5 are the step response of i_d and i_q current when the i_d current reference input is changed from 3A to 6A. A good tracking performance of reference input in i_d current can be observed in Figure 6.4 (a), and the response of i_q current in Figure 6.4 (b) also shows a good regulation around zero current for unity power factor. In terms of feasibility, Figure 6.5 shows both currents are within the limits specified by the MCAS.

Table 6.3: Grid-connected VSC system parameters

Symbol	Parameter Name	Value	Unit
V_{grid}	Grid Voltage	30	V
f_{grid}	Grid Frequency	50	Hz
L_s	Input Filter Inductance	8.9	mH
R_L	Input Filter ESR	8.3	Ω
C_{dc}	DC-link Capacitance	700	μF
R_{dc}	Load Resistance	$20-40$	Ω

To test the handling of system constraints, a step change of i_d current reference from 5A to 8A is simulated. As shown in Figure 6.6, the response of i_d current gets saturated to 7A after the reference input exceeds the current constraint level specified in (6.36). However, it is also interesting to note the increase in the amount of ripple in the i_q current. This is mainly due to reduced number of effective switching states, since the switching states that results infeasibility (i.e violation of constraint) are not considered in the cost optimisation. In other words, a less number of switching states to control the converter results in a larger feedback error in the current. Figure 6.7 shows clearly that the simulated i_d and i_q currents are confined within the MCAS. For the regeneration mode, a step change in the i_d current from 5A to -6A is applied. Figure 6.8–6.9 are the simulation results in regeneration mode which shows a good tracking performance in i_d and i_q current.

The same parameters and test scenarios are repeated in experimental validations. First, experimental results in rectification mode is discussed.

Figure 6.10 is the measured response of i_d current to a step change in the reference input from 5 A to 6 A and the response of i_q current is shown in Figure 6.11. Both results shows a good tracking response to a reference input and a regulation around zero current even during the transient phase. Figure 6.12 is the measured response of three phase current. Figure 6.13 shows the measured current with respect to MCAS. Although the i_d and i_q currents are mostly

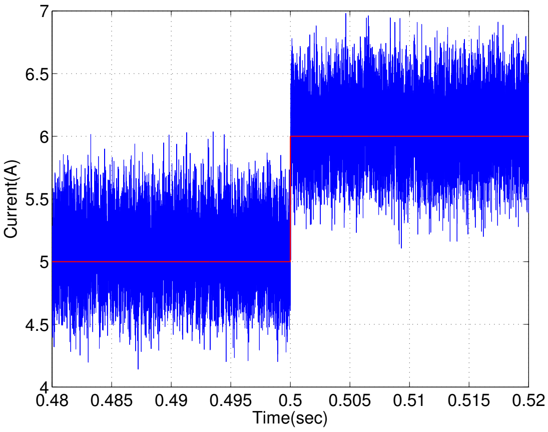

Figure 6.10: The measured response of i_d current (blue) to a step change in reference i_d current (red) from 5 A to 6 A: rectification mode

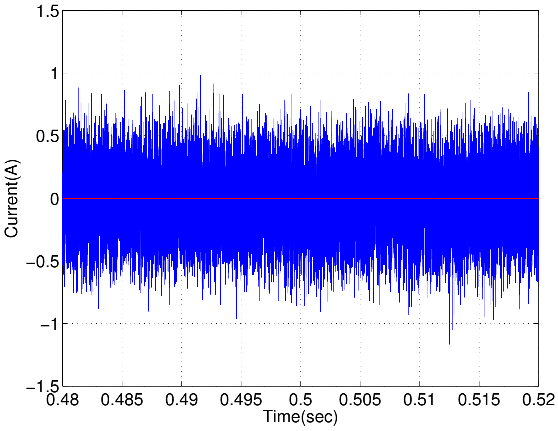

Figure 6.11: The measured response of i_q current (blue) when a step change in reference i_d current occurs from 5 A to 6 A: rectification mode

kept inside the MCAS, due to unaccounted noise/disturbance in the actual system, there are occasions where the current level exceeds the boundaries of MCAS.

For the regeneration mode test, a step change in the i_d current from 5A to -9A is applied after an extra current is injected in the DC-bus. As shown in Figure 6.14, the i_d current is saturated to -7A which was the limit set in (6.36) and as we also observed in the simulation result the amount of ripple in i_q current (Figure 6.15) is slightly increased after i_d current is saturated. Figure 6.16 shows the

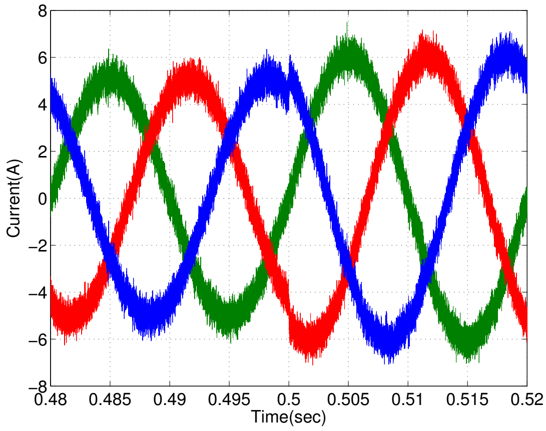

Figure 6.12: The measured response of i_{abc} current to a step change in reference i_d current from 5 A to 6 A: rectification mode

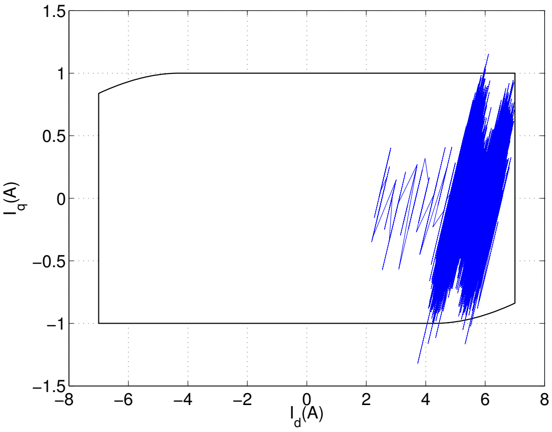

Figure 6.13: The measured response of i_d and i_q current in MCAS: rectification mode

response of three phase current where a phase shift of $180°$ occurs when the mode transition is made. Figure 6.17 shows the response of i_d and i_q current in the MCAS, as we have observed earlier due to the noise in the actual system, the level of i_{dq} current exceeds the boundaries of MCAS.

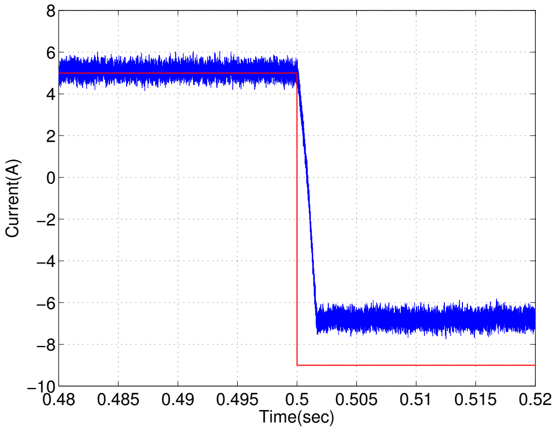

Figure 6.14: The measured response of i_d current (blue) to a step change in reference i_d current (red) from 5 A to -9 A: regeneration mode

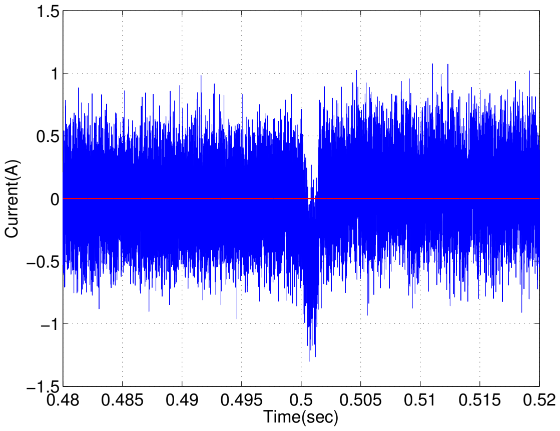

Figure 6.15: The measured response of i_q current (blue) to a step change in reference i_d current from 5 A to -9 A: regeneration mode

6.5 Conclusions

In this chapter we have presented first the stability analysis of FCS-MPC in two different aspects. The first method, which we referred to as Lyapunov statbility based approach, considered the effect of quantised control inputs on the system states as bounded disturbances, and then treated the stability problem of FCS-MPC based on the concept of practical stability. In order to satisfy the practical stability condition, a terminal weighting matrix and a local controller were designed to show that the cost function is practical CLF. In the second

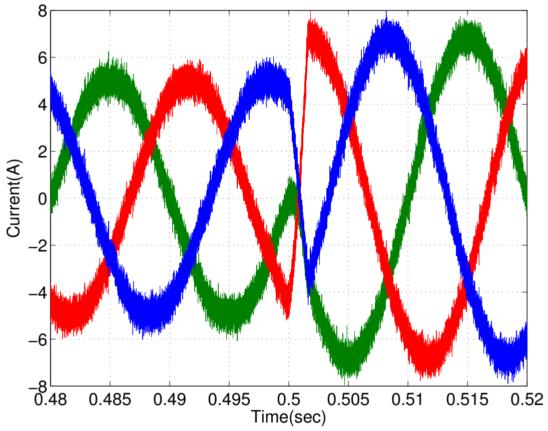

Figure 6.16: The measured response of i_{abc} current to a step change in reference i_d current from 5 A to -9 A: regeneration mode

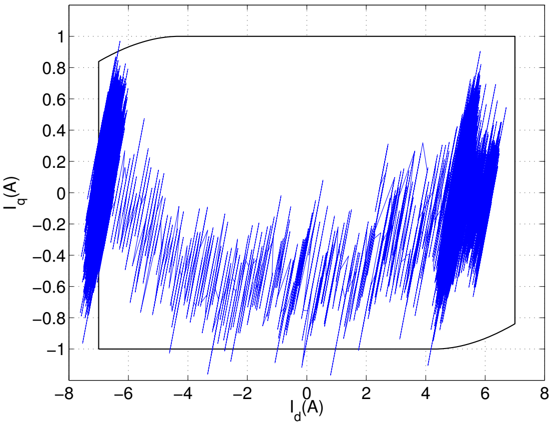

Figure 6.17: The measured response of i_d and i_q current in MCAS: regeneration mode

method, a more direct approach was considered

Based on the Lyapunov statbility based approach of FCS-MPC, the cost function of FCS-MPC was re-defined based on the dual-mode MPC strategy and later augmented it with a linear inequality constraint that represented a maximal control admissible set. The led to a new FCS-MPC method that not only ensures the practical stability but also bounds the i_d and i_q currents to be within the safe operating limit. Both simulation and experimental results showed a satisfactory control performance as well as a constraint handling of

i_d and i_q currents. However due to an unaccounted noise in the actual system, an occasional violation of constraints were observed.

CHAPTER 7

Conclusions

This thesis has presented a continuous-time model predictive control paradigm to control the bi-directional power flow of a grid-connected VSC. In the following, we summarise key contributions as well as some recommended future works based on this thesis.

7.1 Summary of Contributions and Future Works

Model Predictive Voltage Control

A multi-variable control scheme based on a general framework of model predictive control is presented which centralised the control structure to regulate both DC-bus voltage and input currents in the synchronous reference frame. In order to reduce the complexity of tuning, pre-stabilisation techniques were presented to satisfy desired closed-loop responses as well as improving the numerical conditioning of the predictive controller. An extension of prescribed degree of stability method in [109] is made to consider the parameter uncertainties and through experimental results it was shown that under a grid impedance variation the proposed robust method improved the control performance. This idea was further extended to consider a regional pole placement method as a pre-stabilisation technique, which allowed to meet more complex closed loop responses such as decay rate and minimum damping ratio. Both contributions in the pre-stabilisation technique showed the improvement in robustness as well as reducing the complexity in the tuning of MPC. In order to keep the modulation index of switching control input to within a linear region, constrained optimisation with switching control input constraints is also formulated and implemented in the synchronous reference frame. Compared to the traditional control scheme, such as a cascaded PI control, the presented work offers a simpler framework to handle the parametric uncertainties which can be obtained using the LMI framework, furthermore by using the idea of prescribed degree of stability the tuning of the overall controller is simplified compared to the cascaded control scheme. For the future work, as the proposed MPVC system has been developed for a stand-alone grid-connected VSC with a simple DC-load, an ideal extension of the system would be to include a more realistic load conditions such as motor drives and renewable energy sources.

Model Predictive Current Control for LCL filter

Model predictive current control method have been presented for grid-connected VSC with an LCL filter. In the proposed method, a reduced-order model of LCL filter utilised to keep the complexity of the controller to minimal. However, since the control design relies on the reduced-order dynamics, a nominal model predictive current controller alone was not enough to suppress the resonant harmonics of LCL filter. To attenuate LCL filter resonance, a disturbance rejection controller was added which its main idea is to keep the measured current close to the nominal current trajectories. For the design of disturbance rejection controller, we have employed a finite-frequency H_∞ approach based on GKYP lemma. The experimental results showed a significant improvement in suppressing LCL filter resonance while supplying the stable grid current to the grid. Compared to the traditional active damping method, which requires an extra hardware circuitry for measuring grid side current of the filter capacitor, the presented method requires no extra hardware. Furthermore, the disturbance rejection controller ensures the closed-loop stability with a prescribed transient requirement and constrained control in account of disturbance ensures constraint feasibility. A recommended extension of this work is to consider the grid impedance variation in the presented design framework. Since the grid impedance variation affects the resonant harmonic frequency of LCL filter, a further investigation into designing a robust stabilising control law for nominal model predictive current controller and a robust finite-frequency control law for damping the LCL filter resonance are required.

Model Predictive Resonant Control

A model predictive resonant control (MPRC) scheme has been proposed for a three phase grid-connected VSC. The main idea of this approach was to embed a sinusoidal resonant module in the system model to reject/follow periodic disturbances/reference. The basic design framework of MPRC followed the same as in the previous methods except the use of augmented model with an embedded resonant module. We have also investigated a practical consideration of grid frequency variations for the proposed MPRC. For this problem, we have proposed a robustly stabilising feedback law and introduced it into the design of MPRC by using the concept of closed-loop paradigm approach. A nonlinear simulation test was carried out to confirm robust and stable responses of the grid current under grid frequency variations. For another commonly encountered problem in the grid-connected VSC, we investigated a problem of multiple harmonic distortions on the grid current caused by grid voltage harmonics. To eliminate these unwanted harmonics while preserving the stability of the overall control system, two separate disturbance rejection controllers were designed based on LQR method and the common Lyapunov matrix was found to ensure the stability of the overall system. Experimental results were carried out to illustrate the efficacy of the proposed method. As similar to the work in previous chapter, the main benefit of the proposed method lies at the development of model-based harmonic compensator. The proposed method not only ensures that the targeted harmonics are suppressed, but also develops the stability criteria that ensures the closed-loop stability with nominal controller is ensured. By using this approach, the parametric uncertainty especially with grid frequency variation can be considered and compensated in a more systematic way.

Finite-Control-Set MPC with constraints

Based on the motivation that a conventional FCS-MPC for power electronic applications does not incorporate stability guarantee by default, we have investigated a method that not only ensures the practical stability but also bounds the system states, which were i_d and i_q currents to be within the safe operating limit. In the proposed method, the cost function of FCS-MPC was re-defined based on the dual-mode MPC strategy and later augmented it with a linear inequality constraint that represented a maximal control admissible set. Both simulation and experimental results showed a satisfactory control performance as well as a constraint handling of i_d and i_q currents. The presented showed a way of including system constraints in the traditional FCS-MPC. The modification of cost function based on Lyapunov stability theorem and bounding the system states within the invariant set enhances the stability of FCS-MPC. However due to an unaccounted noise in the actual system, an occasional violation of constraints were observed, Therefore a robust control strategy is recommended such as the concept of constraint tightening to mitigate this problem.

Bibliography

[1] IEEE recommended practice for monitoring electric power quality. *IEEE Standard 1159*, 1995.

[2] Limits for harmonic current emissions (equipment input current less than 16 a per phase). *IEC Standard 1000-3-2*, 1995.

[3] IEEE trial-use standard definitions for the measurement of electric power quantities under sinusoidal, non-sinusoidal, balanced, or unbalanced conditions. *IEEE Standard 1459*, 2000.

[4] IEEE standard for interconnecting distributed resources with electric power systems. *IEEE15471*, 2003.

[5] V. Dua A. Bemporad, M. Morari and E.N. Pistikopoulos. The explicit linear quadratic regulator for constrained systems. *Automatica*, 38(1):3–20, 2002.

[6] R. Teodorescu A. V. Timbus, M. Ciobotaru and F. Blaabjerg. Adaptive resonant controller for grid-connected converters in distributed power generation systems. *Twenty-First Annual IEEE Applied Power Electronics Conference and Exposition, 2006. APEC '06*, 47:1601–1606, 2006.

[7] T. Ackermann. *Wind Power in Power Systems*. John Wiley & Sons Ltd, 2005.

[8] R.P. Aguilera and D.E. Quevedo. On stability and performance of finite control set mpc for power converters. *Workshop on Predictive Control of Electrical Drives and Power Electronics (PRECEDE)*, pages 55–62, Oct. 2011.

[9] R.P. Aguilera and D.E. Quevedo. On the stability of mpc with a finite input alphabet. *18th IFAC World Congress*, pages 7975–7980, Aug. Milan, 2011.

[10] A. Alessio and A. Bemporad. A survey on explicit model predictive control. *Nonlinear Model Predictive Control: Towards New Challenging Applications. Springer*, 2009.

[11] R. Alezana, P. Aguilera and D. Quevedo. Steady-state issues with finite control set model predictive control. *35th Annual Conference of IEEE Industrial Electronics*, pages 1776–1781, Nov. 2009.

[12] B. D. O. Anderson and J. M. Moore. *'Linear Optimal Control'*. Prentice-Hall, 1971.

[13] T. W. Kim B. H. Kwon and J. H. Youn. A novel svm-based hysteresis current controller. *IEEE Transactions on Power Electronics*, 13:297–307, 1998.

[14] J.A. Rossiter B. Kouvaritakis and A.O.T. Chang. Stable generalized predic- tive control: an algorithm with guaranteed stability. *Proceedings IEE, Part D*, 139(4):349–362, 1992.

[15] J.A. Rossiter B. Kouvaritakis and J. Schuurmans. Efficient robust predictive control. *IEEE Transactions on Automatic Control*, 45:1545–1549, 2000.

[16] M. Cannon B. Kouvaritakis and J. A. Rossiter. Recent developments in generalized predictive control for continuous-time systems. *International Journal of Control*, 72(2):164–173, 1999.

[17] S. Bemporad A. B. Picasso, Pancanti and A. Bicchi. *Analysis and Design of Hybrid Systems*. Elvesier, 2003.

[18] A. Bemporad and M. Morari. Robust model predictive control: A survey. *Robustness in Identification and Control*, 245:207–226, 1999.

[19] V. Blasko and V.Kaura. "A new mathematical model and control of a three-phase ac-dc voltage source converter.". *IEEE Transations on Power Electronics*, 12(1), 1997.

[20] V. Blasko and V.Kaura. "A novel control to actively damp resonance in input LC filter of a three-phase voltage source converter". *IEEE Transations on Industry Applications*, 33(2), 1997.

[21] B. K. Bose. An adaptive hysteresis-band current control technique of a voltage-fed pwm inverter for machine drive system. *IEEE Transactions on Industrial Electronics*, 37:402–408, 1990.

[22] S. Boyd, L. El Ghaoui, E. Feron, and V. Balakrishnan. *"Linear Matrix Inequalities in System and Control Theory"*. Studies in Applied Mathematics. SIAM, Philadelphia, PA, June 1994.

[23] D. M. Brod and D. W. Novotny. Current control of vsi-pwm inverters. *IEEE Transactions on Industry Application*, 21:562–570, 1985.

[24] S. Buso and P. Mattavelli. *Digital control in Power electronics*. Morgan and Claypool Publishers, 2006.

[25] D. M. Prett C. E. Garcia and M. Morari. Model predictive control: theory and practice - a survey. *Automatica*, 25(3):457–465, 1989.

[26] P. J. Campo and M. Morari. Robust model predictive control. *In Proceedings of American Control Conference*, 1987.

[27] M. Chilali and P. Gahnet. "H_∞ design with pole placement constraints: an LMI approach". *IEEE Transactions on Automatic Control*, 41(3):358–367, 1996.

[28] S. K. Chung. Phase locked loop for grid-connected three phase power conversion systems. *IEEE Transactions*, 147:213–219, 2000.

[29] D. M. Raimondo D. Munez de la Pena J. M. Bravo A. Ferramosca D. Limon, T. Alamo and E. F. Camacho. Input-to-state stability: A unifying framework for robust model predictive control. *Lecture Notes in Control and Information Sciences*, 384:1–26, 2009.

[30] G. Ferrari-Trecate D. Mignone and M. Morari. Stability and stabilization of piecewise affine and hybrid systems: an lmi approach. *IEEE Conference on Decision and Control*, 2000.

[31] J. B. Rawlings D. Q. Mayne and C. Rao. "Constrained model predictive control: Stability and optimality". *Automatica*, 36(2), 2000.

[32] M. M. Seron D. Q. Mayne and S. V. Rakovic. "Robust Model Predictive Control of Constrained Linear Systems with Bounded Disturbances". *Automatica*, 41(2), 2005.

[33] D.G. Holmes D.N. Zmood and G.H.Bode. Frequency-domain analysis of three-phase linear current regulators. *IEEE Transaction on Industry Applications*, 37(2):601–610, 2001.

[34] J. R. Rodriguez et. al. Pwm regenerative rectifiers: State of the art. *IEEE Transactions on Industrial Electronics*, 52(1), Feb, 2005.

[35] E. Feron, V. Balakrishnan, S. Boyd, and L. El Ghaoui. Numerical methods for h2 related problems. In *American Control Conference, 1992*, pages 2921–2922, 1992.

[36] K. Furuta and S. B. Kim. Pole assignment in a specified disk. *IEEE Transaction on Automatic Control*, 32(5):423–427, 1987.

[37] M. Newman G. Bode, P. C. Loh and D. G. Holmes. An improved robust predictive current regulation algorithm. *IEEE Transaction on Industry Applications*, 41(6):1720–1733, 2005.

[38] P. Gahinet and P. Apkarian. "A linear matrix inequality approach to H_∞ control.". *Int. J. Robust Nonlinear Control*, 4(4):421–448, 1994.

[39] T. Geyer. A comparison of control and modulation schemes for medium-voltage drives: Emerging predictive control concepts versus pwm-based schemes. *IEEE Transaction on Industry Applications*, 47(3):1380–1389, 2011.

[40] E. G. Gilbert and K. T. Tan. Linear systems with state and control constraints: The theory and application of maximal output admissible sets. *IEEE Transactions on Automatic Control*, 36(9):1008–1020, 1991.

[41] Sewan Choi Hea-Gwang Jeong, Kyo-Beum Lee and Woojin Choi. Performance improvement of lcl-filter-based grid-connected inverters using pqr power transformation. *IEEE Transaction on Power Electronics*, 25(5):1320–1330, 2010.

[42] W. A. Hill and S. C. Kapoor. Effect of two-level pwm sources on plant power system harmonics. *IEEE-IAS Annual Meeting*, pages 1300–1306, 1998.

[43] T. Iwasaki and S. Hara. "Generalized KYP Lemma: unified frequency domain inequalities with design applications.". *IEEE Transactions on Automatic Control*, 50(1), 2005.

[44] C. Wessels J. Dannehl and F. W. Fuchs. Limitations of voltage-oriented pi current control of grid-connected pwm rectifers with lcl filters. *IEEE Transaction on Industrial Electronics*, 56(2):380–388, 2009.

[45] S. Hansen J. Dannehl, F. W Fuchs and P. ThÃ¸gersen. Investigation of active damping approaches for pi-based current control of grid-connected pulse width modulation converters with lcl filters. *IEEE Transaction on Industry Applications*, 46(4):1509–1517, 2010.

[46] J. Fischer J. E. Huerta, J. Castello-Moreno and R. Garcia-Gil. A synchronous reference frame robust predictive current control for three-phase grid-connected inverters. *IEEE Transaction on Industrial Electronics*, 57(3):954–962, 2010.

[47] V. F. Montagner J. Gabe and H. Pinheiro. Design and implementation of a robust current controller for vsi connected to the grid through an lcl-filter. *IEEE Transaction on Power Electronics*, 24(6):1444–1452, 2009.

[48] J. T. Bialasiewicz E. Galvan R. C. Portillo Guisado M. A. M. Prats J. I. Leon J. M. Carrasco, L. G. Franquelo and N. Moreno-Alfonso. Power-electronic systems for the grid integration of renewable energy sources: A survey. *IEEE Transactions on Industrial Electronics*, 53(4):1002–1016, 2006.

[49] C. Silva P. Correa P. Lezana P. Cortes J. Rodriguez, J. Pontt and U. Ammann. Predictive current control of a voltage source inverter. *IEEE Transaction on Industrial Electronics*, 54(1):495–503, 2007.

[50] C. Silva P. Cortes S. Rees J. Rodriguez, J. Pontt and U. Ammann. Predictive direct torque control of an induction machine. *In Proceedings of 11th EPE-PEMC, Riga, Latvia*, 2004.

[51] J. R. Espinoza P. Zanchetta H. Abu-Rub H. A. Young J. Rodriguez, M.P. Kazmierkowski and C.A. Rojas. State of the art of finite control set model predictive control in power electronics. *IEEE Transactions on Industrial Informatics*, 9(2):1003–1016, 2013.

[52] L. Jih-Sheng J. Rodriguez and P. F. Zheng. Multilevel inverters: A survey of topologies, controls, and applications. *IEEE Transaction on Industrial Electronics*, 49(4):724–738, 2002.

[53] P. Correa P. Lezana J. Rodriguez, J. Pontt and P. Cortes. Predictive power control of an ac/dc/ac converter. *In Proceedings of IEEE IAS Annual Meeting*, 2005.

[54] L. Jih-Sheng and P. F. Zheng. Multilevel converters-a new breed of power converters. *IEEE Transaction on Industry Applications*, 32(3):509–517, 1996.

[55] A. Kawamura K. P. Gokhale and R. G. Hoft. Dead beat microprocessor control of pwm inverter for sinusoidal output waveform synthesis. *IEEE Transaction on Industrial Applications*, IA-23(5):901–909, 1987.

[56] M. P. Kazmierkowski and L. Malesani. Current control techniques for three-phase voltage-sorce pwm converters: a survey. *IEEE Transaction on Industrial Electronics*, 45(5):814–822, 1998.

[57] H. Komurcugil and O. Kukrer. "Lyapunov-based control for three-phase pwm ac/dc voltage-source converters.". *IEEE Transations on Power Electronics*, 13(5), 1998.

[58] P. Mattavelli L. Malesani and S. Buso. Robust dead-beat current control for pwm rectifiers and active filters. *IEEE Transaction on Industry Applications*, 35(3):613–620, 1999.

[59] A. Linder and R. Kennel. Model predictive control for electrical drives. *In Proceedings of IEEE PESC, Recife, Brazil*, 2005.

[60] M. Lindgren. *Modeling and control of voltage source converters connected to the grid.* PhD thesis, Chalmers University of Technology, 1998.

[61] M. Liserre. Innovative control techniques of power converters for industrial automation. *PhD Thesis, Politechnico di Bari, Italy*, 2001.

[62] P. Grieder M. Kvasnica and M. Baotic. Multi-parametric toolbox (mpt). *Swiss Federal Institute of Technology*, 2004.

[63] A. Dell'Aquila M. Liserre and F. Blaabjerg. "Stability improvement of an LCL-filter based three-phase active rectifier". *Proceedings of Power Electronics Specialist Conference*, 3:1195–1201, 2002.

[64] F. Blaabjerg M. Liserre and A. Dell Aquila. Step-by-step design procedure for a grid-connected three-phase pwm voltage source converter. *International Journal of Electronics*, 91:445–460, 2004.

[65] F. Blaabjerg M. Liserre, R. Teodorescu. Multiple harmonics control for three-phase grid converter systems with the use of pi-res current controller in a rotating frame. *IEEE Transaction on Power Electronics*, 21(3):836–841, 2006.

[66] R. Teodorescu M. Liserre and F. Blaabjerg. Stability of photovoltaic and wind turbine grid-connected inverters for a large set of grid impedance values. *IEEE Transaction on Power Electronics*, 21(1):263–272, Jan, 2006.

[67] W. Kolomyjski M. Malinowski, S. Stynski and M. P. Kazmierkowski. Control of three-level pwm converter applied to variable-speed-type turbines. *IEEE Transaction on Industrial Electronics*, 56(1):69–77, 2009.

[68] M. A. Dzieniakowski M. P. Kazmierkowski and W. Sulkowski. Novel space vector based current controllers for pwm inverters. *IEEE Transactions on Power Electronics*, 6:158–166, 1991.

[69] R. Krishnan M. P. Kazmierkowski and F. Blaajerg. *Control in Power Electronics: Selected Problems*. Academic Press, 2002.

[70] V. Balakrishnan M. V. Kothare and M. Morari. Robust constrained model predictive control using linear matrix inequalities. *In Proceedings of American Control Conference, Baltimore, USA*, 1994.

[71] V. Balakrishnan M. V. Kothare and M. Morari. Robust constrained model predictive control using linear matrix inequalities. *Automatica*, 32(10):1361–1379, 1996.

[72] J. Maciejowski. *Predictive Control with Constraints*. Prentice Hall, 2000.

[73] L. Magni and R. Scattolini. Robustness and robust design of mpc for nonlinear discrete-time systems. *Assessment and Future Directions of Nonlinear Model Predictive Control, Springer*, 2007.

[74] L. Malesani and P. Tenti. A novel hysteresis control method for current controlled vsi pwm inverters with constant modulation frequency. *IEEE Transactions on Industry Application*, Jan/Feb:88–92, 1990.

[75] M. Malinowski. Sensorless control strategies for three phase pwm rectifiers. *Ph.D. Thesis, Warsaw Univ. of Technology, Poland*, 2001.

[76] H. Michalska and D. Mayne. Robust receding horizon control of constrained nonlinear systems. *IEEE Transactions on Automatic Control*, 38:1623–1633, 1993.

[77] F.Blaabjerg M.Liserre and S. Hansen. Design and control of an lcl filter-based three phase active rectifier. *IEEE Transaction on Industry Applications*, 41(5):1281–1291, 2005.

[78] M. Morari and J. H. Lee. Model predictive control: Past, present and future. *Computers and Chemical Engineering*, 23(3):667–682, 1999.

[79] K. R. Muske and J. B. Rawlings. Model predictive control with linear models. *Journal of American Institute of Chemical Engineers (AIChE)*, 39(2):262–287, 1993.

[80] H. D. Tuan P. Apkarian and J. Bernussou. Continuous-time analysis,eigenstructure assignment and h2 synthesis with enhanced linear matrix inequalities (lmi) characterizations. *IEEE Transaction on Automatic Control*, 42(12):1941–1946, 2001.

[81] J. I. Yuz J. Rodriguez S. Vazquez P. Cortes, G. Ortiz and L. G. Franquelo. Model predictive control of an inverter with output lc filter for ups applications. *IEEE Transaction on Industrial Electronics*, 56(6):1875–1883, 2009.

[82] H. Demircioglu P. J. Gawthrop and I. Siller-Alcala. Multivariable continuous-time generalised predictive control: A state space approach to linear and nonlinear systems. *IEE Pt.D: Control Theory and Applications*, 1998.

[83] C. T. Pan and T. Y. Chang. An improved hysteresis current controller for reducing switching frequency. *IEEE Transactions on Power Electronics*, 9:97–104, 1994.

[84] G. Pannocchia and E. C. Kerrigan. Offset-free receding horizon control of constrained linear systems subject to time-varying setpoints and per-

sistent unmeasured disturbances. *Technical Report, University of Cambridge*, 2003.

[85] B. Pluymers, J. A. Rossiter, J. A. K. Suykens, and B. De Moor. The efficient computation of polyhedral invariant sets for linear systems with polytopic uncertainty. *IEEE American Control Conference, Portland, USA*, 2005.

[86] M. P. Kazmierkowski R. Kennel D. Quevedo P. Cortes and J. Rodriguez. Predictive control in power electronics and drives. *IEEE Transactions on Industrial Electronics*, 55(12), Dec 2008.

[87] J.K. Pedersen E. Cengelci S. U. Sulistijo-B. O. Woo R. Teodorescu, F. Blaabjerg, , and P. Enjeti. Multilevel converter - a survey. *Proceeding of European Conference on Power Electronics and Application*, Lausanne, Switzerland, 1999.

[88] M. Liserre R. Teodorescu, F. Blaabjerg and P.C. Loh. Proportional-resonant controller and filters for grid-connected voltage-source converters. *IEE Proceedings Electric Power Applications*, 153(5), Sept, 2006.

[89] J. Rodriguez R. Vargas, U. Ammann and J. Pontt. Reduction of switching losses and increase in efficiency of power converters using predictive control. *IEEE PESC*, pages 1062–1068, Jun. 2008.

[90] U. Ammann J. Rodriguez R. Vargas, P. Cortes and J. Pontt. Predictive control of a three phase neutral point clamped inverter. *IEEE Transactions on Industrial Electronics*, 54:2697–2705, 2007.

[91] S. B. Dewan R. Wu and G. Slemon. Analysis of an ac-to-dc voltage source converter using pwm with phase and amplitude control. *IEEE Transaction on Industry Applications*, 27(2):355–364, 1991.

[92] S. B. Dewan R. Wu and G. R. Slemon. Analysis of a pwm ac to dc voltage source converter under the predicted current control with a fixed switching frequency. *IEEE Transaction on Industry Applications*, 27:756–764, 1991.

[93] J. Rawlings and D. Mayne. Model predictive control: Theory and design. 2009.

[94] J. B. Rawlings. Tutorial overview of model predictive control. *IEEE Control Systems Magazine*, 49(1):1433–1443, 2000.

[95] J. B. Rawlings and K. R. Muske. "The stability of constrained receding horizon control". *IEEE Transations on Automatic Control*, 38:1512–1516, 1993.

[96] Pedro RodrÃguez Remus Teodorescu, Marco Liserre. "Grid Converters for Photovoltaic and Wind Power Systems". 2011.

[97] J. A. Rossiter. Model-based predictive control: A practical approach. 2003.

[98] J.A. Rossiter and B. Kouvaritakis. Numerical robustness and efficiency of generalised predictive control algorithms with guaranteed stability. *Proceedings IEE, Part D*, 141(3):154–162, 1994.

[99] J. Bordonau J. Gago D. Gonzalez S. Alepuz, S. Busquets-Monge and J. Balcells. Interfacing renewable energy sources to the utility grid using a three-level inverter. *IEEE Transactions on Industrial Electronics*, 53(5):1504–1511, 2006.

[100] R. Vargas U. Ammann S. Kouro, P. Cortes and J. Rodriguez. Model predictive control- a simple and powerful method to control power converters. *IEEE Transactions on Industrial Electronics*, 56(6), Jun 2009.

[101] P.O.M. Scokaert and J.B. Rawlings. Constrained linear quadratic regulation. *IEEE Transaction on Automatic Control*, 43(8):1163–1168, 1998.

[102] R. J. Svensson. Synchronization methods for grid-connected voltage source converters. *IEEE Transactions*, 148:1545–1549, 2001.

[103] T. Miyashita T. Kawabata and Y. Yamamoto. Dead beat control of three phase pwm inverter. *IEEE Transaction on Power Electronics*, 5:21–28, 1990.

[104] S. Kondo T. Noguchi, H. Tomiki and I. Takahashi. Direct power control of pwm converter without power- source voltage sensors. *IEEE Industry Applications*, 34(3):473–479, 1998.

[105] E. Twining and D. G. Holmes. Grid current regulation of a three-phase voltage source inverter with an lcl input filter. *IEEE Transaction on Power Electronics*, 18(3):888–895, May, 2003.

[106] S. V. Rakovic W. Langson, I. Chryssochoos and D. Mayne. Robust model predictive control using tubes. *Automatica*, 40(1):125–133, 2004.

[107] L. Wang. Continuous time model predictive control design using orthonormal functions. *International Journal of Control*, 74(16):1588–1600, 2001.

[108] L. Wang. A tutorial on model predictive control. *The 4th Asian Control Conference*, 49:1394–1399, 2002.

[109] L. Wang. *"Model Predictive Control System Design and Implementation Using MATLAB"*. Springer, 2009.

[110] L. Wang, C. T. Freeman, E. Rogers, and D. H. Owens. Experimentally validated continuous-time repetitive control of non-minimum phase

plants with a prescribed degree of stability. *Control Engineering Practice*, 18(10):1158–1165, Oct 2010.

[111] P. Wang F. H. Choo Y. Tang, P. C. Loh and F. Gao. Exploring inherent damping characteristic of lcl-filters for three-phase grid-connected voltage source inverters. *IEEE Transaction on Power Electronics*, 27(3):1433–1443, March, 2012.

[112] D. K. Yoo and L. Wang. "Predictive Control of a Three-Phase Regenerative PWM converter using a Prescribed Degree of Stability". *18th IFAC World Congress, Milan*, Aug, 2011.

[113] N. Zagari and S. Rizzo. Medium voltage drives in industrial applications. *In Proceedings of Tech. Seminar, IEEE Toronto Section*, 2004.

[114] K. Zhou and D. Wang. Relationship between space-vector modulation and three-phase carrier-based pwm: A comprehensive analysis. *IEEE Transaction on Industrial Electronics*, 49(1):1433–1443, Feb, 2012.

[115] D.N. Zmood and D. G. Holmes. Stationary frame current regulation of pwm inverters with zero steady-state error. *IEEE Transaction on Power Electronics*, (18):814–822, 2003.

APPENDIX A

Experimental set-up

The laboratory prototype of three phase PWM converter has been developed for this work to validate the proposed control design in the real hardware environment. As shown in this Figure A.1, the three phase voltage source converter laboratory set-up consists of a step-down transformer (see mark (2)) that is used to reduce the line voltage from the main grid voltage (see mark (1)) of 415V to 30V. From the transformer, there are three line inductors (see mark (3)) connected between the converter and the transformer. These line inductors are a multi-tapped inductors whose value of inductance can be varied depending on the connection.

For LCL filter applications, an extra filter capacitors are connected to these inductors. The converter (see mark (4)) is made up of largely three components: a soft-start circuit, a number of sensors and a switching module. The soft-start circuit mainly provides a starting mechanism to limit the in-rush current when the DC-link capacitor is fully discharged at the start. The sensors include AC current sensors and DC bus voltage sensors. The switching module consists of six IGBT devices including freewheeling diode. This module is also fitted with a gate driver circuit and IGBT fault detection circuit. The real-time model predictive controller is developed using xPC target (see mark 5), and finally a DC-link load is connected to the system (see mark 6).

The overall control software and PWM switching output is executed in xPC target. xPC target is Simulink's real-time toolbox which allows easy and seamless transition from a Simulink model to a real-time executable code. Figure

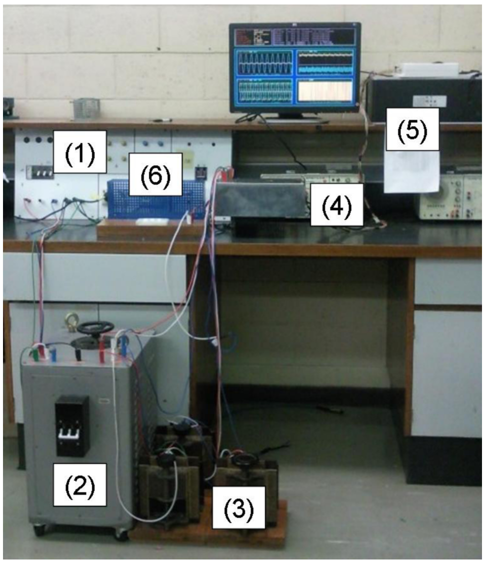

Figure A.1: Experimental set-up

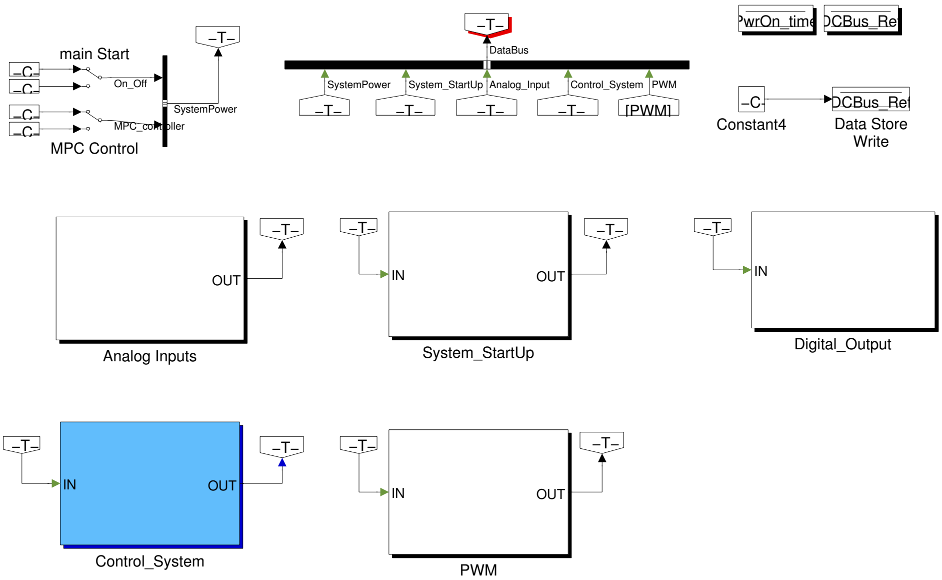

Figure A.2: Real-time simulation model of the grid-connected converter control system

A.2 shows the overall control system model used in this thesis, which consists of several sub-modules including the main control system module (indicated in blue). In the main control system module, a grid-synchronisation and a phase

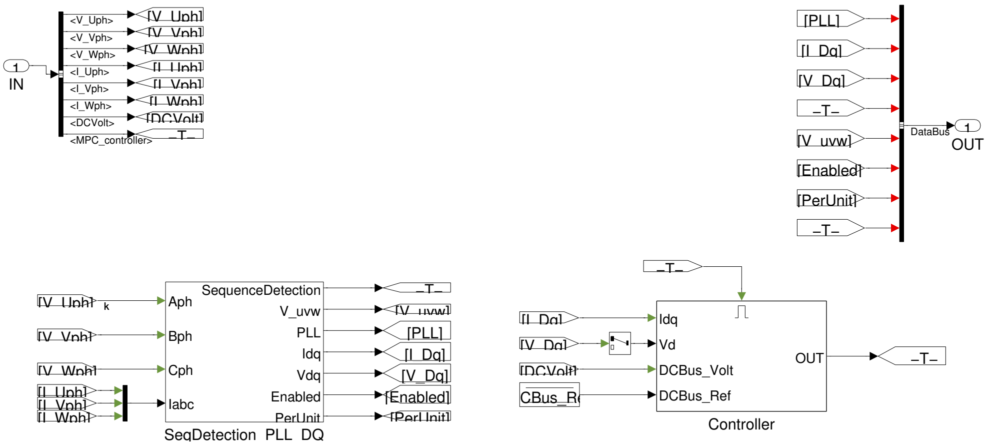

Figure A.3: The main control system module containing grid-synchronisation, sequence detection and MPC modules

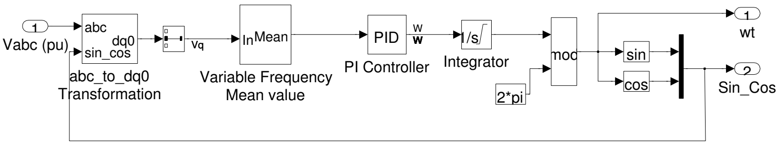

Figure A.4: Grid-synchronisation module: Phase-locked loop

detection are also included as shown in Figure A.3.

The grid-synchronisation algorithm is implemented in a feedback-loop configuration which mainly consists of synchronous reference transformation (dqo transformation) and a PI controller, see Figure A.4. Here the instantaneous phase angle is detected by synchronizing the PLL rotating reference frame to the grid voltage. The PI controller sets the q-axis reference voltage V_q to zero, which results in the reference being locked to the utility voltage vector phase angle. Under ideal grid conditions without any harmonic distortions or unbalance, a high bandwidth which is mainly determined by the gains of PI controller, can yield a fast and precise detection of the phase of the grid voltage.

As shown in Figure A.5, the phase sequence detection part is to automatically detect the orientation of three phase voltage input (e.g. U→V→W or

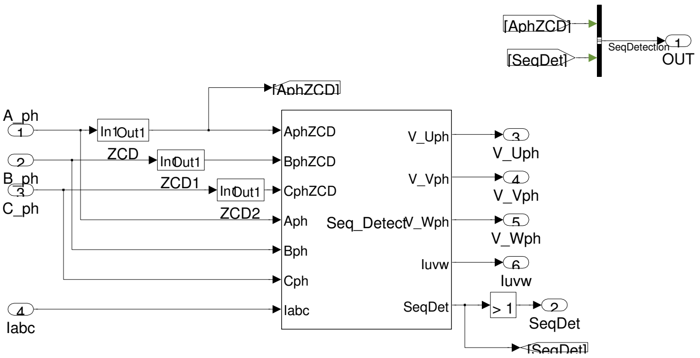

Figure A.5: Three-phase sequence detection module

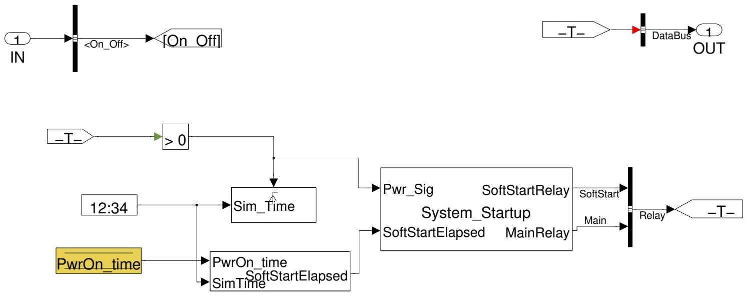

Figure A.6: Soft-start module

U→W→V) by monitoring the zero crossings of each phase. Once the sequence is detected at the start-up, synchronous reference transformation module is reconfigured to follow the correct orientation of the main grid voltage.

In the start-up module shown in Figure A.6, a soft start mechanism is implemented to prevent a large in-rush current at the start-up when the DC-bus is fully discharged. This is done by switching the soft-start relay at the start to connect the main three phase to the converter via a set of resistor. To simplify the design of this mechanism, a fixed but tunable time constant is used to determine the duration of this phase.

In the PWM module shown in Figure A.7, control inputs from the main controller is transformed from the two-phase coordinate frame (either in dq or $\alpha\beta$) into the three phase frame. After the transformation, control inputs are fur-

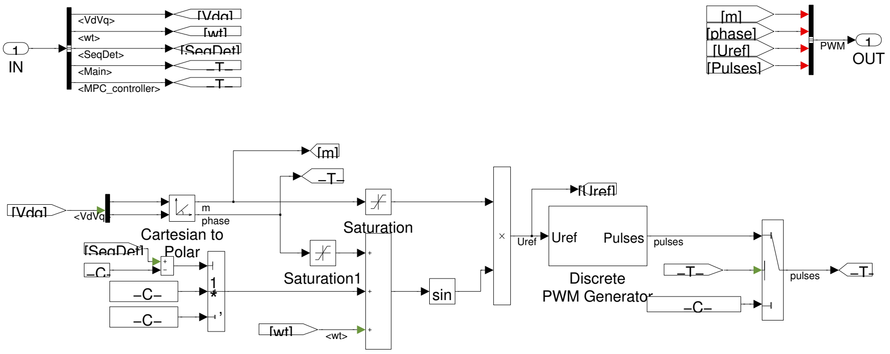

Figure A.7: Pulse-width modulation module including inverse synchronous reference frame transformation

ther discretised into six switching input signals using a regular sampled PWM method. For FCS-MPC in chapter 6, this stage is replaced by the fixed interval task for updating the switching input signals.

APPENDIX B

Continuous-time Laguerre functions

In this section, we first introduce the basic definitions and some useful properties of Laguerre functions. Based on the described properties of Laguerre functions, we then present a detailed explanation of control input approximation using Laguerre function in the continuous-time MPC design. The most of contents in this section are excerpted from Chapter 5 and 6 in [109].

B.1 Definitions of Laguerre functions

The Laguerre function is a set of complete orthogonal functions (see [] for a general description of orthogonal functions) which is defined as below for $p > 0$

$$\begin{aligned} l_1(t) &= \sqrt{2p} \times e^{-pt} \\ l_2(t) &= \sqrt{2p}(-2pt + 1)e^{-pt} \\ \vdots &= \vdots \\ l_i(t) &= \sqrt{2p}\frac{e^{pt}}{(i-1)!}\frac{d^{i-1}}{dt^{i-1}}[t^{i-1}e^{-2pt}] \end{aligned} \tag{B.1}$$

where the parameter p is referred to as a time scaling factor.

Figure B.1 and B.2 show the first three Laguerre functions with the time scaling factor $p = 1$ and $p = 2$ respectively, where the scaling factor $p = 2$ shows a faster exponential decay rate. Therefore, in general a higher value of

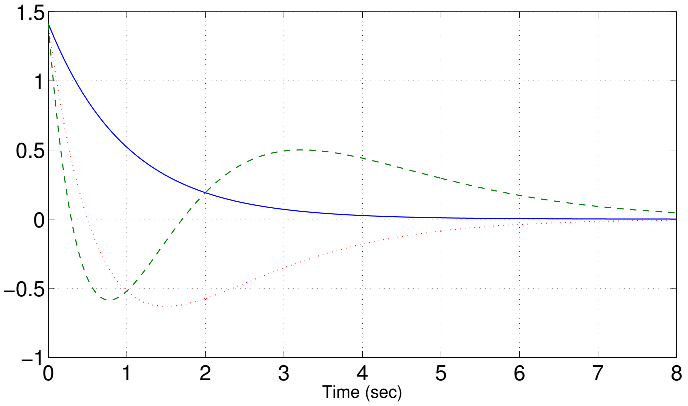

Figure B.1: Laguerre functions (p=1). Solid line:$l_1(t)$;dashed line:$l_2(t)$;dotted line:$l_3(t)$

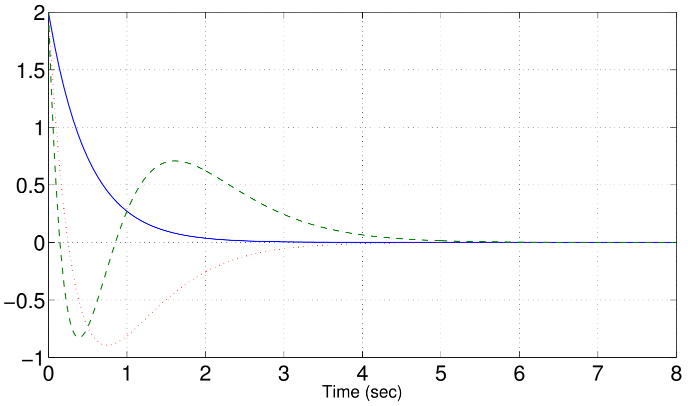

Figure B.2: Laguerre functions (p=2). Solid line:$l_1(t)$;dashed line:$l_2(t)$;dotted line:$l_3(t)$

p corresponds to a faster convergence of these functions. By using this feature of Laguerre functions in continuous-time MPC design, the time scaling factor p plays an important role in tuning the closed response of MPC system.

In the interest of simplifying the representation of Laguerre function in (B.1), we can derive a state-space form of Laguerre function by first considering the Laplace transform of the Laguerre functions (B.1), which leads to the following

Laguerre network.

$$\begin{aligned}
L_1(s) &= \int_0^\infty l_1(t)e^{-st}dt = \frac{\sqrt{2p}}{(s+p)} \\
L_2(s) &= \int_0^\infty l_2(t)e^{-st}dt = \frac{\sqrt{2p}(s-p)}{(s+p)^2} \qquad \text{(B.2)} \\
\vdots &= \vdots \\
L_i(s) &= \int_0^\infty l_i(t)e^{-st}dt = \frac{\sqrt{2p}(s-p)^{i-1}}{(s+p)^i} \qquad \text{(B.3)}
\end{aligned}$$

By letting $L(t) = [l_1(t), l_2(t), \ldots, l_N(t)]^T$, a state-spce representation of Laguerre function can be obtained as:

$$\begin{bmatrix} \dot{l}_1(t) \\ \dot{l}_2(t) \\ \vdots \\ \dot{l}_N(t) \end{bmatrix} = \begin{bmatrix} -p & 0 & \ldots & 0 \\ -2p & -p & \ldots & 0 \\ \vdots & \vdots & \ddots & 0 \\ -2p & \ldots & -2p & -p \end{bmatrix} \begin{bmatrix} l_1(t) \\ l_2(t) \\ \vdots \\ l_N(t) \end{bmatrix} \qquad \text{(B.4)}$$

The solution to the above differential equation can be represented by Laguerre function for $i = 1, 2, \ldots, N$ as:

$$L(t) = e^{A_p t}L(0) \qquad \text{(B.5)}$$

where $L(0) = \sqrt{2p}\,[1 \;\; 1 \ldots 1]^T$ and

$$A_p = \begin{bmatrix} -p & 0 & \ldots & 0 \\ -2p & -p & \ldots & 0 \\ \vdots & \vdots & \ddots & 0 \\ -2p & \ldots & -2p & -p \end{bmatrix} \qquad \text{(B.6)}$$

B.2 Application to continuous-time MPC

B.2.1 Approximation of control trajectory

The continuous-time MPC design based on the augmented system model, such as in section 3.2, transforms the optimisation problem of MPC from the control input $u(\tau)$ into the derivative of control input $\dot{u}(\tau)$ optimisation. In other words, considering an unconstrained case we can represent the optimal control input of MPC for the augmented system model as

$$\dot{u}(\tau) = -Kx(\tau) \tag{B.7}$$

where K is the unconstrained control law of MPC. The closed system with initial condition $x(t_i)$ is then given by

$$x(\tau) = e^{(A-BK)\tau}x(t_i) \tag{B.8}$$

$$\dot{u}(\tau) = -Ke^{(A-BK)\tau}x(t_i) \tag{B.9}$$

Assuming $(A - BK)$ is Hurwitz, then it is seen that the control trajectory $\dot{u}(\tau)$ decays exponentially to zero which also satisfies the following condition for $0 \leq \tau \leq T_p$,

$$\lim_{T_p\to\infty} \int_0^{T_p} \dot{u}(\tau)^2 d\tau < \infty \tag{B.10}$$

Based on the above observation, the derivative of control signal $\dot{u}(\tau)$ can be described by a set of Laguerre functions. Namely, for $o \leq \tau \leq T_p$

$$\dot{u}(\tau) \approx \sum_{i=1}^{N} c_i l_i(\tau) = L(\tau)^T \eta \tag{B.11}$$

where $\eta = [c_1 \;\; c_2 \;\; \ldots \;\; c_N]$ is the vector of Laguerre function coefficients and $l_i(\tau) = [l_1(\tau), l_2(\tau), \ldots, l_N(\tau)]^T$ are the set of Laguerre functions. As defined below, for a given scaling factor $p > 0$, the convergence of this approximation increases with a larger value of N

$$\int_0^{\infty} \left(\dot{u}(\tau) - \sum_{i=1}^{N} c_i l_i(\tau) \right)^2 < \varepsilon \tag{B.12}$$